Aerodynamic Analysis and Desing of a Car for the Shell Eco Marathon

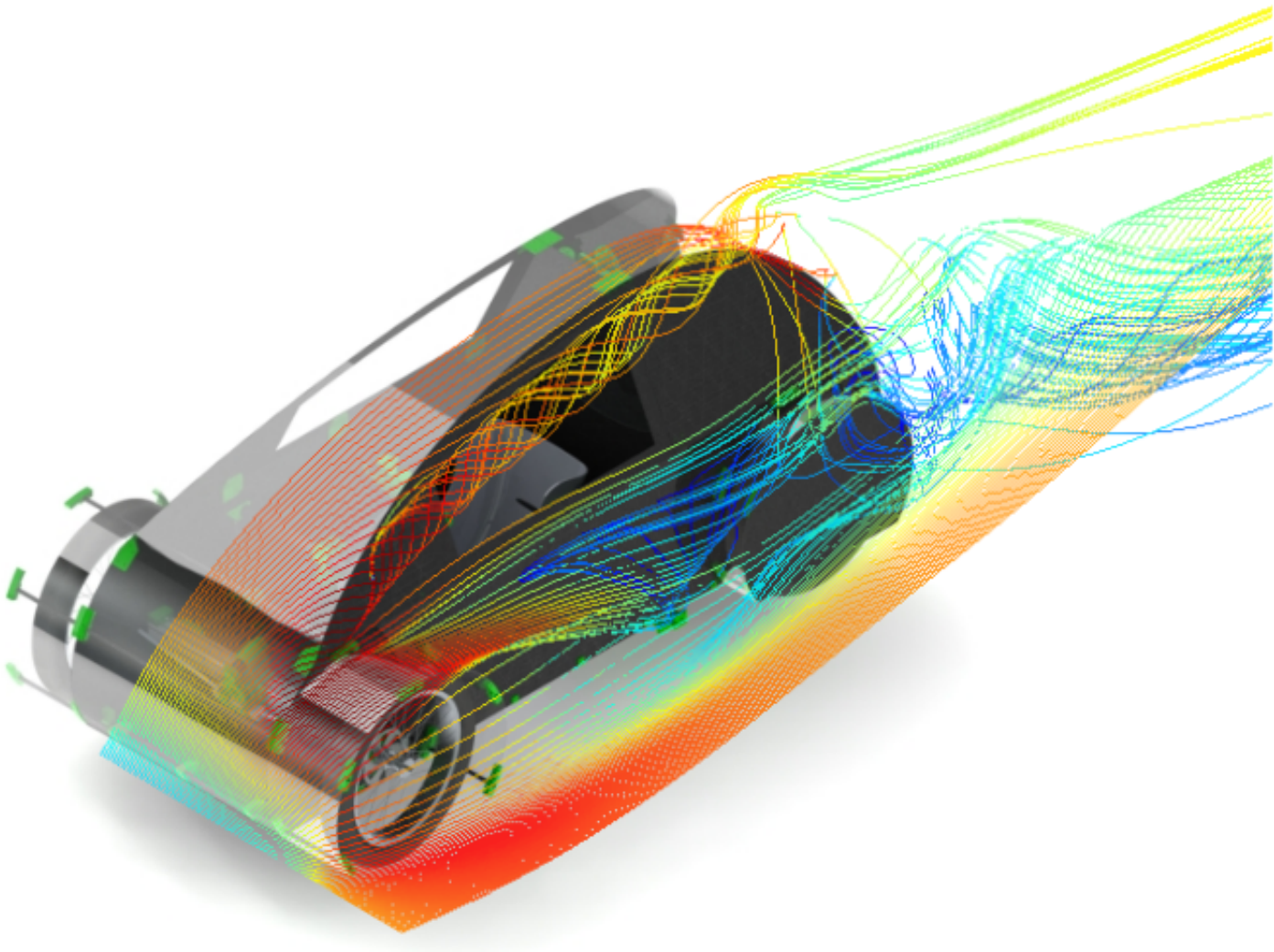

Daniel Fiuza Dosil

Master's Thesis Project, June 2016

Thermal Energy and Process Engineering

AALBORG UNIVERSITY
STUDENT REPORT

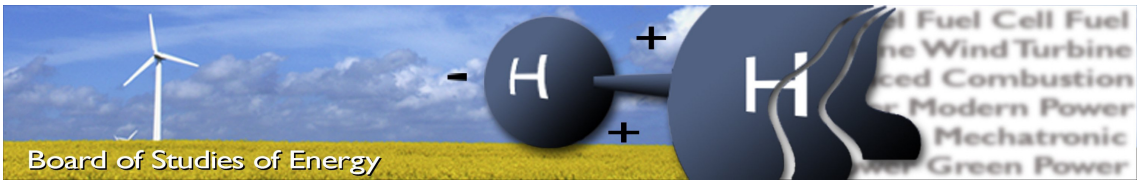

Title:	Aerodynamic Analysis and Design of a Car for the Shell Eco Marathon
Semester:	10^{th}, Spring semester 2016
Project period:	01/02/2016 - 01/06/2016
ECTS:	30
Project group:	TEPE-1007
Supervisors:	Henrik Sørensen
	Jakob Hærvig
	Christian Jeppesen

Synopsis:

In the pursuit of an ultra energy efficient car, the aerodynamic analysis of the car used by the Team Aalborg Energy in the Shell Eco Marathon competition is essential to further improve its fuel efficiency. An extensive computational and experimental analysis of the car was performed revealing the drag and lift coefficients, the aerodynamic deficiencies and the flow features. Several add-on modifications of the current vehicle with the intent of reducing the drag were designed and tested (including tail extension, edge rounding, wheel skirt and vortex generators). The individual drag reduction of these modifications varied between 9% and 35% from the current design. The author was also responsible of complete re-design of the car, obtaining a vehicle with a remarkable aerodynamic performance (the drag coefficient C_D was reduced a 80% from 0.61 to 0.12). With this new design the driving range of the car would be expected to be increased a 41%, with a new estimated fuel efficiency of 877 km/L on gasoline equivalent.

Daniel Fiuza Dosil

Pages, total: 114
Appendices: A-E

By signing this document, the author confirm that the report does not include plagiarism.

Preface

This report was written between February 1st and June 1st 2016 by a student of the 10th semester pursuing a Master in Thermal Energy and Process Engineering at Aalborg University. The project aims to study the aerodynamic performance of the car of the Team Aalborg Energy used in the Shell Eco Marathon and to reduce its drag.

The report presupposes thereby a level of knowledge about aerodynamics, fundamental fluid dynamics and computational fluid dynamics. Besides it may be helpful to have a certain knowledge about SolidWorks, ANSYS Fluent and ParaView as these tools where used for the creation of the CAD model, for the simulation of the aerodynamics and for the visualization of the solution data.

Reading guide

Source Citation

The report conforms to the scientific standard of citing the sources used throughout. The report follows the Vancouver citation method, where sources in the text are referenced with a number the following way: [Number]. This citation refers to the bibliography at the end of the report, where books are listed with author, year, title, edition and publisher. Websites are listed with author, title, date and URL. The bibliography is ordered alphabetically.

Figures, tables and formulas

Figures, tables and equations are numbered according to chapter they belongs and its order of appearance. As an example, "Figure 5.22" will be found in Chapter 5 and it will be the second figure of this chapter. Equations numbers appear in parentheses and shifted to the right side of the document.

Appendix

Appendix is named according to the letters of the alphabet and can be found in the back of the report. The appendixes contains information, both theoretical and practical and also extra results that are relevant to different parts of the main report, and can be used to support the explanations given throughout the report.

Nomenclature

Abbreviations

Abbreviation	Explanation
AAU	Aalborg University
BR	Blockage Ratio
CAD	Computer Aided Design
CCD	Charge Coupled Device
CFD	Computational Fluid Dynamics
CO_2	Carbon Dioxide
DES	Detached Eddy Simulation
LES	Large Eddie Simulation
PM	Particulate Matter
PDE	Partial Differential Equation
PIV	Particle Image Visualization
RANS	Reynolds Averaged Navier Stokes
RAM	Random Access Memory
RSM	Reynold Stress Model
RNG	Renormalization Group theory
SO_2	Sulfur Dioxide
NO_x	Nitrogen Oxides
VG	Vortex Generator
WHO	World Health Organization
3D	Three Dimensional

Symbol list

Symbol	Explanation	Unit
A	Frontal Area	[m^2]
C_D	Drag Coefficient	[–]
C_L	Lift Coefficient	[–]
F	Force	[N]
g	Gravitational Acceleration	[kg/s·m^2]
h_{ts}	Test Section Height	[m]
l	Length Car	[m]
p	Pressure	[Pa]
P	Power	[W]
q	Dynamic Pressure	[Pa]
Re	Reynolds Number	[–]
T	Thompson's Tunnel Shape Factor	[–]
U	Free Stream Velocity	[m/s]

Symbol	Explanation	Unit
v	Velocity	[m/s]
V	Volume Car	[m/s]
w_{ts}	Test Section Width	[m]
α	Angle	[°]
β	Angle	[°]
δ	Angle	[°]
ϵ	Turbulent Dissipation	[m/s]
κ	Turbulence Kinetic Energy	[m^2/s^2]
μ	Viscosity	[Pa·s]
ν	Kinematic Viscosity	[m^2/s]
ρ	Density	[kg/m^3]
τ	Shear Stress	[Pa]

Commonly used subscripts

Symbol	**Explanation**
c	Corrected
D	Drag
lam	Laminar
L	Lift
m	Model
p	Prototype
ts	Test section
$total$	Total
$turb$	Turbulent
w	Wall

Contents

Chapter 1

Introduction and Motivation

Carbon dioxide (CO_2), particulate matter (PM), nitrogen oxides (NO_x) and sulphur dioxide (SO_2) are some examples of the long list of pollutants emitted by fuel powered vehicles. Air pollution have now become the world largest environmental health risk. Studies by the World Health Organization (WHO) have linked that, for example, the air pollution in 2012 caused the death of around 7 million people [31]. The effects of the air pollution are not only harmful to the human health but also to the biodiversity, including plants, animals and climate changes in the Earth. Cause by the huge amount of air pollution produced by the transportation sector as well as the significant increase over the years of the total amount of vehicles (Figure 1.1), solutions to decrease the amount of pollution must be developed to reach a sustainable development of our society.

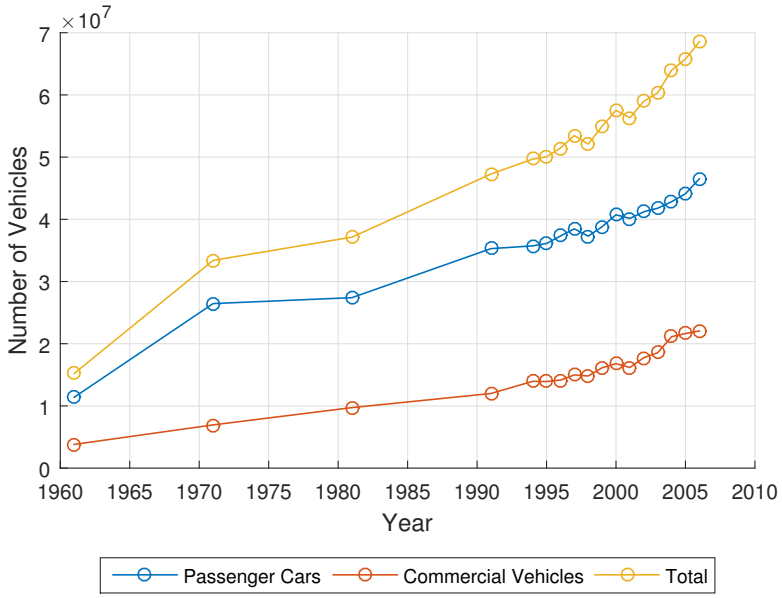

Figure 1.1: Number of vehicles in the past 50 years in the US. Data from [20].

In the transportation sector, policies and investments supporting sustainable transport, energy-efficient vehicles, cleaner fuels and electrical cars would help to reduce the main sources of urban outdoor air pollution. The revolution of the electrical cars have appeared a few years back with long driving range distances, affordable prices and the development

of better and cheaper batteries. The electric car market is still new and expensive, but countries like Norway, due to the policies and investments, has been able to reach a market share of 22.39% in 2015 [6]. It is expected that in the near future, the electrical cars can compete directly in price and range with a comparable fuel power vehicle [19].

The efficient use of the energy in a vehicle is one of the improvements that can be applied to any kind of transportation, no matter if electrical or fuel-powered vehicles, air or road transportation, cars or trucks. This increase of vehicle efficiency, along with the efficient buildings and industry has been one the most important topics of research and concern of the last decades.

The continuous increase of the car market seen in Figure 1.1, along with the extra budget for development, have provided a big opportunity for research in the automotive industry. The fuel efficiency has become one of the main topics of interest. The evolution of the fuel efficiency of the cars, motivated mainly due to the increasing prices of the oil and the environmental awareness, has increased over the years in the car market, as shown in Figure 1.2.

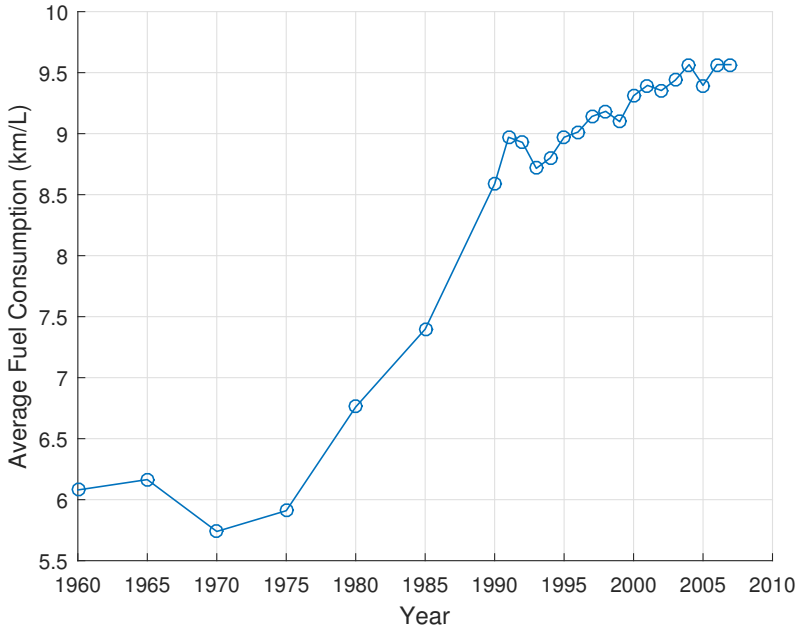

Figure 1.2: Average fuel consumption of the cars manufactured for the last 50 years. Data from [10].

The reduction of the energy losses of the car is the key for increasing the fuel efficiency. The energy in a car is not exclusively used to generate movement in the car, but is also lost due to different factors as engine and idling losses, car accessories, aerodynamic drag, rolling resistance and breaking losses. The reduction of these losses to the minimum along with a friendly driving can lead to a efficient car that can decrease the total fuel consumption considerably. Considering the amount of cars worldwide, the increase of the fuel efficiency on the car industry would reduce hugely the amount of pollutants and global-warming gases released into the atmosphere.

One example of this concern is the creation of the Shell Eco Marathon, an annual

competition in which students from all around the world gather in teams in order to build a vehicle with the highest possible fuel efficiency. The development of this kind of competitions helps to prove that a sustainable development of the car industry is possible.

1.1 Shell Eco Marathon

The Shell Eco Marathon, an annual competition sponsored by Shell, challenges student teams from all over the world to optimise and increase the efficiency in all technical aspects in order to build the most efficient vehicle. This vehicle must travel the farthest distance possible using the least amount of energy. The Team Aalborg Energy from Aalborg University participates annually in this competition with a car, that in 2015 in Rotterdam, with a efficiency of 640 km with the equivalent of 1 litre of fuel, obtained the 3^{rd} place in its category. Figure 1.3 shows the current car of Team Aalborg Energy in the track during the competition.

Figure 1.3: Aalborg University car for the Shell Eco Marathon

The competition is divided in two categories, UrbanConcept and Prototype. The UrbanConcept category includes the construction of a car resembling a conventional passenger car, with constraints about dimensions, spaces and accessories in the car. In the Prototype category the primary design consideration is maximizing the efficiency, with fewer rules about dimensional constraints. Each category is also subdivided according to the energy type used in the car. This can be gasoline, battery-electric, diesel, natural gas, hydrogen or alternative fuel.

The car of the Team Aalborg Energy is an electrical hydrogen powered car that competes

in the category of Urban Concept vehicle. In order to obtain a super efficient vehicle, the team has the challenging duty to optimise and reduce the losses of each of its components. Several student projects have been focused on the increased of the efficiency of the drive train of the vehicle, including the motor, the transmission and motor controller. A 80-85% efficiency have been achieved for the motor and motor controller at the cruise speed. For the transmission the value of the efficiency reaches approximately 90%. The same happen with the fuel cell, where the conversion process of the hydrogen into electricity have been optimised, reaching approximately an efficiency of 60% at cruise speed. The weight and the friction between components have also been another of the concerns. For the weight, advanced lightweight material as carbon fibre and 3D printed parts have been used to consummate a vehicle of only 84 kg.

However, there is one topic that has not been studied yet, the aerodynamics of the vehicle. For this reason, and for the sake of improving further the efficiency of the vehicle of the Team Aalborg Energy, the work of this thesis will aim to study and improve its aerodynamics. A low drag is a essential goal for a good fuel economy, required condition for the development of a competitive ultra efficient car.

For designing a car that can compete in the Urban Concept, the vehicle must comply with the '2016 Official Rules, Shell Eco Marathon' [27]. These comprise different constraints regarding safety, driving rules, equipment and vehicle design. In Table 1.1 some of the most important dimensional constraints are presented.

	Minimum	Maximum
Vehicle height [cm]	100	130
Body width [cm]	120	130
Vehicle length [cm]	220	350
Track width (Front axle) [cm]	100	-
Track width (Rear axle) [cm]	80	-
Wheelbase [cm]	120	-
Driver's compartment height [cm]	88	-
Driver's compartment width [cm]	70	-
Ground clearance [cm]	10	-
Driver's compartment width [cm]	70	-
Vehicle weight [kg]	-	225

Table 1.1: Dimensional constrains [27].

These limitations must be considered when designing the vehicle, as the drag is highly dependent on its shape and dimensions. In order to familiarize the reader with the current car and to use as a reference during the explanations of this thesis, Figure 1.4 shows the current car from different views. Based on Figures 1.3 and 1.4, the vehicle of the team does not give the impression of a good aerodynamic design. Sharp edges, steep rear back, wheel cases and protuberances in the surface could be expected to contribute quite negatively to the fuel efficiency of the vehicle. Bluff elements like those, are generally a great source of disturbances of the flow. The flow is not allowed to pass through these elements smoothly, creating drag, the force opposing the movement of the car, reducing its fuel efficiency.

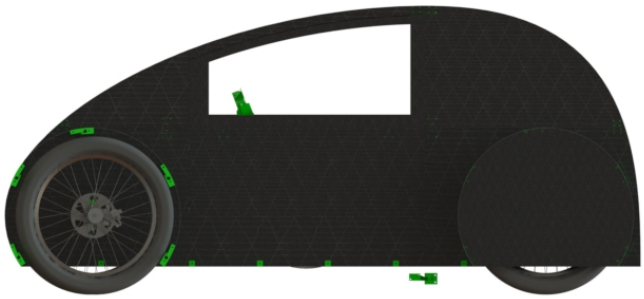

Side View

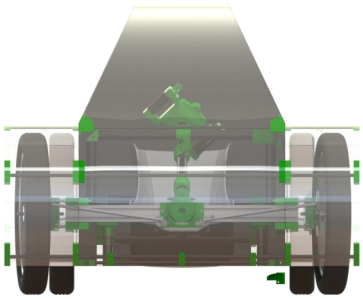

Front View

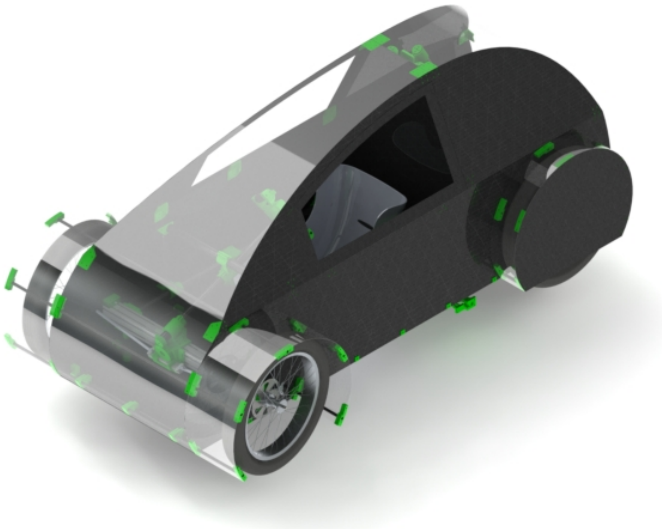

Isometric View

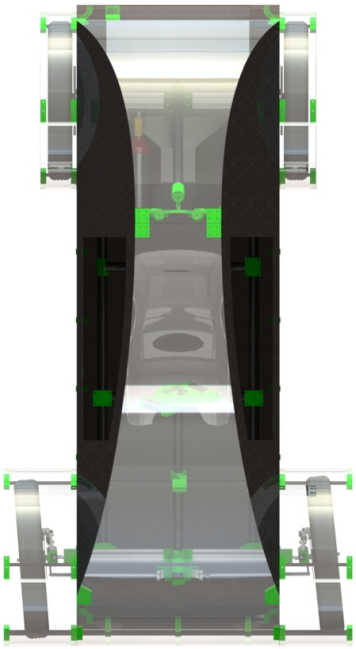

Top View

Figure 1.4: Car of Team Aalborg Energy.

Chapter 2

Problem Statement

The drag is a parameter highly linked with the fuel efficiency of the vehicle. For this reason, the study of the aerodynamic performance of the car is essential to quantify its efficiency. Various existing methods are used in the automotive industry and research to evaluate the aerodynamics of a vehicle. One of the methods is through a numerical simulation of the flow around the car, using computational fluid dynamics (CFD). This allows to resolve numerically the governing equations of the fluid motion and the forces, moments and vector fields can be calculated. The second method is an experimental approach where the full car or an scaled model is tested in a wind tunnel. The tunnel emulates a driving scenario while allows to measure the parameters of interest. A third way of evaluating the aerodynamics is through on-road testing. The vehicle is used on a track to collect data about its aerodynamics.

2.1 Problem Statement

Because of the absence of studies of the aerodynamic performance of the current car and due to its significance to improve its fuel efficiency, this thesis will aim to perform this essential task. To do so, a problem statement is formulated:

How is the aerodynamic performance of the current car? How can it be improved?

In the process of answering these questions, the following tasks are proposed:

* Evaluate the aerodynamic performance of the current car.
* Based on the current design, design and test of different modifications in the car to increase its efficiency by reducing the drag.
* If the improvements do not originate a decent drag reduction, a complete re-design will need to be proposed. This design will be tested and optimized such that the drag is minimised as much as possible.

Different analysis and designs will be conducted through the study, that will permit to carry out the investigation of the problem proposed.

2.2 Problem Approach

From the existing methods of evaluating the aerodynamic performance of a vehicle, both CFD simulations and wind tunnel testing will be used throughout this thesis. In the following subsections, the description of these approach and solving strategies will be explained.

2.2.1 Numerical Approach

The numerical approach for analysing the aerodynamics of the car is done with a commercial CFD software. This allow to perform the following:

* Calculation of the drag and lift over the different designs.
* Calculation of the properties of the representative variables everywhere in the computational domain.
* Identify characteristic flow features.
* Identify the areas contributing to addition of drag.

2.2.2 Experimental approach

The experimental approach for analysing the aerodynamics of the car is done with the wind tunnel available at Aalborg University. This allow to perform the following:

* Measurement of the forces (drag and lift) over the car by using a force balance.
* Calculation of the velocity flow field by the use of a PIV system.
* Visualization of the flow features through the injection of smoke in the flow stream.
* Validation and verification of the results obtained from the numerical simulation.

2.2.3 Comparison of both approaches

Both numerical and experimental approaches are extensively used nowadays in the automotive field. Not long time ago, the experimental testing in a wind tunnel was the only technique used to perform this kind of analysis. The computational power available in that time was not enough and/or too expensive to solve accurately the governing equations describing the flow field. In the last decades, computational fluid dynamics (CFD) have become a more standard approach for relatively simple problems, as the computers have become cheaper and more powerful. In Table 2.1, the advantages and disadvantages of the CFD simulations are presented.

Table 2.1: CFD advantages and disadvantages.

Advantages	**Disadvantages**
• Allows a full domain analysis with much more data available. • Better visualization of results. • Great time and cost reductions can be obtained.	• CFD results can be prone to numerical errors. • Limited by the amount of computational resources available. Unsuitable for really complex geometries.

Although a CFD simulation is a much better approach in terms of amount of information obtained, it is still limited by the amount of computational power needed to resolve accurately the flow. At this moment, if a wind tunnel is available, both numerical and experimental testing would be recommended. Wind tunnel have been the standard testing for so many years, that it has been perfected giving excellent results. For this reason, and as the CFD simulations can be prone to numerical errors, the wind tunnel is an excellent tool for the validation and verification of the numerical simulations. In Table 2.2, the advantages and disadvantages of the wind tunnel testing are presented.

Table 2.2: Wind Tunnel advantages and disadvantages.

Advantages	**Disadvantages**
• Accuracy and precision can be excellent if the suitable wind tunnel is used. • Validation and verification of the numerical simulations. • Speed of the testing.	• Not possible to measure certain variables (eg. wall shear stress). • Cost of the facility, need of a lot of instrumentation and large amount of power needed for run it. • Need the creation of a model with the associated cost.

For the analysis of the car, and based on the advantages and disadvantages presented in Tables 2.1 and 2.2, the numerical approach will be chosen as the main one and the wind tunnel will be used to verify and validate the numerical simulations. This decision is taken as a relatively powerful computer is available for the simulations and because the wind tunnel of the university have not been optimized for automotive testing, that may lead to inaccurate results.

Chapter 3

General Considerations on Vehicle Aerodynamics

The aerodynamics is the part of the fluid mechanics that studies the motion of the air when it interacts with a solid object. The following section serves to describe the different forces acting on the vehicle, and how affects its aerodynamic performance.

3.1 Drag and Lift

A body immersed in a moving fluid will experience forces over its surface. The resulting force over the car in the direction of the flow, in the x-direction, is termed the drag 'F_D'. The force acting normal to this one, in the y-direction, is termed the lift 'F_L'. The Figure 3.1 shows a representation of these two forces over a vehicle.

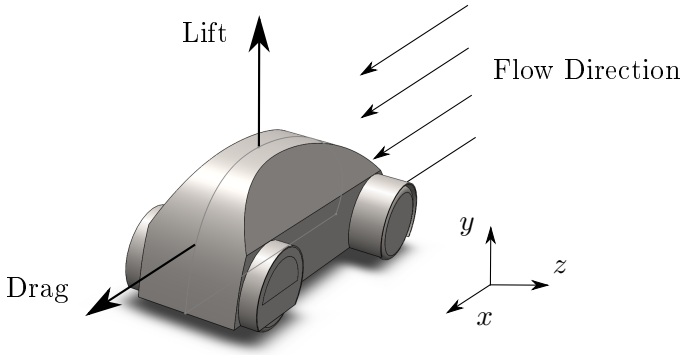

Figure 3.1: Drag and lift forces over a car.

For a fully three dimensional case, with a flow direction not aligned with the symmetry plane, a side force in the z-direction, named the side force, would appear on the vehicle. Besides, the moments created by these forces over the centre of gravity of the car could be of interested in some advanced analysis on the aerodynamic performance of a vehicle. They are called rolling, jawing and pitching moments, acting around the x,y and z axis, respectively.

A quite common approach in fluid dynamics to handle the drag and lift is the use of the drag and lift coefficients. These dimensionless quantities allows to quantify and compare the drag and lift of different shapes. The drag coefficient (C_D) is defined according to (3.1).

$$C_D = \frac{F_D}{\frac{1}{2}\rho U^2 A} \tag{3.1}$$

And the lift coefficient (C_L) is defined according to (3.2).

$$C_L = \frac{F_L}{\frac{1}{2}\rho U^2 A} \tag{3.2}$$

where:			
	A	Frontal area of the object	[m^2]
	U	Upstream velocity	[m/s]
	ρ	Density of the moving fluid	[kg/m^3]

From Equations (3.1) it is seen that the drag is proportional to the density, to the square of the velocity, to the frontal area and to the dimensionless parameter C_D. This drag coefficient is highly dependent on the shape of the body. A proper aerodynamic design of a car will aim reduce the total drag by reducing its drag coefficient and its area. In the designing process of a car the product of $C_D \cdot A$ should be used as a reference to quantify the aerodynamic performance of the designs independent of the operating conditions of velocity and fluid. The main goal of an efficient design would be to obtain the lower C_D and frontal area, while complying with the dimensional constraints of the competition and the comfort of the pilot.

As the drag is one of the forces opposing to the relative movement of the vehicle, it increases the amount of energy needed on the vehicle, reducing its efficiency. Equation (3.3) states the amount of power needed to overcome the drag in a vehicle.

$$P = U\,F_D = \frac{1}{2}\rho U^3\,A\,C_d \tag{3.3}$$

From Equation (3.3), it is seen that the power required to overcome the drag force is proportional to the cube of the speed. The power required to move a car at high velocities is much bigger than the one needed at lower velocities. This is a topic that should be taken into consideration when selecting the cruise driving speed of an ultra-efficient car for the Shell Eco Marathon. Apart from the speed, and as the density of the air can not be selected, the reduction of the $C_D \cdot A$ should be the primary concern of a good design such that the efficiency can be increased.

3.2 Types of Drag

The understanding of the types of drag and how they are produced is of fundamental importance for a proper analysis of the results obtained from experimental or numerical simulations. This enables to discern the different mechanisms of how the drag is generated. The two main ones are the pressure drag and the surface drag. In modern vehicle design, the drag is usually classified into more constituents. The induced, excrescence, interference and internal drag are explained in Appendix B.

3.2.1 Pressure or Form Drag

As the air moves around the vehicle, it results on a pressure variation all over its surface. The form drag depends on the magnitude of the pressure in each surface element and its inclination with respect to the free stream velocity. A good representative example of the pressure drag contribution is given by a surface perpendicular to the free stream velocity as shown in Figure 3.5. In this case, the drag will result in a contribution exclusive of the pressure drag. For a conventional car, the form drag contributes approximately around 55% to 60%, being the biggest component of the drag of a vehicle [25].

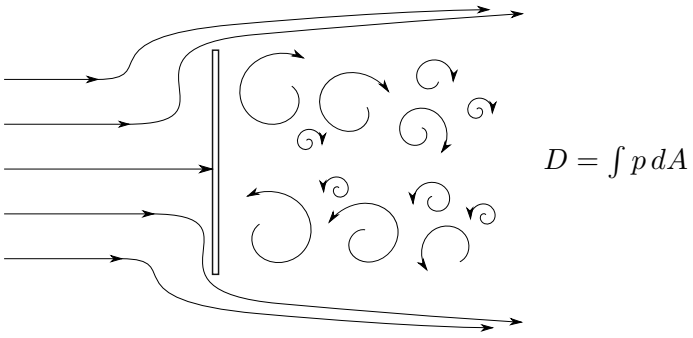

Figure 3.2: Pressure drag example.

One main origin of drag in a blunt body is due to the flow separation of the boundary layer. The flow may detach from the body when there is an adverse pressure gradient in the direction of the flow (ie. increasing fluid pressure in the flow). A graphical representation of the phenomenon of the boundary layer separation is shown in Figure 3.3.

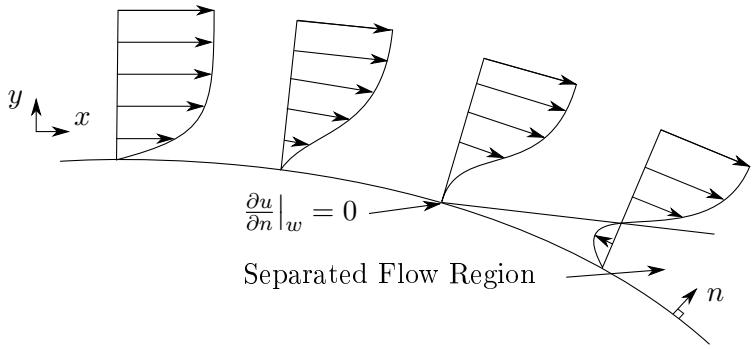

Figure 3.3: Boundary layer separation.

When a corner or a turning surface is present in the body, the flow in boundary layer may be unable to follow the deflection. This causes the separation of the stream and a recirculating flow in forms of eddies and vortices is formed. This happen because these geometrical features create a decelerating flow situation, where the energy in the boundary layer is gradually lost until the separation finally occurs. The character of flow, whether laminar or turbulent is a very important parameter for the prediction of the flow separation. The boundary layer structure of a laminar flow is different to the one in a turbulent flow, as it is shown in figure 3.4.

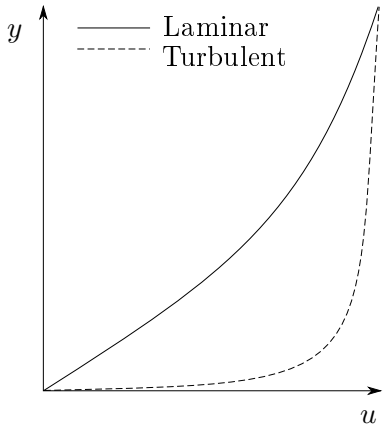

Figure 3.4: Turbulent vs. laminar boundary layer structure.

The turbulent boundary layer has an increased amount of momentum (ie. velocity) near the wall, as it is seem from Figure 3.4. This bigger amount of energy in a turbulent boundary layer with respect to the laminar one makes the first one less prone to separation. The turbulence, due to its chaotic and highly diffusive character increases the flow capability of adapting to the increasing pressure, retarding the flow separation farther downstream. One of the methods used for reducing the drag losses is based on inducing a earlier transition to turbulence. With this, the energy available in the boundary layer is increased, and the flow separation is retarded. This behaviour is taken into account when designing airfoils, golf balls and other turbulence generator devices. Although a general drag reduction is achieved by reducing the pressure drag based on this method, the surface drag is usually increased. This surface drag is explained in the next subsection. More methods of reduction of the drag in a road vehicle are explained in Appendix A.

3.2.2 Surface drag or skin friction drag

The flow moving around the surface of an object induces a second component of the drag, the skin friction drag. This is produced as a result of the no-slip condition (ie. the velocity in the wall is zero) by cause of the frictional forces acting on the surface of the body. A boundary layer is developed close to the surface of the body, defined as the region where the velocity increases from zero to the 99% of the free stream velocity. Within this zone, the viscous effects and shear stresses needs to be considered. For a conventional car, the surface drag contributes approximately a 10% to the total drag [25].

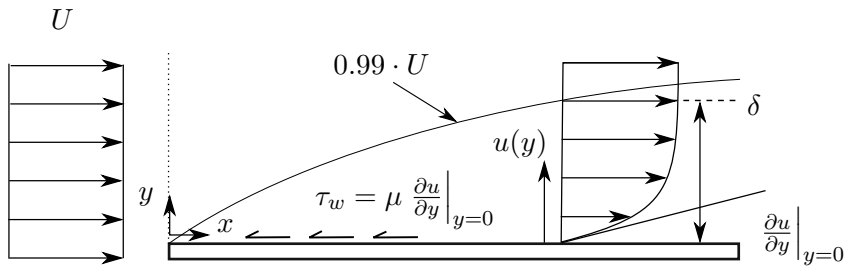

Figure 3.5: Boundary layer.

A good representative example of the surface drag contribution is given by a flat plane parallel to the free stream velocity, as shown in Figure 3.6. In this case the drag will result in a contribution exclusive of the viscous drag.

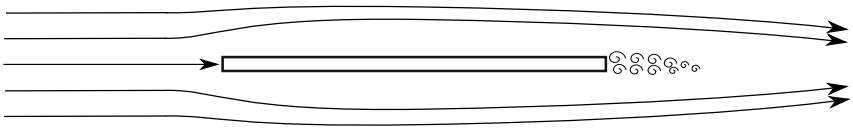

$$D = \int \tau_w \, dA$$

Figure 3.6: Viscous drag example.

The surface finish of the body of the vehicle, whether a smooth or a rough surface can also affect significantly the skin friction drag contribution. Rough surfaces create instabilities on the flow near the wall, a displacement of the boundary layer and extra momentum losses [18]. If the drag wants to be minimized, it is important to keep the surface as smooth as possible and avoid any rough surfaces or protuberances.

The character of the flow, whether laminar or turbulent also influences the contribution of this viscous drag. As explained in the previous section, a turbulent flow has an increase amount of momentum in the boundary layer with respect to a laminar one. The gradients of the velocity on the wall are steeper for a turbulent flow and therefore they are associated with a larger shear stress. This larger shear stress contributes to an increased skin friction drag in a turbulent flow.

Chapter 4

Numerical Investigation

The numerical simulations carried out in this thesis have been done using ANSYS Fluent, a commercial computational fluid dynamics (CFD) software. This chapter serves to describe the different modelling and set ups of the numerical model. First of all, the flow chart of the whole numerical designing process is presented in Figure 4.1. This procedure will be followed along the different designs analysed numerically throughout this thesis. The first step of this process involve the creation of a CAD model of the car in SolidWorks 2015. This model is then imported into ANSYS Fluent, where the numerical simulations will take place. Once the results of the simulations have been obtained, the data will be exported into ParaView, where the analysis of the information can be performed. In the following sections, these different steps, procedures and numerical set-ups will be explained.

4.1 CAD Modelling of the Car

For the current design of the car, a CAD model provided by Team Aalborg Energy have been used. For all the other modification and new designs, the geometry of the car is created with the software SolidWorks 2015. These models can be exported into an .IGES file than can be read by ANSYS Fluent.

In the new designs advanced organic surfaces are used, that can be difficult to model despite its apparent simplicity. For these new designs, the approach of creation of the surfaces in the CAD software is based on the creation of guides and profiles curves. Then, the software can interpolate between the profiles and guide curves in a smooth manner in order to create these complex surfaces. It should be acknowledge that during the process of the creation of the new designs there were a lot of limitations to control accurately all the points within the surfaces and to define relationships between the different guided curves. This was caused by the inexperience of the author with these surface tools and the limited amount of time to reach the mastery and knowledge of all of them. Small inaccuracies may be found in the designs.

The models used for the simulations are a simplified version of the actual design in case of being constructed. The simplifications used for the CFD simulations include that both wheels have been covered and no space exists between the wheel and the wheel cases. Also,

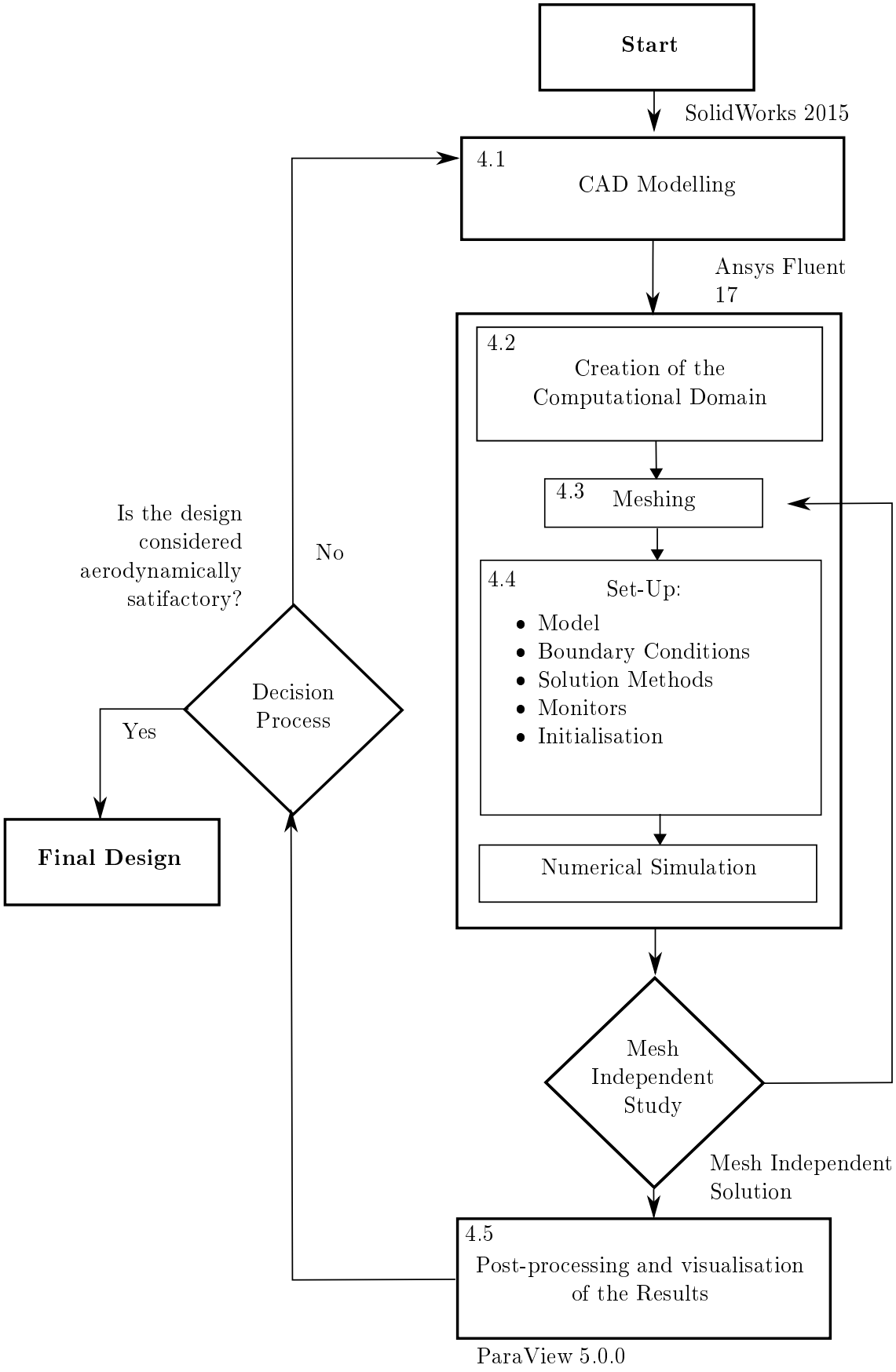

Figure 4.1: Flow diagram of the design process.

any small details that would be found in the surface of a real car are not considered, as screws, protuberances and small gaps between the different sections of the car. The CAD design behaves as a perfect solid where no air can enter or leave the vehicle. It is important to notice that these simplified designs are expected to obtain a lower drag coefficient than the real constructed car, as all those simplification would act as a small sources of drag.

4.2 Computational Domain

The computational domain is the region in the space where the numerical equations of the fluid flow are solved by the CFD software. Based on the recommendations given by the studies about automotive external aerodynamics done by Lanfrit [14], a computational domain size of at least 3 car lengths in the front of the vehicle and 5 car lengths behind is used. The vehicle in the simulations have been also raised 1 cm above the ground. Smaller distances create highly skewed cells between the wheels and ground. These cells destabilize the solution and makes the convergence of the problem really challenging and prone to numerical errors. The representation of the computational volume chosen is shown in Figure 4.2.

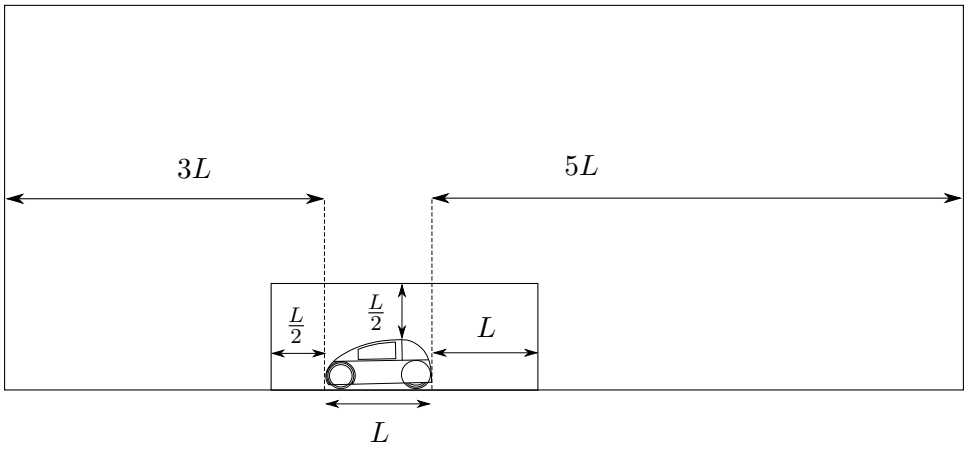

Figure 4.2: Computational volume for the CFD simulations.

Thanks to the symmetry in the vehicle, and in order to reduce the computational cost, only half of the car is simulated. For this, the computational domain is only created to one side of the symmetry plane of the car, halving the amount of volume needed to simulate the flow around the vehicle.

As it will be explained later in Section 4.3, for a local refinement of the mesh around the car, an extra inner computational box is used. For this case, and based again in the studies done by Lanfrit [14], a distance of 1 car length is left to the rear of the car and 1/2 car length to the front and sides of the car, as it is shown in Figure 4.2. It is within this box where the gradients of the variables of interest is expected to be higher, requiring refinement of the mesh in order to obtain accurate results of the discretised problem.

4.3 Mesh Generation

As explained in Appendix D, the fundamental governing equations of a fluid flow can not be solved analytically except for some special simple cases. The engineering approach of solving a general complex fluid dynamic problem is to divide the flow domain into smaller subdomains or control volumes.

The process of the creation of these subdomains, named elements or cells, is called the mesh generation. This process will be done using the software ANSYS Meshing, included in ANSYS Workbench. Regarding the types of elements that can be used, several geometries are available. Figure 4.3 shows the most used geometries for a 3D mesh generation in CFD. The choice of the element type depends on the complexity of the geometry and

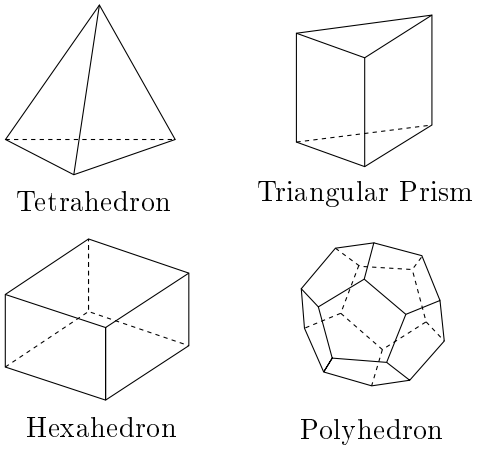

Figure 4.3: 3D elements for mesh generation

the computational resources available. The practice guidelines recommended by ANSYS is to use hexahedral meshes for simple geometries; unstructured tetrahedral meshes with prism layers for complex geometries and pure tetrahedral meshes for extremely complex geometries [4]. Due to the complexity of the geometry of the car, tetrahedral mesh will be used all over the computational domain. For the boundary layer, as the near wall region requires a special treatment, an inflation of triangular prism layers will be used.

The polyhedral elements shown in Figure 4.3, can not be created directly in ANSYS Meshing but thanks to a new function incorporated in the latest versions of ANSYS Fluent, the software allows the conversion of a regular mesh into a polyhedral one. The advantages of polyhedral meshes compared to tetrahedral have been demonstrated to be remarkable. The amount of cells needed is 3 to 5 times lower, and an increase of the accuracy and computational time of the simulation is also obtained [21]. For this reason, a conversion to polyhedral mesh will be done in most of the simulations for the sake of reducing the computational resources and time needed. A study about the differences between the solution of a tetrahedral mesh compared to a polyhedral can be found in Appendix F.

Also, besides the inflation layers for the near wall modelling, two other refinements are used. The first one, that have been briefly discussed, is the inner box sizing. This is the so-called body sizing done in the area shown in Figure 4.2. Is within this area where larger gradients of properties will occur, and therefore a finer mesh is needed. The second

refinement is done in the elements in contact with the surface of the car, where the size is further decreased. The goal is to account accurately for the flow separation that may occur in the surface of the car. With these refinements, a high quality mesh able to predict the flow correctly is expected to be obtained.

Regarding the quality of the mesh, different parameters can be used to measure the characteristic of a mesh. Three of the most used quality attributes are the skewness, the aspect ration and the smoothness of the cells. For all the meshes created, the quality of the mesh have been checked to comply with the recommendation given by ANSYS [4]. More information about these different quality parameters can be found in Appendix E.

4.4 Set-Up of the Problem

Once the mesh have been created and the problem is discretised is smaller domains, the problem is ready to be solved numerically. First, different parameters regarding the turbulence model, the boundary conditions, the numerical methods used, the monitorization of the iteration process and initialization of the solution must be chosen accordingly.

4.4.1 Turbulence Model

As explained in detail in Appendix D, it is not possible to solve the governing set of partial differential equations (Navier Stokes equations) for the general problem. In the discretised case, the Navier Stokes equations are converted into a set of algebraic equation. Solving them without any turbulence model requires an enormous amount of cells in order to account for the entire range of length scales present in the flow. As this method, called DNS, is extremely expensive in terms of computational resources, the modelling of the turbulence becomes a necessary issue in the CFD field.

Different models have been develop over the years to predict the turbulence without the need of solving the whole length scales in the flow. These models try to estimate the turbulence, so that the problem can be solve without resolving the smaller scales present (ie. Kolmogorov microscale) in the flow. The models of interest for external aerodynamics with their equations, advantages and disadvantages are explained and derived in Appendix D.

For the simulations conducted in this thesis, and based on the 'Best Practice Guidelines for handling External Aerodynamics with Fluent' [14], the Realizable $\kappa - \epsilon$ model will be the predetermined model used for all the simulations conducted in this thesis. This model, an improvement over the Standard $\kappa - \epsilon$ model, deal better with flows involving rotations, boundary layers under strong adverse pressure gradients, separation and recirculation [3]. Realizable $\kappa - \epsilon$ have demonstrated a superior ability to capture the mean flow of the complex structures [8]. The Reynolds Stress Model (RSM) is also recommended [14] and it will be used to analyse the differences between this one and Realizable $\kappa - \epsilon$. RSM is a higher order model that accounts for the anisotropy in the turbulence and the transport of

all Reynolds Stresses, with the penalty of a higher cost in computational time and RAM resources [14].

4.4.2 Boundary Conditions

In order to solve numerically the problem, the boundary conditions needs to be specified. In Table 4.1, the boundary conditions for the problem are presented.

Surface	Boundary Condition	Extra Information
Inlet	Velocity Inlet: 7 m/s	Turbulence Intensity: 1%
Outlet	Pressure Outlet*: 0 Pa	Turbulence Intensity: 5%
Car	No slip Condition	Stationary Wall
Ground	No slip Condition	Stationary Wall
Walls	Symmetry plane	-

* Gauge Pressure

Table 4.1: Boundary Conditions

An inlet velocity of 7 m/s is chosen as it is the average driving speed of the car during the Shell Eco Marathon competition. The surface of the car and the ground are set up as stationary walls with the no-slip condition. In a real case scenario, the condition of the stationary wall is not fulfilled. Only the body of the car would behave as a stationary wall, while the road and the wheels of the vehicle would be moving.

Although defining a certain velocity for the road and a rotational speed for the wheels can be set up as boundary conditions in ANSYS Fluent, this is not done so that the tests in the wind tunnel can be comparable to the simulations done in CFD. For some advance and expensive wind tunnel testing, not available for this thesis, the conditions of moving road and turning wheels could be recreated. This is done usually with a moving belt under the car that emulates the movement of the road and allows the flow to behave as a real driving situation with the precise boundary layer development in the ground.

4.4.3 Solution Methods

For the solution methods, different algorithms are available in ANSYS Fluent. Two different methods have been used for the simulations in this thesis, the SIMPLE and the Coupled. These are some of the pressure based numerical schemes available for solving the discretised Navier Stokes equation. For the simulations carried out the Coupled scheme was used, as the convergence is reached in fewer iterations and less computational time. Although, in the cases where no enough RAM memory was available, the simulations were done using the SIMPLE method.

For the spatial discretisation, the second order upwind scheme was used for momentum, turbulent kinetic energy and turbulent dissipation rate. Also, some of the under-relaxation factors were changed from the default ones used in Fluent for the momentum, pressure, turbulent viscosity and Reynolds stress equations. This was done whether the convergence was slower than expected and the stability of the solution was not compromised.

4.4.4 Monitors

In order to follow the iteration process and decide whether to stop the calculation and consider the solution as converged, several variables of interest were monitored. First of all, a monitor of the residuals was used for the continuity, the velocity components (x,y and z), the turbulent kinetic energy κ, the dissipation rate ϵ and the Reynolds stresses. The residuals are defined as the differences in the value of a quantity between two consecutive iterations. For this monitor of the residuals, the default convergence stopping criteria in Fluent was eliminated, as it was visually checked along with the other monitors that will be explained now.

Then, as the variables of interest are the drag and the lift, a monitor for the C_D and C_L was generated. This is the main monitor that was tracked during the iteration process, as once these values reach a steady behaviour of at least the 3^{rd} or 4^{th} decimal number, the solution was considered to be converged in terms of lift and drag.

If the solution was converged in terms of the drag and lift coefficients, the residual monitors was checked to ensure that all the residuals are below 10^{-4} or 10^{-5}. Both of this conditions have been fulfilled for all the data presented in this thesis.

4.4.5 Solution Initialisation

Reducing the simulation time is possible by providing a initial data field close to the final solution. For the numerical simulations where no previous data is available, the method called hybrid solution initialization was used. This uses the potential flow theory to efficiently initialize the solution [3], and provides a initial solution field.

ANSYS Fluent, in his latest versions, is able to interpolate the solution data for a given geometry from one mesh into another. This enables to compute the solution using a solution from another mesh as the starting point. This feature is really useful and reduces substantially the simulation time of the mesh independence study. Even if slightly different geometries are used, as it will happen with the modifications and improvement of the current design, the solution files from the original design have been used for the initialisation of the problem, and it will be proved to save a lot of computational time.

4.5 Post-Processing of the Results

Once the convergence criteria explained in Section 4.4.4 have been fulfilled, the simulation can be considered completed, and the solution data from the whole computational volume can be exported. The post-processing of these results involves extracting the desired flow properties from the computed flow field. Almost 100 flow properties are obtained from the solution, including pressure, velocity, turbulence intensity, vorticity and a long etcetera of other variables. The software used to process these data and to understand the flow features is ParaView 5.0.0, an open source for interactive, scientific visualization.

Chapter 5

Experimental Investigation

In order to make the experimental investigations, a scaled model of the car will be tested on a wind tunnel. This is a very employed tool in the field of the aerodynamics to perform experimental investigations on how the air behaves around a body. With this, analysis of the velocities and forces acting on the body can be conducted. It will be also used as a method to check the validity and the accuracy of a numerical simulation of a commercial CFD software. This chapter serves to describe the different setups used for the experimental analysis of the vehicle.

5.1 General Set Up

A 1:9 scaled model of the full car have been fabricated using a 3D printer and will be analysed in the wind tunnel WT241 from Aalborg University. The similarity conditions required and the theoretical background regarding model testing in wind tunnel are explained in Appendix C. In Figure 5.1 the isometric view of the tunnel that will be used in the experiments is presented. From the different parts of a wind tunnel, the test section is the most important one. It is within this area where the desirable flow condition for the testing needs to be achieved. It is also where the model and all the instrumentation is positioned.

The scaled model is placed in the test section of the wind tunnel and it is attached to it by means of a sting mount. The sting apart from serving as a mechanical support between the wind tunnel and the model, will allow to measure the forces of the car. This is because the sting is connected to the force balance, the instrument used to measure forces and moments in the wind tunnel. In Figure 5.2, the set up of the model in the wind tunnel is presented.

5.2 Force Balance

The force balance is the device that will be used for the calculation of the drag and lift of the model placed. A commercial force balance manufactured by AEROLAB that is available in the laboratory will be used. This system, based on strain gauges, is already

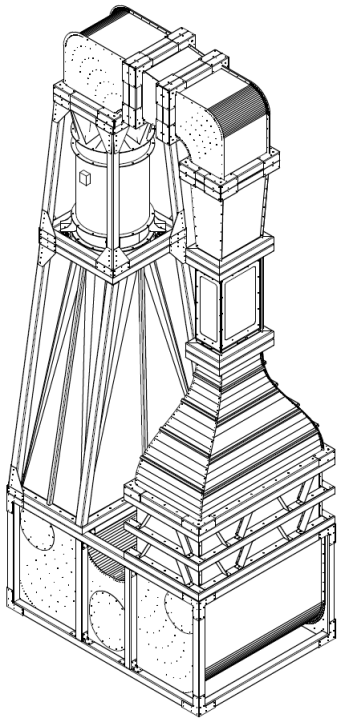

Figure 5.1: WT241 wind tunnel from Aalborg University.

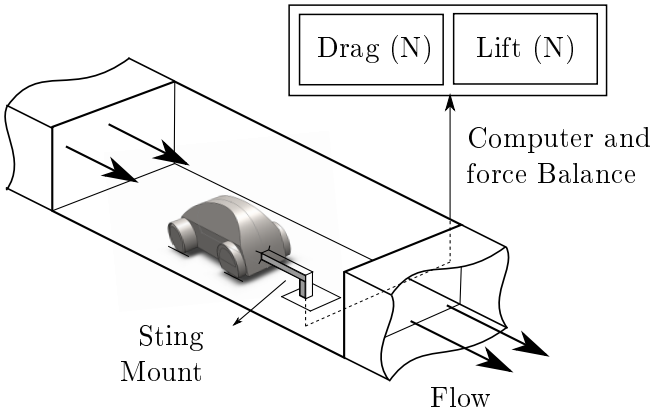

Figure 5.2: Setup of the car in the wind tunnel.

calibrated and gives the forces (drag and lift) directly in a computer. Figure 5.2 shows the configuration of this set up.

5.3 Particle Image Velocimetry (PIV)

The Particle Image Velocimetry (PIV) is a non-intrusive optical method of flow visualization that can be used to determine the velocity vector field of a given flow. The process behind the PIV is based on the measurement of the air movement by capturing a series of pictures of the flow. The PIV set-up used in the wind tunnel is presented in Figure 5.3.

In order to being able to visualize the movement of the air, a seed generator is used to

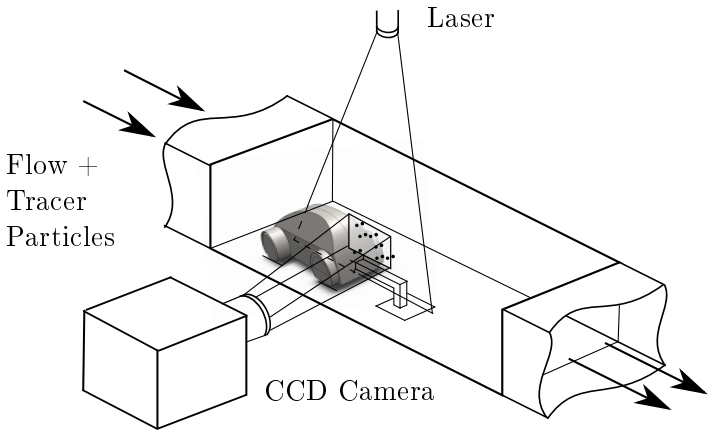

Figure 5.3: PIV set-up in the wind tunnel.

introduce tracer particles into the wind tunnel. These particles must follow correctly the flow dynamics, so they can be representative of the flow movement. The particles have to be illuminated in the region of interest at least twice within a short time interval with laser pulse. This region with the particles is recorded with the digital camera shown in Figure 5.3. This can be done with either a single frame or by a sequence of frames [22]. The displacement of the particle captured in the images between the pulses of the laser has to be determined through evaluation of the PIV recordings. In order to do that a post-processing is required.

In the post processing of the recording, the images are divided in small sub-areas. The displacement between the particles of these sub-areas is calculated by means of a statistical methods. Some of most used ones are the autocorrelation or cross-correlation. More information about these methods can be found on [22]. With these techniques, by the statistical comparison of the sub-areas of different frames, the displacement of the particles is obtained. With this displacement vector $\vec{s}$ calculated from the analysis of the frames, the flow velocity field can be also calculated by the use of Equation 5.1.

$$\vec{U} = \frac{\vec{s}}{\Delta t_{pulse}} \tag{5.1}$$

This equation simply relates the displacement of the particles with the time between the pulses of the laser, that allows the calculation of the velocity field.

For the studies in this thesis, 100 different images will be taken and analysed in order to obtain the average velocity flow field. The post-processing of the information will be done with a commercial software for PIV by means of a cross-correlation technique.

5.4 Smoke Visualization

In order to visualize the flow features of the air around the car, a smoke visualization system will be installed. This technique involves the injection of streams of smoke into the flow. Figure 5.4 shows the set up used in the wind tunnel.

A smoke generator system is used for the creation of the smoke stream. This flow of smoke is conducted thought a hose of small diameter into the wind tunnel, where is

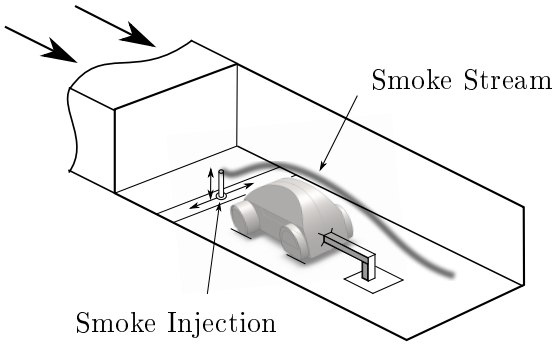

Figure 5.4: Set-up of the smoke visualization.

injected. The flow features of the smoke stream is captured with a digital camera, by mean of photographs and also through slow motion videos recorded at 120 frames per second.

5.5 Pitot-Static Tube

A pitot-static tube is a pressure-sensitive instrument used to determine speed of the flow. A schematic representation of the pitot static tube is presented in Figure 5.5.

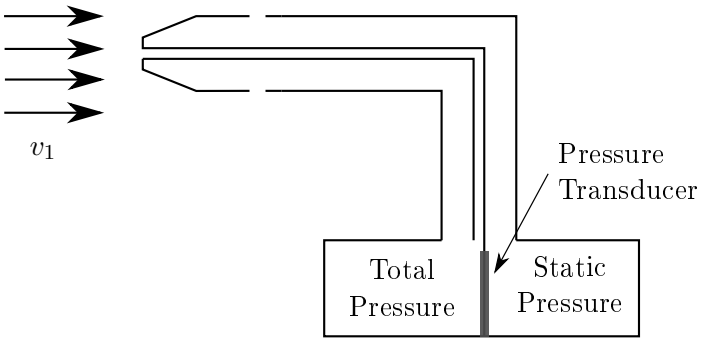

Figure 5.5: Pitot tube schematic.

The principles of operation behind the pitot tube may be explained with basic fluid mechanics principles. The well known Bernoulli Equation may be used in the derivation of the velocity equation in the tube, that is presented in Equation 5.2.

$$v_1 = \sqrt{\frac{2(p_2 - p_1)}{\rho}} \tag{5.2}$$

The pressures difference $p_2 - p_1$ can be measured with a manometer or pressure traducer as shown in the Figure **??**. The static pressure $p1$ is measured thanks to the use of the static ports on the side of the pitot tube. This device will be used to calculate the flow speed in the wind tunnel.

Chapter 6

Analysis of the Current Car

This chapter contains the results of the aerodynamic analysis of the current car of Team Aalborg Energy. Both the numerical analysis presented Chapter 4 and the experimental one explained in Chapter 5 will be conducted. This chapter is divided in three sections, the numerical results, the experimental ones and one section for the comparison and validation of both approaches.

6.1 Numerical Results

For the numerical analysis, the simplified model of the car shown in Figure 6.1 have been used. As explained in Chapter 4, the difference between the actual car and the simplified one, is that in the simplified there is no gaps between the wheels and wheel cases. Also that the frontal wheels have been covered.

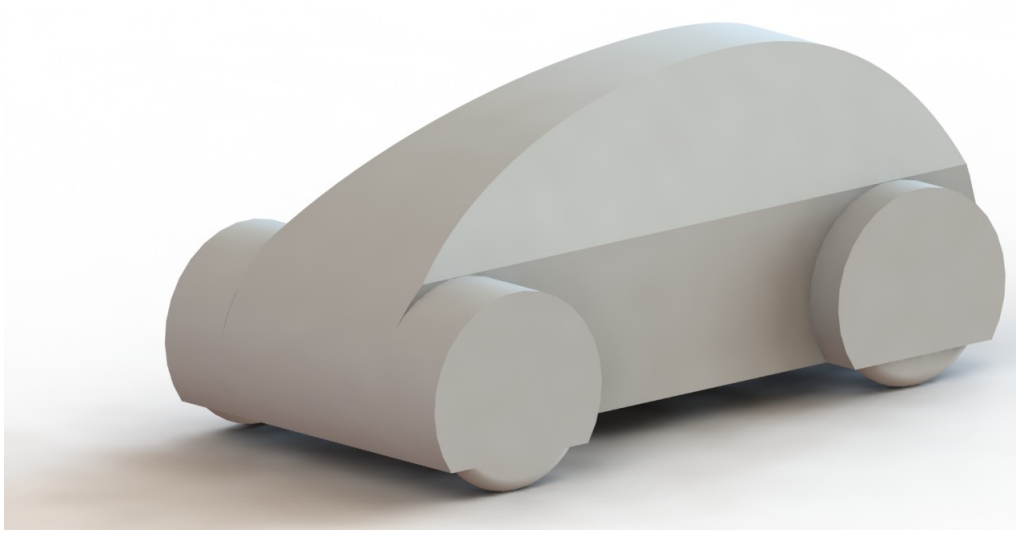

Figure 6.1: CAD model of the current simplified.

The CAD model have been imported into the CFD software, ANSYS Fluent, and the numerical approach explained in Chapter 4 is conducted. In order to later perform a mesh independent study, several simulations are conducted with various mesh sizes. For these different meshes, the face sizing and the body sizing (ie. the inner refinement) have been

gradually refined, by reducing the size of their elements. The information regarding the mesh, model used and the solution obtained from each of the simulations is presented in Table 6.1.

	Mesh 1	Mesh 2	Mesh 3	Mesh 4
Mesh Type	Tetrahedral	Tetrahedral	Tetrahedral	Tetrahedral
Nodes	$1.936\ 10^6$	$2.932\ 10^6$	$3.771\ 10^6$	$2.932\,10^6$
Elements	$11.152\ 10^6$	$14.021\ 10^6$	$18.848\ 10^6$	$14.021\ 10^6$
Face Sizing	10 mm	7 mm	7 mm	7 mm
Body Sizing	50 mm	50 mm	30 mm	50 mm
Growth Rate	1.05	1.05	1.05	1.05
Mesh Conversion	None	Polyhedral	Polyhedral	Polyhedral
Elements Polyhedral	-	$3.029\,10^6$	$3.867\,10^6$	$3.029\,10^6$
Ratio Elements	-	4.629	4.779	4.629
Model	Real. κ–ϵ	Real. κ–ϵ	Real. κ–ϵ	RSM
Drag Coefficient	0.65	0.61255	0.61434	Inconclusive
Lift Coefficient	0.43	0.34440	0.34633	Inconclusive

Table 6.1: Information of the numerical simulations.

Whether to choose or not one of these solutions for the drag and lift coefficient rely upon if it is not dependent on the discretisation process and if the solution have converged.

6.1.1 Mesh Independent Study

The mesh independent study is the way of checking the dependence of the solution on the discretisation process, and is carried out by increasing the amount of elements of the mesh. Once the difference in the solutions between the meshes is small or negligible (criteria based on the application, time and resources), the solution can be considered mesh independent. If the solution is not mesh independent, the discretisation process would be a source of errors, and the result may be inaccurate and imprecise. Figure 6.2 shows the study performed for this car regarding the mesh independence.

The mesh independence study shown in Figure 6.2 is done with three different simulations. It is seen that the solution from the Mesh 3 differs only a 0.2922% for the drag coefficient with respect to Mesh 2. With such a small difference, the solution can be considered mesh-independent.

6.1.2 Convergence Study

It is also of crucial importance to ensure that each of the numerical solutions are converged. For that, the tracking of the values of the drag and lift coefficients along with the residuals is performed during the simulation. Figure 6.3a shows the convergence of the the C_D and C_L value over the iteration process. It is seen that both the drag and lift coefficient do not change with the iteration process above the 500 iterations, and therefore the solution can be considered converged.

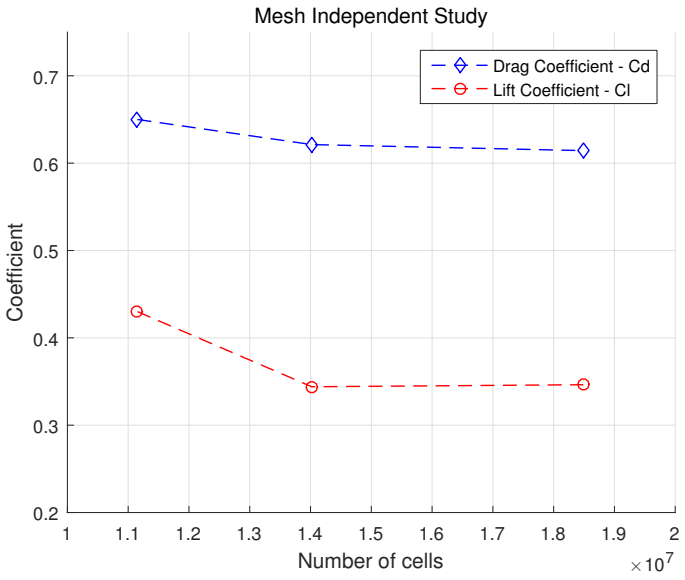

Figure 6.2: Mesh independent study.

6.1.3 Turbulence Model Comparison

For the current design, and based on the recommendations of Lanfrit [14], an extra simulation is done with another of the recommended turbulence models for external aerodynamics, the Reynold Stress Model. The RSM, based on different studies, have been proved to arise better accuracy than the κ–ϵ, but with the need of more computational resources and more CPU hours [14]. The iteration process of the simulation the RSM model is shown in Figure 6.3b.

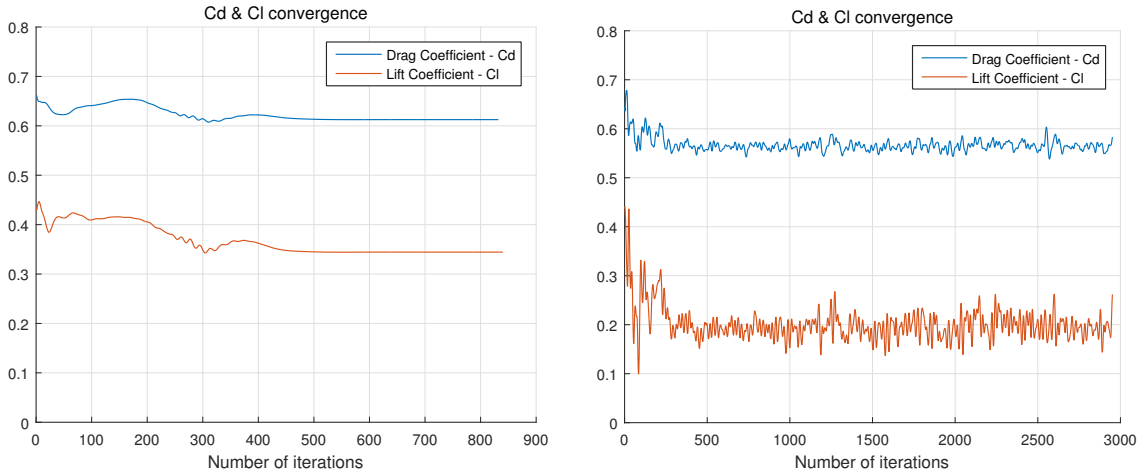

(a) Convergence of the Mesh 2

(b) Convergence of RSM model.

Figure 6.3

The convergence plot of the RSM model of Figure 6.3b shows a non-steady behaviour. No conclusive results regarding the C_D and C_L value can be obtained from this simulation. A possible reason for this non-steady behaviour is the existence of a transient behaviour on the wake of the car that does not let the coefficients to stabilize, but oscillate around

a pseudo-mean value. A transient behaviour may exists in the back of some cars with a steep rear end, as square back configurations [14].

6.1.4 Transient simulation

In order to check the existence of a transient behaviour of the drag and lift in the car a transient simulation is carried out. After initializing the problem with the converged and mesh independent solution of mesh 3 to reduce the computational time, the transient simulation results obtained are shown in Figures 6.4a and 6.4b.

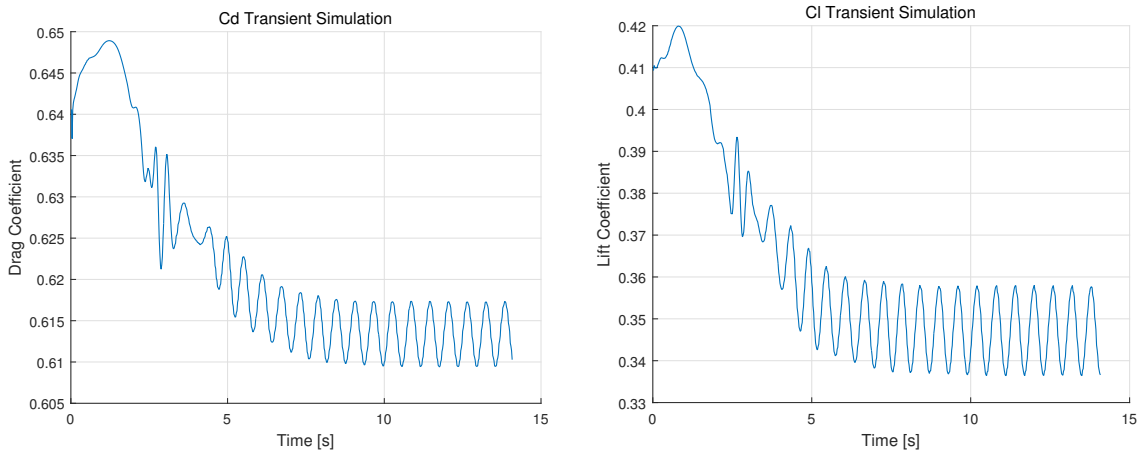

(a) Transient behaviour of the drag coefficient. (b) Transient behaviour of the lift coefficient.

Figure 6.4

From the Figures 6.4a and 6.4b it is seen the existence of a transient behaviour of the car. That may explain the oscillations seen in the convergence of the RSM simulation. This transient analysis shows that the C_D value oscillates between the values of 0.6095 and 0.61725, indicating a variation of 0.632% up and down the mean value. For the lift coefficient the oscillations falls between 0.3365 and 0.3579, with a larger variation of 3.082%. For the transient analysis the frequency of the oscillations is found to be approximately 0.58 s (1.8 Hz), that could be linked to vibrations that may be seen in the car while driving.

6.1.5 Results

After discussing the mesh independence and the convergence of the solutions together with the transient behaviour in the solution, the results from the Mesh 3 are chosen. The solution of this mesh, of more than 18 million elements, proved to be mesh independent and converged, results in a drag coefficient of 0.614. This value should not be taken as a constant value, but the average of an oscillating drag coefficient, as it was proved to involved a transient behaviour. The mean lift coefficient will be considered as 0.346, but the transient nature of the lift must also be acknowledged.

The total drag force over the vehicle at 7 m/s, the primary parameter in this study is presented in Table 6.2, together with the reference values used for the calculation of the

dimensionless drag and lift.

Frontal area	0.8440 m^2
Density air	1.225 kg/m^3
Air speed	7 m/s
Pressure Force	14.8393974 N
Viscous Force	0.72285128 N
Total Force	15.5622488 N

Table 6.2: Reference values and drag force.

Figure 6.5 shows the relative contribution of the pressure drag compared with the viscous drag. It can be observed that the mayor contribution of the drag is due to the pressure

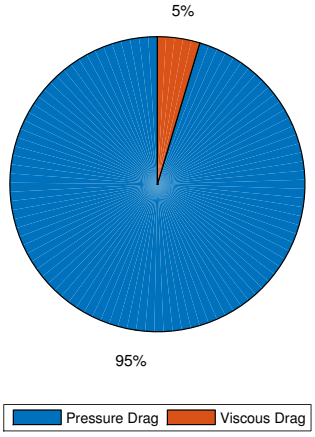

Figure 6.5: Relative magnitude of pressure and viscous forces.

drag, contributing to the 95% of the total. This is a clear indicator that the design have the potential to be improved by the streamlining of the shape of the car. It should be noted that a streamlined design is expected to reduce the pressure drag by usually increasing the surface area in contact with the fluid. This would cause the collateral of an increased viscous drag, although the overall drag reduction would be expected to be positive and beneficial for the aerodynamics.

For the quantitative comparison of the aerodynamic performance of this car, the drag coefficient along with the frontal area is the most representative parameter. The forces shown in Table 6.2 are only illustrative for the own car, or to compare cars with similar size, at the same speed and in same fluid. With a C_D value of 0.614, and comparing a benchmark values of some of the cars available in the market, it is safe to say that this design is extremely deficient in terms of aerodynamic performance. Even the cars with the higher drag coefficient found within a list of more 100 vehicles (eg. C_D of 0.48 of a Fiat 126 Bambino from 1977)[11], their aerodynamic performance is much better than the current design of the Team Aalborg Energy. Even with a frontal area more than two times smaller than a regular commercial car, the C_D·A of 0.518 is in the same order of magnitude as some of these commercial vehicles.

The improvement of the design can not be done with just the quantification of the total drag shown in this section. The analysis of the flow features and the information

obtained from the CFD simulation is essential for the understanding the causes of this deficient design. Knowing the causes that produce the drag, will allow to modify the design accordingly in order to be improved. In the next Subsection 6.1.6, the analysis of data obtained from the simulation is presented. These visualization of the vector fields will allow to study where and how the drag is produced within the car.

6.1.6 Data Analysis

From the CFD results, the pressure and velocities fields together with other variables characterizing the flow are obtained in the solution. This section contains an analysis of the data from the CFD simulation, including velocity, pressure and turbulence intensity flow fields.

Velocity Field

In Figure 6.6, the velocity magnitude field in the symmetry plane of the vehicle is presented. From this figure, several flow features can be identified and are explained.

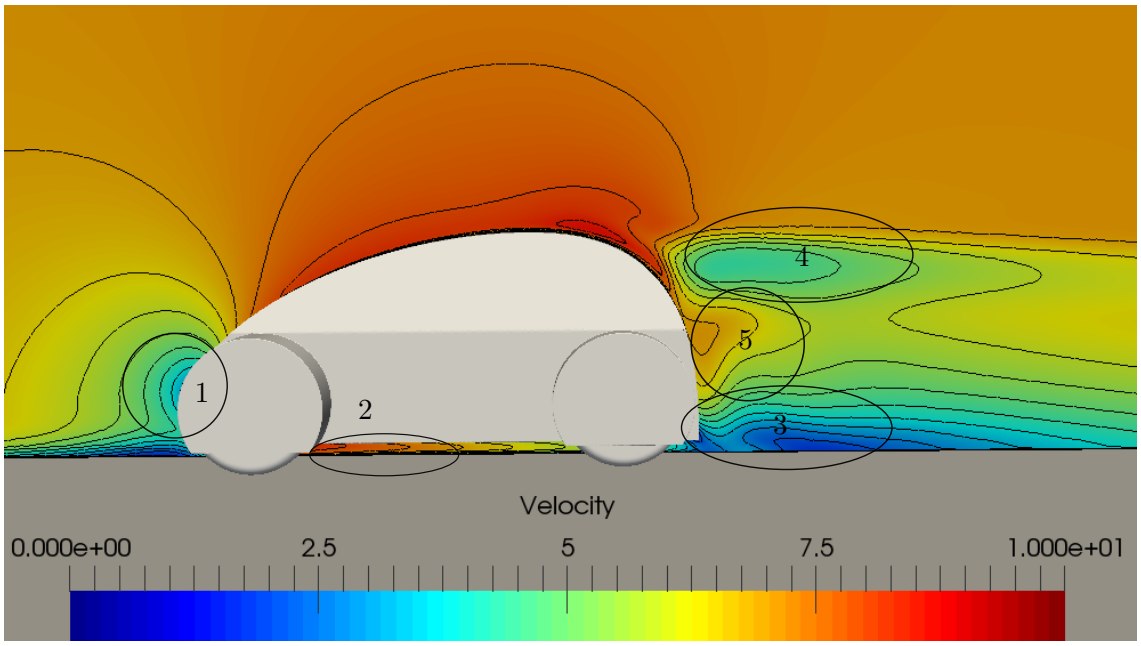

Figure 6.6: Velocity flow field in the symmetry plane [m/s].

1. As it is expected from the fluid mechanics principles, the front of car will slow down the particles of air close to it. The flow velocity is gradually reduced in the nose area, reaching a stagnation point where the local flow velocity will be zero.
2. After the flow has been slowed down due to the frontal part of the car, the fluid undergoes an acceleration into the lower and upper body of the vehicle, increasing its velocity. This behaviour it can be explained due to a decrease of the pressure, as it will be seen from Figure 6.7. The flow is accelerated up to velocities close to 12 m/s in the turning area between the front and the underbody, and between 8 to 9 m/s in the upper surface of the car.

3. A really low velocity magnitude region, between 0 and 3 m/s, is present in the lower part of the wake. This is due to the separated flow in the wake together with the boundary layer development close to the ground (being the velocity zero at the ground because of the no-slip condition).
4. In the upper part of the wake, a low velocity region is also present (velocities magnitudes between 4 and 5 m/s). It will be later seen in the smoke visualization process that is in this region where the flow separation occurs and where the rotating vortex are generated. Regions of inverted flow velocity appears, than in the averaged velocity flow field may be expected to be seen as a low velocity region.
5. Between 3 and 4, there is a higher velocity area with speeds close to the free stream velocity of 7 m/s. This high magnitude in the wake it might be caused by these rotating structures. Vortices create different velocity regions between the centre and outer part of it, caused by its rotational movement, that may explain this high velocity region.

Pressure Field

In Figure 6.7, the pressure field in the symmetry plane of the vehicle obtained from the CFD results is shown. Based on this figure, several flow features related with the pressure can be identified. The pressure changes in the field can be directly linked with the ones in the velocity field, as an increase in the pressure in the field would lead to a decrease in the velocity magnitude. These flow features regarding the pressure are presented below.

1. A region of high pressure is present in the front of the car. It increases up to three times the free stream value and can be associated to the low velocity area shown previously in Figure 6.6. The influence of this high pressure reaches a considerable distance upstream.
2. Once the flow has overcome the deflection from the frontal surface, it reduces its pressure in the upper and side of the vehicle. This reduction reaches a minimum of 109 times lower than the free stream pressure. The sharp edge on the side of the vehicle may create a rotating vortex line. This would explain the reason why the extremely low pressure area seems to follow a line trough the side window of the vehicle. The rotating vortices, as with the wing-tip vortices in the airfoil of an aircraft, as a consequence of their vorticity, create an area of low pressures. This region is confined due to the swirling of the flow, creating the so-called vortex line. Further analysis of the data have shown this hypothesis is correct, as it can be seen from Figure 6.8.

   From this figure it can be identified that the sharp edge of the car causes the flow to glide from the upper to the side surface and swirl into a vortex sheet. Figure 6.8b, also helps to visualize the existence of the vortex line and the rotating structure present in this region.
3. As with the upper side, once the flow has overcome the deflection from the frontal surface it will switch also to the underbody of the car. The pressure decreases after

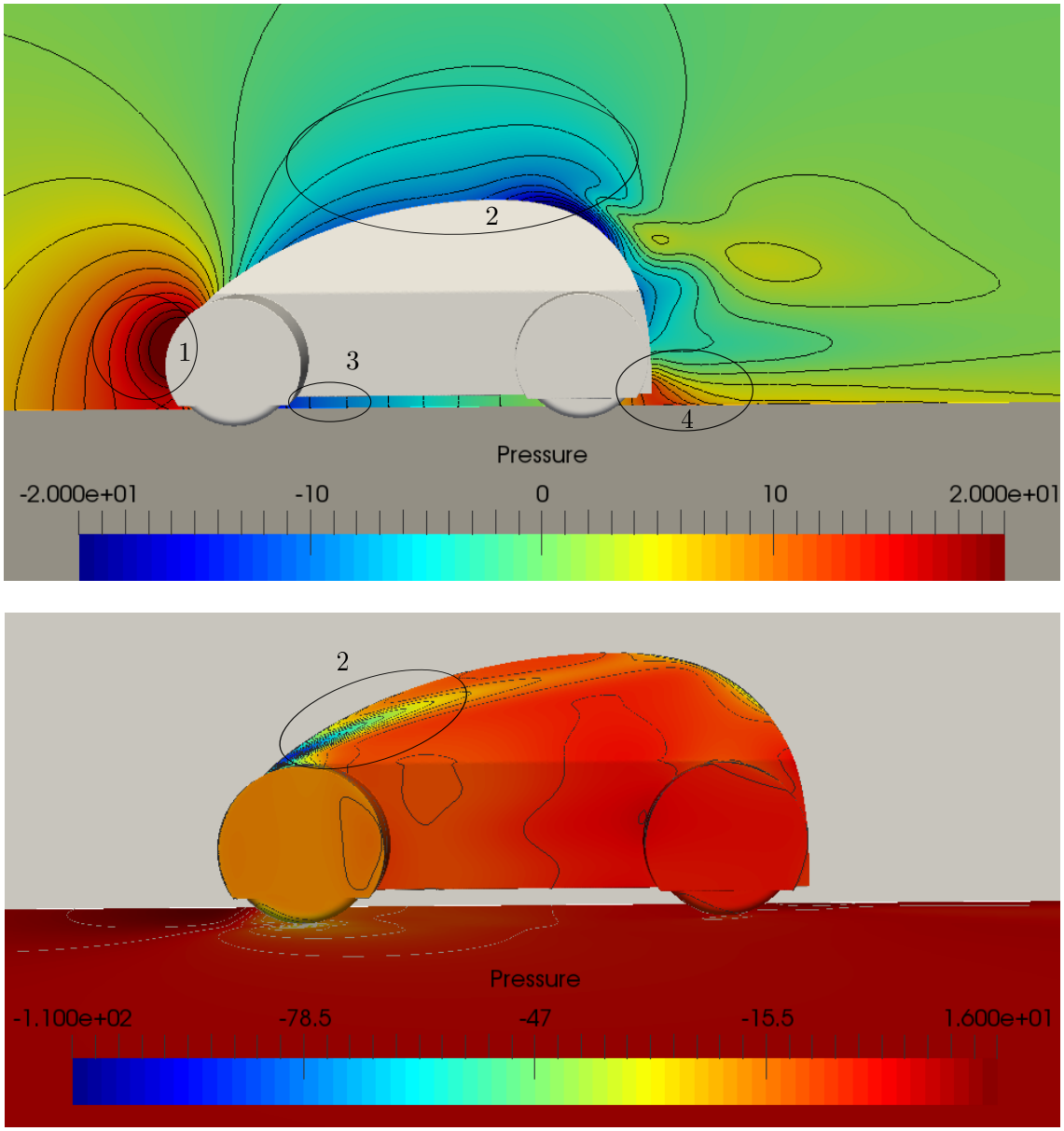

Figure 6.7: Pressure (Gauge) flow field in the surface of the car and in the symmetry plane.

the sharp edge between the nose and the underbody and, once more, can be related with the increased velocity seen in the area 2 of Figure 6.6.

4. In the wake of the car, and as a result of the low velocity in that region, the pressure increases again. Additionally, as similarly identified with the velocity, there is a region of higher pressure in between the upper and lower part of the wake. This may corroborate, again, the initial hypothesis of the presence of rotating structures in the wake.

Turbulence Intensity Field

In Figure 6.9, the turbulence intensity field in the symmetry plane of the vehicle is shown. From this figure, several flow features regarding the turbulence intensity can be identified and will be explained below.

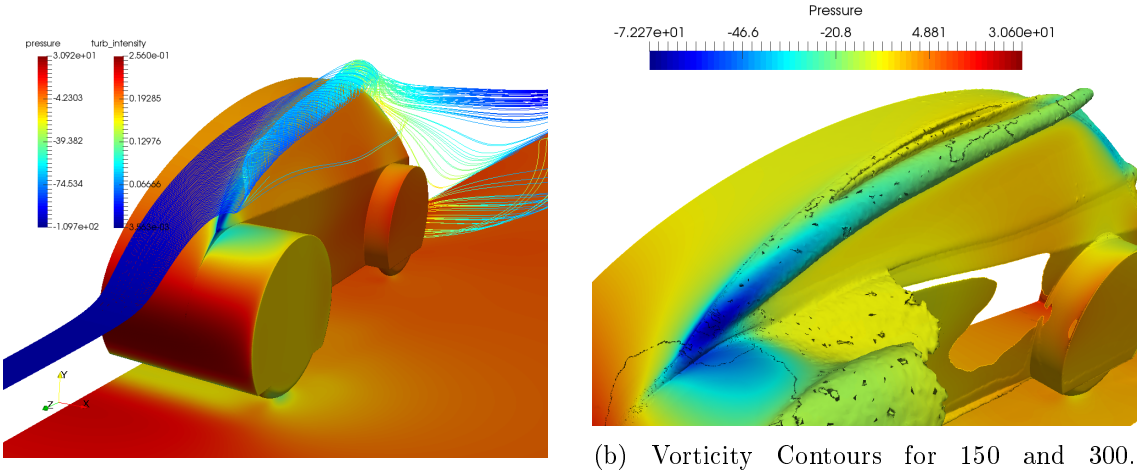

(a) Flow separation in the side edge.

(b) Vorticity Contours for 150 and 300. Coloured with the pressure.

Figure 6.8: Rotating flow structure - Vorticity

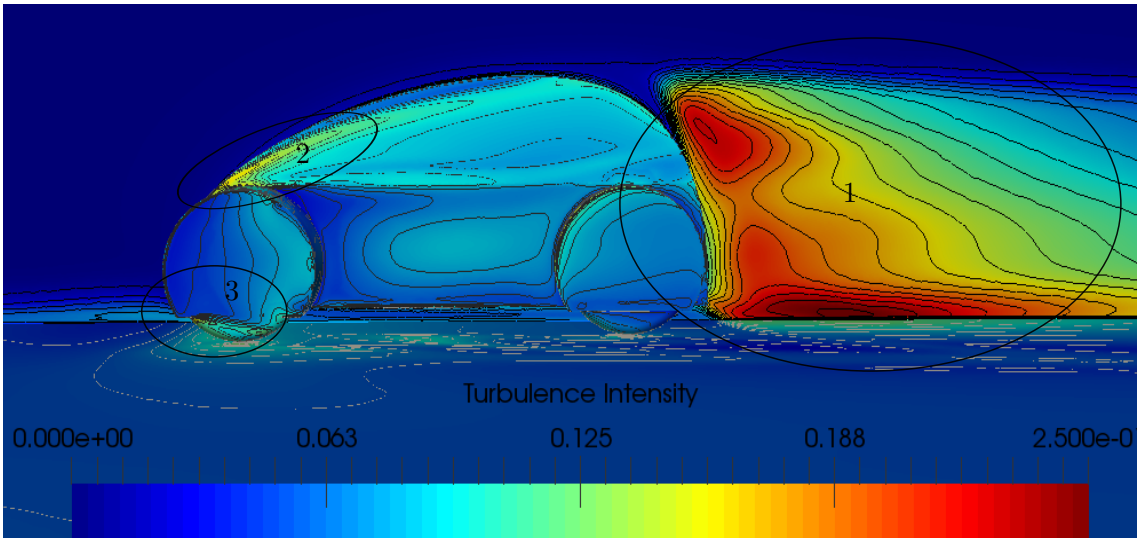

Figure 6.9: Turbulence intensity flow field in the symmetry plane and surface of the car.

1. Turbulence is created abundantly at the wake of the car. The rear back generates a turning situation that makes the flow unable to follow the surface of the car. This causes an adverse pressure gradient that leads to the flow separation, with a substantial production of turbulence as it can be seen on the Figure 6.9 .
2. The sharp edges on the side of the car, the wheels and wheel cases are the other primary sources of turbulence intensity.
3. Another source of turbulence is found in the sharp edge between the frontal area and the underbody. This source of turbulence will be propagated some distance downstream. All the regions where a sharp edge is present or a steep turning situation appears seems to be the main sources of turbulence intensity for a body.

With the discussion made from Figures 6.6, 6.7 and 6.9, the wheelcase, the steep rear back of the vehicle and the sharp edges in the side and front of the vehicle have been

identified as the main sources of turbulence and gradients of pressure and velocity. Another view of the turbulence intensity of some of these regions are shown in Figure 6.10.

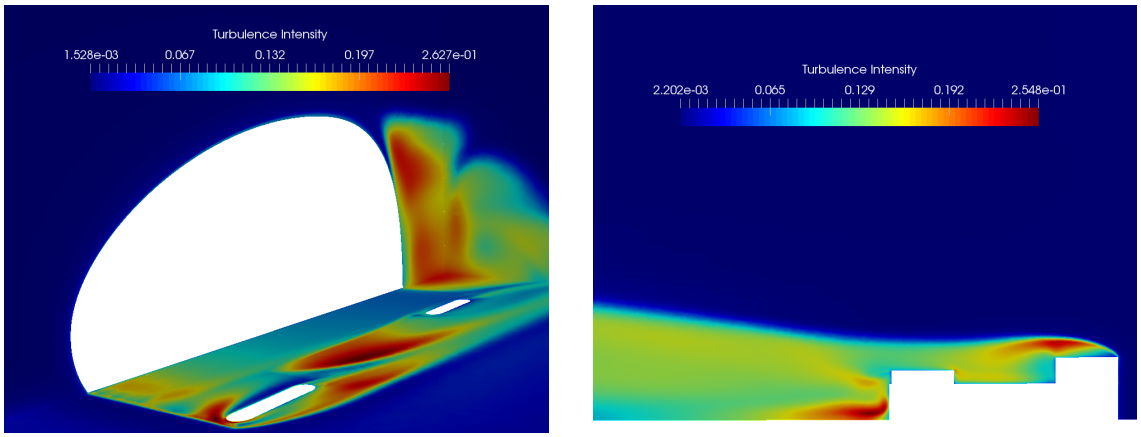

(a) Turbulence intensity on the underbody and wake of the car.

(b) Turbulence intensity, top view. Sliced at the nose of the car.

Figure 6.10: Other Views of Turbulence Intensity Field

From Figure 6.10a, it can be seen how the sharp edge between the frontal area and the underbody generates turbulence intensity. Also how the wheels and wheelcases create turbulence into the underbody of the car. The structure of the wake flow can also be seen from this figure. Regarding its magnitude, it is seen that the turbulence intensity is bigger in the region between the wheels than in the back of the car. This is due probably to the flow separation in the front wheelcase for a flow that have been accelerated after surpassing the frontal area. In the right, in Figure 6.10b, the turbulence intensity of the top plane cut from the nose of the car is presented. This figure shows how much the wheelcases and the sharp edge in the front wheel influences the turbulence in the flow, and how this is propagated widely into the sides and wake of the car.

As the wheelcases are found to be one of the most important sources of turbulence in the vehicle, Figure 6.11 is shown to better understand the flow in this region.

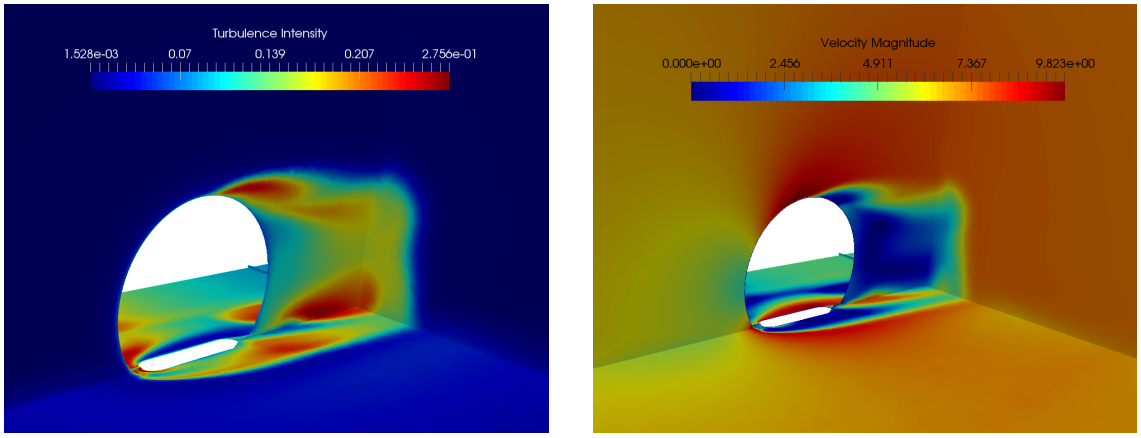

(a) Turbulence intensity on wheel case.

(b) Velocity on wheel case.

Figure 6.11: Velocity and turbulence on wheel case.

From Figure 6.11a, the turbulence intensity generated by the front wheel case is presented. It can be seen from this figure that behind the case, a great amount of turbulence is generated, as the flow is expected to separate from the surface of the cylindrical shape. The velocity field of the same view is shown in Figure 6.11b. It is seen that the flow is brought almost to rest in the wake of the wheel, where the velocity is close to 0 m/s. In the top of the wheel case the flow is accelerated up to velocities close to 10 m/s.

One of the most interesting flow features in the wheels seen in Figures 6.11a and 6.11b it is what happen at both sides of the wheel. In the case of the velocity flow field, the velocity magnitude in the region close to the right side of the wheel (ie. the outer part) is close to zero, while the area in the left side region reaches velocities close to 10 m/s. The opposite behaviour occurs with the turbulence intensity, where no turbulence is generated in the left side region but on the other hand, a high amount of turbulence intensity is created in right side of the wheel cases.

As a summary, from the investigation of this solution data, different areas have been found as main sources of turbulence intensity, pressure and velocity gradients:

1. The steep rear back.
2. Both the front and back wheel cases.
3. Edge between side and roof.
4. Side edge in the frontal wheel cases.
5. Flow in underbody and wheels.
6. Frontal edge.

These areas are expected to be the main causes of the high drag obtained over the vehicle. If the aerodynamic performance wants to be improved, the main focus should be to correct how the flow behaves around this areas.

6.2 Experimental Results

This section serves to describe the experimental analysis done in the current design. To do so, a scaled model of the car was placed in the wind tunnel. Using the instrumentation and the set-up explained in Chapter 5, the drag force over the model, the velocity field and the flow features can be calculated.

6.2.1 Force Measurements

The velocity required in order to match the Reynolds number and fulfil the similarity conditions should be 63 m/s. Caused by the difficulty of obtaining that exact speed in the wind tunnel, the closest one to that is used, with a value of 63.8 m/s. In order to investigate the changes of the C_D value in connection to the Reynolds number, more measurements of the forces at different speeds are also recorded. Figure 6.12 shows all the measurements of the drag force in the wind tunnel for different flow velocities.

In Table 6.3, the data from the wind tunnel along with the calculation of the uncorrected drag coefficient, the Reynolds number and the statistical standard deviation is presented.

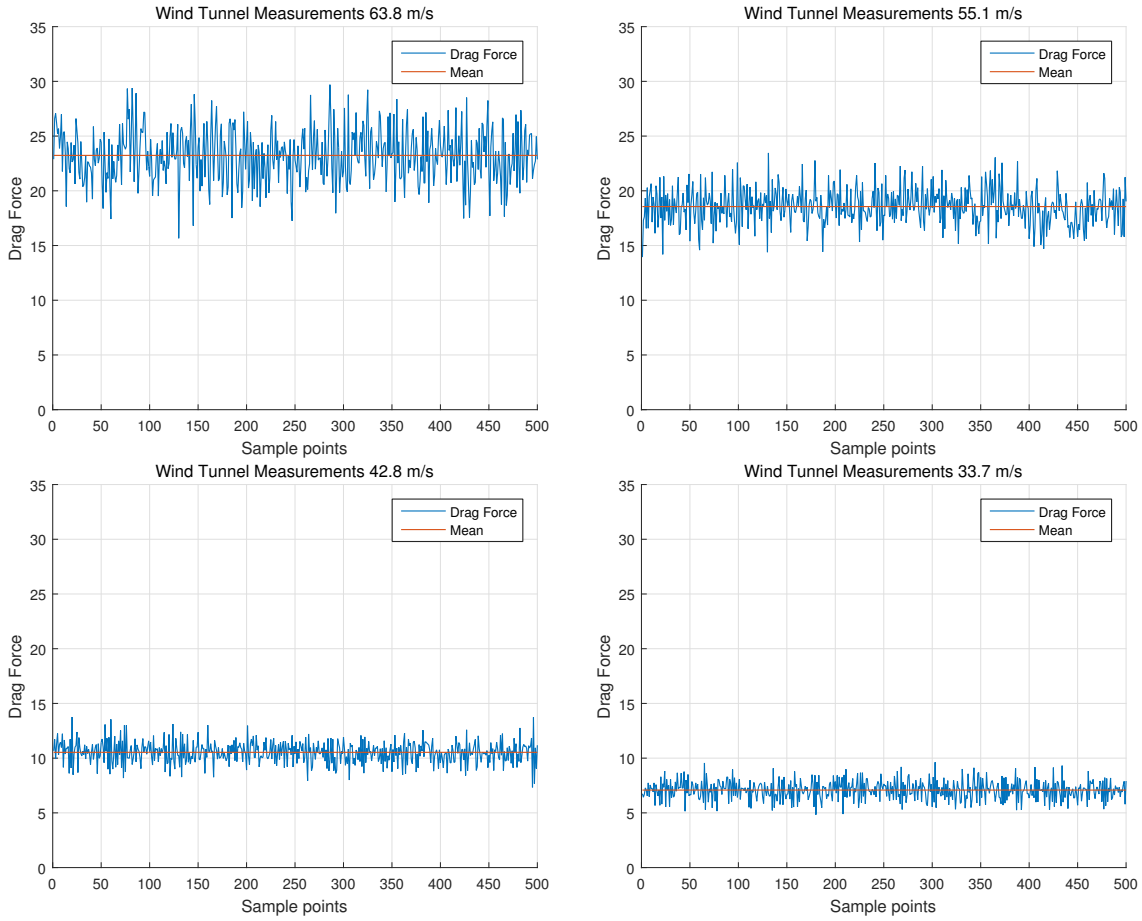

Figure 6.12: Drag measurement (in N) in the wind tunnel for different flow speeds.

	63.8 m/s	55.1 m/s	42.8 m/s	33.7 m/s
Mean Drag Force (N)	23.2353	18.5590	10.5318	7.0824
Standard Deviation	2.4391	1.6590	1.0277	0.9028
Drag Coefficient	0.8945	0.9579	0.9009	0.9772
Reynolds Number	$4.4582\,10^5$	$3.8503\,10^5$	$2.9908\,10^5$	$2.3549\,10^5$

Table 6.3: Data from the wind tunnel.

From the Figures 6.12 and Table 6.3, it can be seen that there are a lot of fluctuations and deviations in the data measured in the wind tunnel. For the high velocity cases, the standard deviation is considerably large, and could lead to some wide confident intervals for the C_D value, that reduces the precision of the measurement. From Figures 6.12 it is seen that the lower the velocity, the lower the deviation in the data. Due to the lack of information about the sample time in the device measuring the forces, a filtering of the noise and vibrations in the data can not be performed. The filtering of these variations would be beneficial in order to get clean measurements by eliminating the noise received by the data acquisition system.

In Figure 6.13, the drag coefficient dependence on the Reynolds number is shown, using the data obtained at different speed flows in the wind tunnel. From this figure, it is seen that within the range of Reynolds number of the order of 10^5 the C_D value does not show

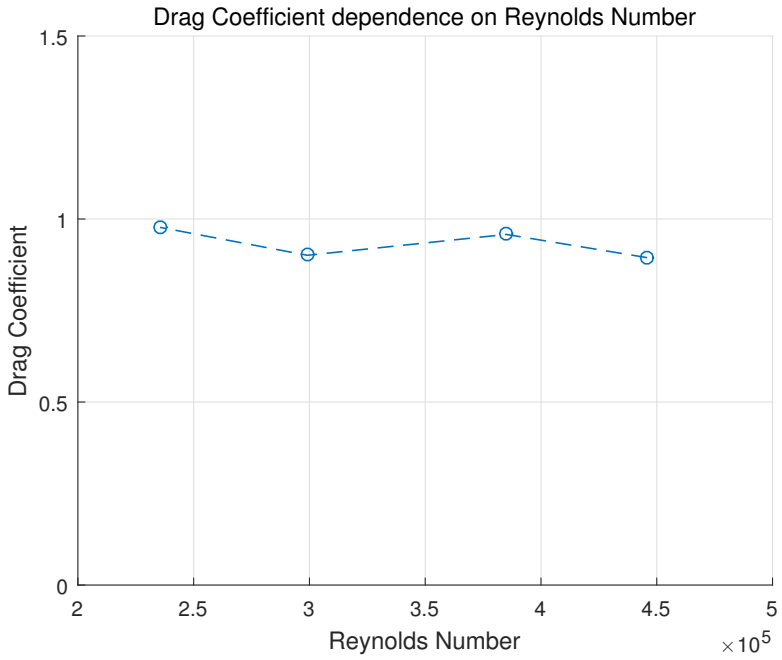

Figure 6.13: Drag Coefficient dependence on Reynolds Number

important differences. This is in concordance with what is expected for a bluff object in that Reynolds range, as for example the sphere, where the C_D is almost independent of the Reynolds number. Therefore, the drag coefficient at 63.8 m/s can be considered the same as at 63 m/s, and dynamic similarity in the testing can be considered as fulfilled.

As explained in detail in Appendix C, a high blockage ratio in the wind tunnel will result in a high source of errors in the data obtained. For this reason, and due a blockage ratio of 8.34%, different corrections will be applied to the drag coefficient obtained in the wind tunnel at 63.8 m/s. The different blockage correction that are used in this study are chosen because of its applicability to external aerodynamics over vehicles, and they are explained in Appendix C. In Table 6.4, the corrected C_D values with the different methods are shown.

Maskell Correction	0.7540
Tom and Heriot correction	0.7744
Improved Maskell Correction	0.7525
Uncorrected C_D	0.8945

Table 6.4: Drag coefficient corrections due to the blockage ratio.

From Table 6.4 it can be seen that the change of the drag coefficient due to the blockage ratio is quite significant (around 15% of difference). The C_D of the improved Maskell Correction is the one that is going to be used as the reference value for the drag coefficient in the wind tunnel. The corrected value for the C_D obtained in the wind tunnel is 0.7525. This one differs to the one in numerical simulations of 0.614 by 22.5%. This significant differences in the values may be explained because of the different source of errors in the wind tunnel and/or the errors in the CFD simulations.

As a method of validating the flow features obtained in the CFD simulations and in order to see how the flow behaves in a real case scenario, smoke and particle image visualization (PIV) is conducted over the scaled model in the wind tunnel.

6.2.2 PIV Results

The set-up for the is PIV explained in Chapter 5. This was consisting on a seeding system for the wind tunnel, a laser and a high speed CCD camera along with a computer for the analysis of the images is used. With this, the velocity flow field in the wake of the car have been captured and processed. In Figure 6.14, the scaled velocity field in the wake is shown. It should be noted that this velocity field is composed of 5 different processed images that have been overlapped.

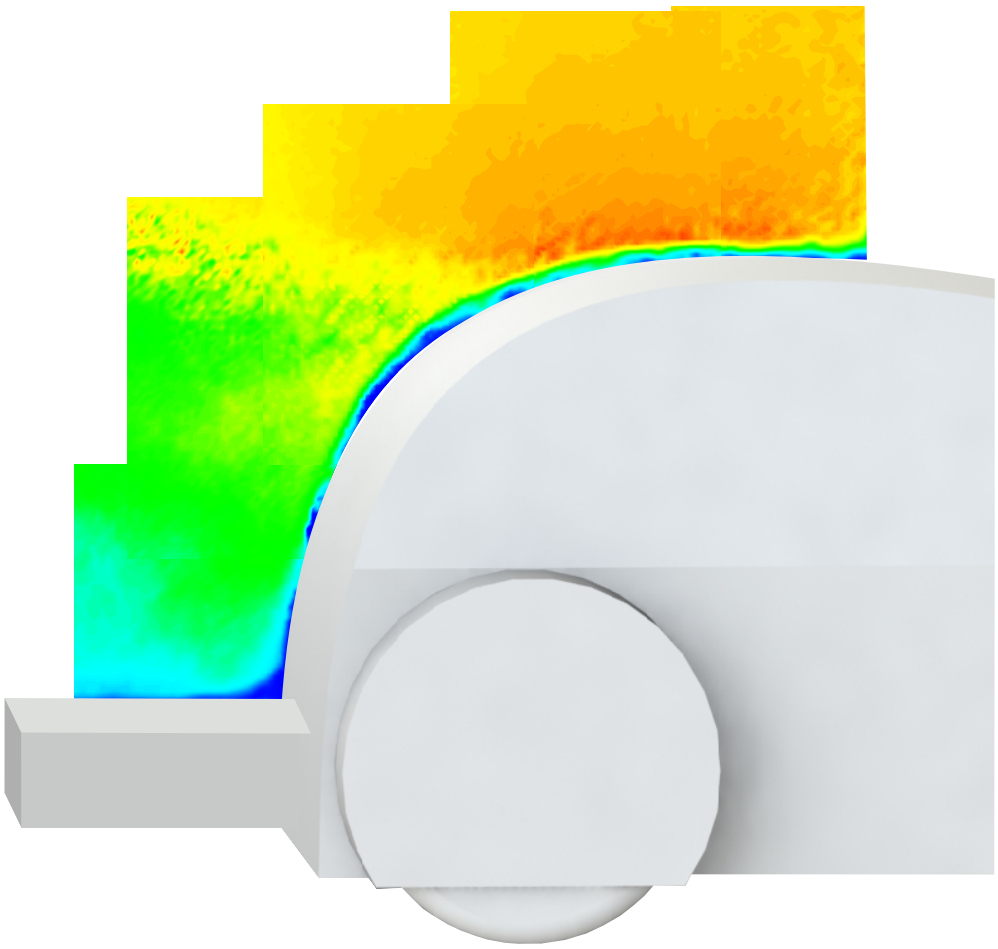

Figure 6.14: PIV visualization of the wake of the car.

6.2.3 Smoke Visualization

For a further study of flow features, the smoke visualization technique is also used in the wind tunnel. This method, explained in Chapter 5, allows to visualize the streamlines and how the flow behaves around the car. This technique is really useful to detect vortices and regions of separated flow around the object. With this the flow behaviour around some

areas of the vehicle was captured and recorded. Figure 6.15 shown the visualization of the flow over the top of the car.

Figure 6.15: Streamline visualization over the symmetry plane.

It is seen from Figure 6.15, that the flow is attached to the roof and follows smoothly the surface changes until the back end. Once reached this point, the flow is not able to follow the curvature and gets detached from the surface and the smoke is sparsed downstream of the point of separation. Further illustration of the behaviour in the upper surface of the car is shown in Figure 6.16, screenshots taken from the slow motion video that allows to observe some of the transient features present in the flow. From 6.16a, a rotating vortex

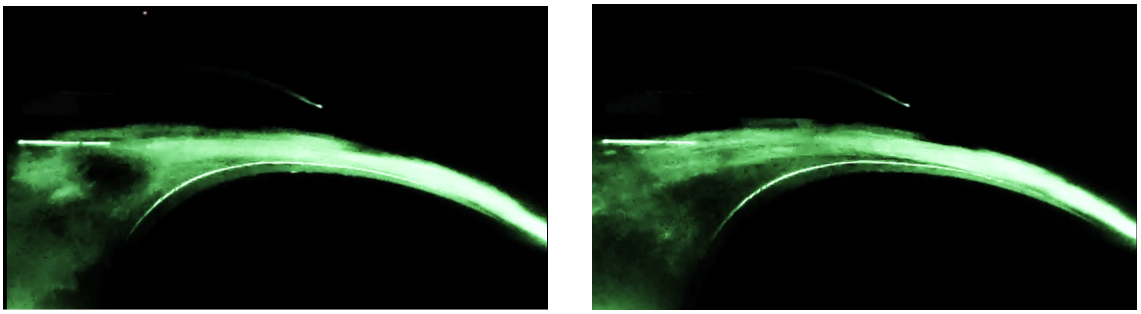

(a) (b)

Figure 6.16: Flow features on the wake of the car.

can be appreciated. From the analysis of the frames of the video, the rotating vortex moves and dissipates downstream. These vortexes are not always formed and sometimes the flow just follow a chaotic random behaviour in the wake. From another of the frames

of the video, shown in Figure 6.16b, the separated flow and the point of separation can be easily seen. The point of separation of the flow also presents a transient behaviour. It moves downstream and upstream depending of the behaviour of the flow in the wake and the rotating structures present on it. Comparing Figures 6.16a and 6.16b it can be seen that the point of separation is slightly different in both of them.

Another of the regions of interest, with detrimental effect on the drag are the wheels. Figure 6.17 shows a photograph of the behaviour of the flow around the car front wheelcase.

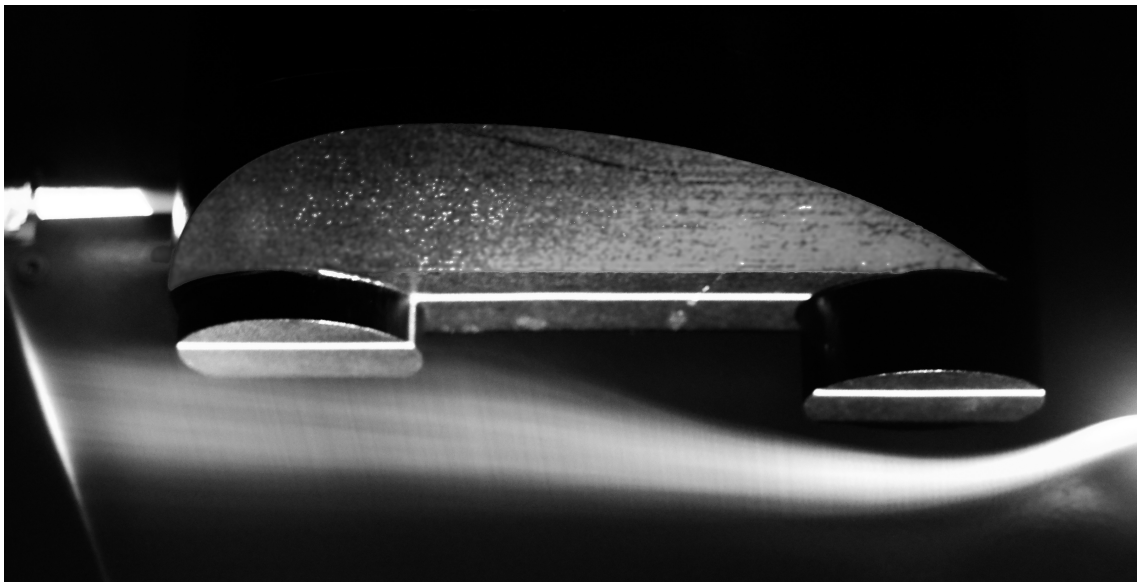

Figure 6.17: Smoke Visualization around the wheelcase

From Figure 6.17 it is seen that the sharp edge in the frontal wheelcase diverges the flow around it, detaching the flow from all the side of the vehicle. Also, the flow after being diverged away from the frontal wheel case, it comes closer to the surface of the car and collides with the back wheel case. Figure 6.18 shows a couple of screenshots of the slow motion video of the flow behaviour around the wheel case.

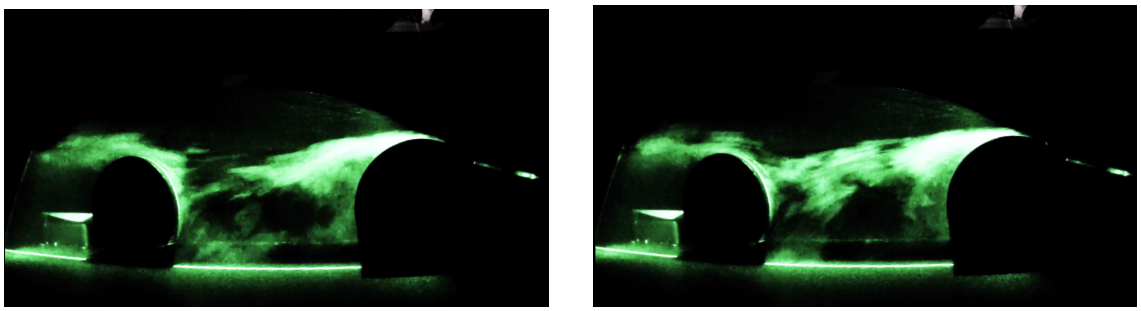

(a) (b)

Figure 6.18: Velocity and Turbulence on Wheelcase

The collision of the flow from the front wheel cases against the back ones can be seen from Figures 6.18. It can also be seen some kind of rotating structures, in the wake behind

the frontal wheel.

6.3 Validation of Numerical Simulations

This chapter serves to perform a validation and verification of the CFD model presented in Chapter 4. In order to do so, the results from the numerical and experimental analysis will be compared. A discussion about the differences obtained between the CFD model and the experimental data will be done.

6.3.1 Validation through PIV

One of the most challenging cases in a CFD simulation is the correct prediction of the flow separation. In order to perform a validation of the numerical model, the region of the wake obtained from the numerical simulation is compared with the experimental data obtained in the wind tunnel. It is in the region of the wake, where flow separation and the steepest gradients of pressure and velocity are expected. In Figure 6.19a, the scaled PIV velocity field with the numerical one are compared.

(a) PIV visualization of the wake of the car. (b) CFD visualization of the wake of the car.

Figure 6.19: Comparison of the velocity field for the PIV and the CFD.

From the comparison shown in Figure 6.19, it is seen that the main velocity features of the CFD matches correctly with the PIV flow field. Both numerical and experimental analysis shows great correspondence. It should be noted that in the analysis on the wind tunnel, the model was connected through a sting mount that allows the measurement of forces and keeps the car attached to the wind tunnel surface. This support was placed in the lower part of the rear back (as shown in Figure 6.19a) and influences the flow field around this region. Aside from this region, where the information is lost due the mount, the PIV is in excellence concordance with the results obtained in the numerical simulations.

Therefore, the CFD approach using in the simulations is considered to predict correctly the flow separation for steep rear back. This is a clear situation of a turning, highly strained

flow, one of the major problematic cases in the turbulence modelling field.

6.3.2 Validation through smoke visualization

The results obtained in the CFD software should predict accurately the characteristics of the movement of the air around the car. In order to validate this, the smoke visualization technique is compared with the flow features processed from the numerical simulation. In Figure 6.20, the features seen in the stream of smoke injected in the wind tunnel are compared with the flow features obtained from the CFD.

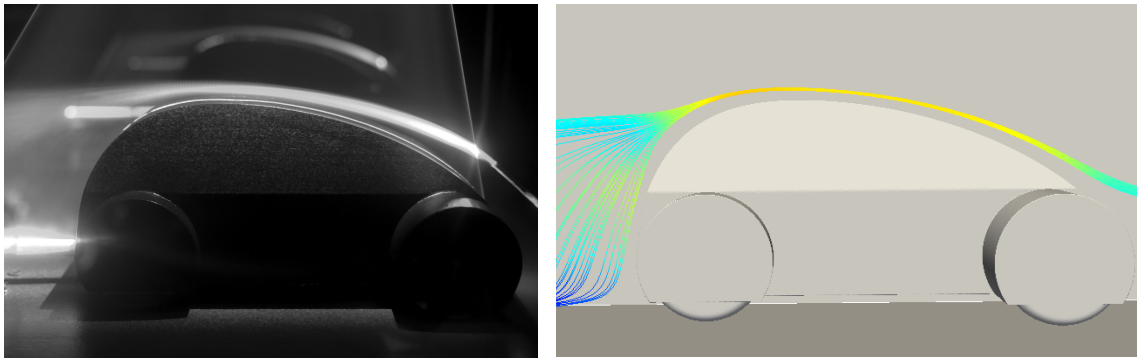

Figure 6.20: Comparison of smoke visualization and CFD in the wake.

From the smoke visualization the flow is attached to the roof and follows smoothly the surface changes until the back end. After that, the flow get detached and separated. Most of the air flows in a quite straight manner while some is sparse downwards. From the CFD simulation the flow features follow a similar pattern. The flow is also separated in the rear back but it seems that the separation happens a little bit downstream. The causes behind this small difference in the point of separation are difficult to evaluate. It should be noted that the speed in the wind tunnel while injecting smoke it was lower than the 63 m/s, and may provoke different flow patterns and separation points despite of the Reynold independence of the drag in these region of velocities (see Figure 6.13). Also, the precise point of the injection of smoke was not known, not allowing the perfect emulation of that location from the numerical results. It may be also a deficiency of the turbulence model Realizable κ-ϵ or some numerical issues created by the author in the set-up of the simulation.

Another example of the concordance of the flow features between the CFD simulations and the smoke injection can be seen from Figure 6.20, where the detachment of the flow in the side of the car is shown. For this case, the flow features matches almost perfectly, with only minor differences. The CFD simulation is able to predict the turning on the flow around the frontal wheel case correctly together with the collision of the flow against the back wheel case.

Regardless these small differences found in the two cases analysed, the main flow features are almost identical between the numerical simulation and the smoke visualization. Therefore it can be concluded that the CFD is able to predict correctly the flow separation, the turning in sharp angles and other flow features of the car.

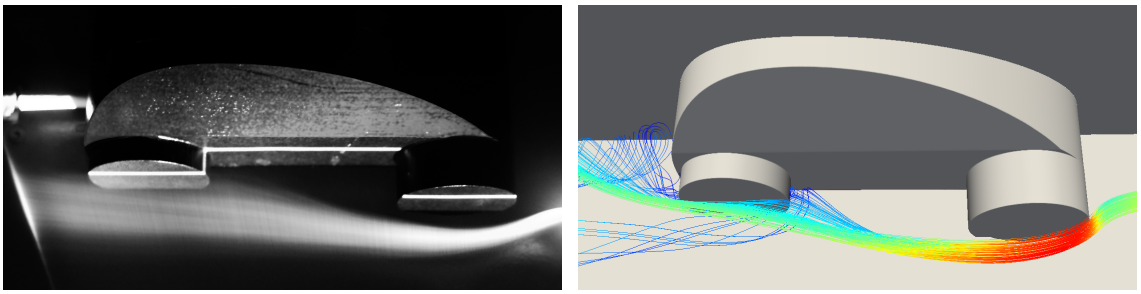

Figure 6.21: Comparison of smoke visualization and CFD in the side.

6.3.3 Validation through force measurement

The forces obtained in the numerical simulation should be also compared to the ones measured in the wind tunnel. In order to make a comparable judgement of the results, the C_D value of the numerical simulation will be compared with the corrected C_D value obtained from the wind tunnel. In Table 6.5 these results are presented.

C_D Wind tunnel (corrected)	0.7525
C_D Numerical simulation	0.614
Difference	+22.557 %

Table 6.5: Drag coefficient validation

The values for the C_D shown in Table 6.5 show a considerable difference between them. The drag coefficient obtained in the wind tunnel is 22.5 % larger than the one from the numerical simulation. Although in the same order of magnitude, the differences between them are substantial. As shown in the previous chapter in Table 6.3, the data from the wind tunnel shows really big fluctuations and variations. This reduces the precision of the data obtained in the wind tunnel and makes the comparison between both C_D values difficult to evaluate. Also, the sting mount where the model of the car is attached, due to its considerable dimension is expected to affect the flow and contribute to an increased drag. These factors together with that the wind tunnel of the university have not been optimised to perform aerodynamic test over vehicles, makes the C_D obtained in the wind tunnel a very uncertain value.

6.3.4 Discussion

Based on what have been presented in the validation through the force measurement, it is difficult to determine whether or not the drag coefficient of the CFD simulation is an accurate one. The author of this thesis expects the CFD simulations to be more precise and accurate than the wind tunnel testing. The numerical approach was based on some best practice guidelines [14] created from the information obtained during the year 2001 by the CFD-Subcommittee of the European Automotive Data Exchange. They conducted a benchmark study for the prediction of external aerodynamics [26], obtaining accuracies within the order of 2% with Realizable κ-ϵ for meshes three times coarser than the one used in this thesis. Therefore, as a much higher quality mesh is used for the CFD

simulation in this thesis, great accuracy would be expected on the numerical results. Also, the forces obtained from the wind tunnel, with the big variation on the measurement and the different possible source of errors, it can not be considered as a trustworthy source of data. Therefore, no reliable validation of the CFD results can be obtained from the comparison of the experimental data. Although no validation can be done from the forces of the wind tunnel, it serves to emphasize the extremely large value of the C_D of the current design.

6.3.5 Conclusion of the validation

Both the PIV and the smoke visualization have shown great concordance with the numerical results. The wake of the car with the separated flow obtained from the numerical simulation, the most challenging region to be accurately predicted in CFD, have shown a great correspondence with the experimental data. The numerical model was also able to predict accurately the velocity field and the important flow features around the car. The only discrepancy in the validation of the CFD model was found in the measurement of the forces, where a considerable difference of 22.5 % was found between the drag coefficients values.

As the differences in the drag results were possible due to variation associated with the measurement devices and the sting mount, and after the discussion done in Subsection 6.3.4, the CFD model can be considered to accurately and precisely predict the physical behaviour of the flow around the car. Because of this, the CFD model and numerical approach will be used exclusively for the analysis of the following designs and modification, and no experimental analysis will be conducted in other designs for the sake of time and the saving of resources.

Chapter 7

Modifications of the Current Car

As it was analysed in Chapter 6, the wheel cases, the sharp edges and the steep rear back of the current design have been proved to be a great source of turbulence generation, pressure and velocities gradients. These big changes are expected to be linked with a drag increase over the vehicle. As an attempt to improve the aerodynamic performance without completely restructuring the car, some add-on modifications are proposed and evaluated. The intent of these add-ons is to be able create a fast and cheap way of reducing the drag without the need of building a completely new vehicle. This chapter contains the results of these add-on modification and is divided in the individual analysis of these modifications. For the sake of comparison along the chapter, the general flow behaviour of the current car is illustrated in Figure 7.1, where the streamlines in the horizontal and vertical planes are presented.

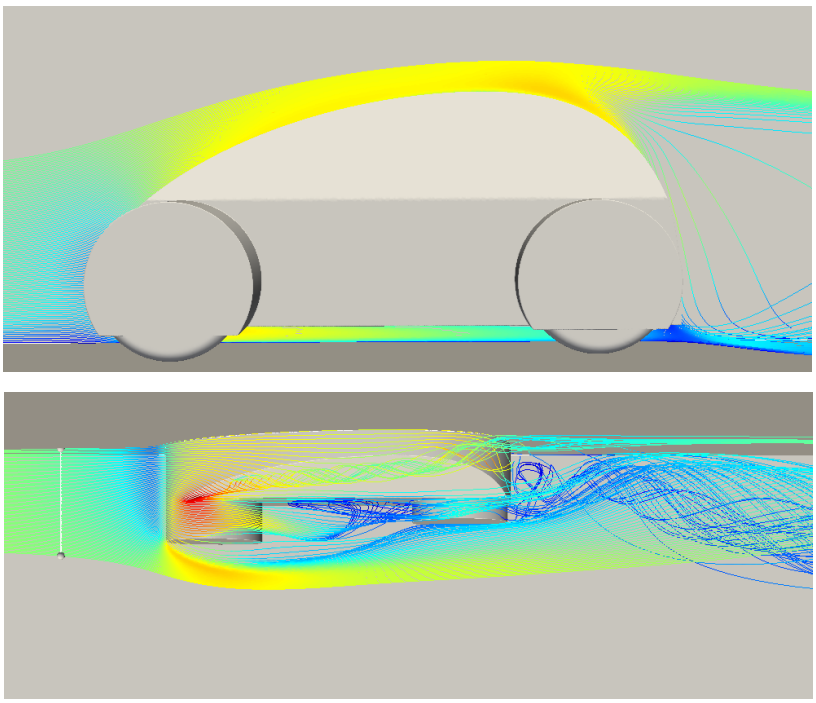

Figure 7.1: Flow features over the current car

The characteristic flow features of the car can be seen from Figure 7.1. This includes the flow separation in the rear back, the deflection of the flow due to the wheel cases and the vortex sheet created by the side edge. These detrimental flow features, sources of drag, will be aimed to be improved by the different modifications presented in this chapter.

7.1 Improvement 1: Wheel Skirt Add-On

As a attempt to improve the aerodynamic performance in the area of the wheels cases, a wheel skirt add-on is proposed. The design created is shown in Figure 7.2, with the aim of reducing the drag over the wheels of the vehicle.

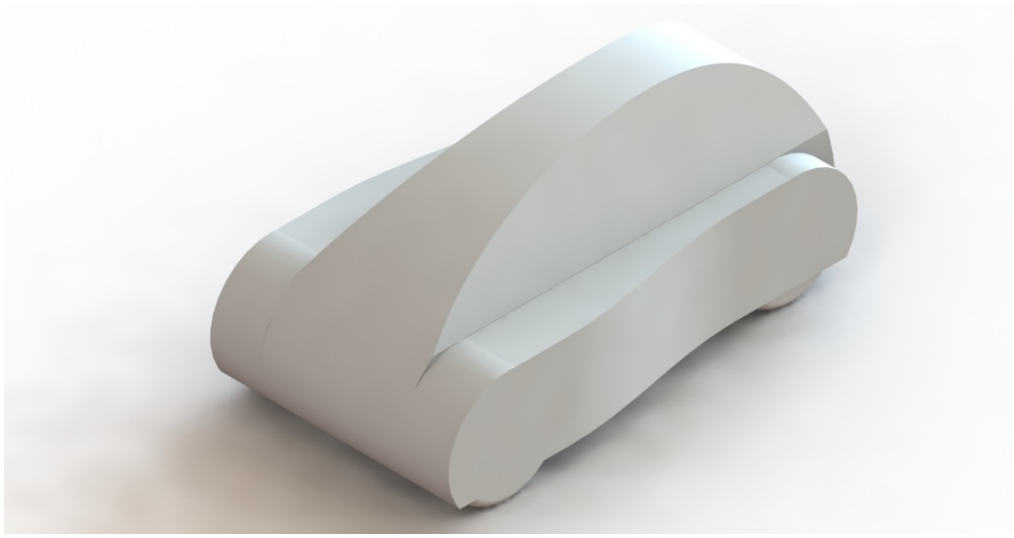

Figure 7.2: Evolution 1: wheel skirt add-on.

The design shown in Figure 7.2 is a simple surface cover of the area between the front and back wheel cases. Tangency and smooth transition should be ensured between the add-on and the actual surface of the car. With this modification the flow from the front wheel is not allowed to collide with the back wheel case. Although the extension will prevent the collision of the flow in back wheel case, it is not expected to prevent the separation seen in Figure 6.17 provoked by the sharp front edge of the wheel case.

A CFD simulation was conducted in this modified design to see the improvement that may be achieved. The set-up, solver and meshing approach is the same one used for the finer mesh of the unmodified car. The convergence of the simulation have been checked and the mesh independence have been assumed. Table 7.1 shows the comparison of the C_D and C_L values obtained from the numerical simulations.

	Wheel Skirts	Unmodified	Change (%)
C_D	0.54526	0.61434	-11.2446
C_L	0.34424	0.34633	-0.6035

Table 7.1: Drag and lift coefficient with the wheel skirts add-on.

Front Table 7.1, it can be seen that with this add-on the drag coefficient is reduced by 11.2%. The change in the drag is substantial, although the full potential of this add-on would be expected to be achieved if the edge of the frontal wheel cases together with of the edges of the add-on are rounded. Regarding the lift, the use of the add-on barely changes the lift coefficient.

The comparison of the flow behaviour with and without the wheel skirt is shown in Figure 7.3.

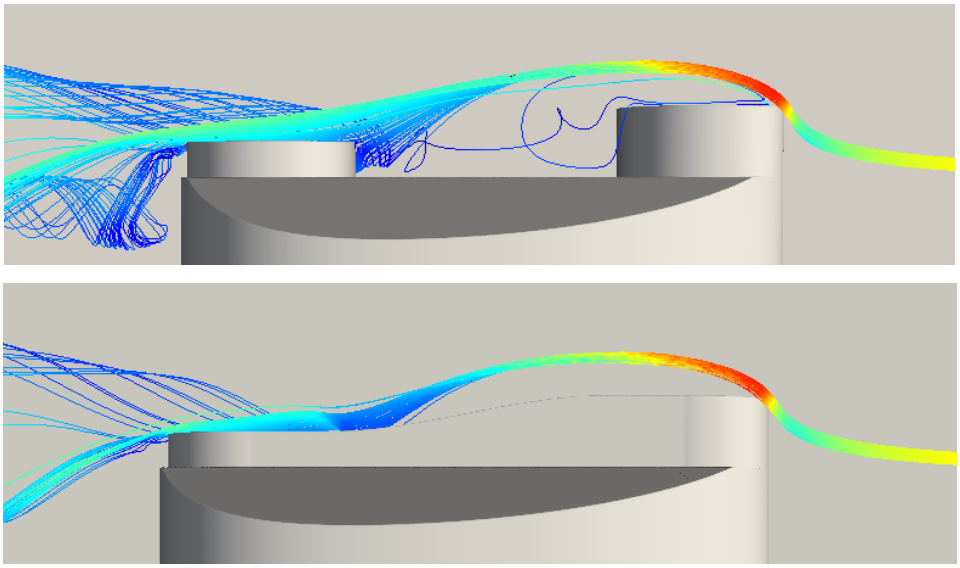

Figure 7.3: Comparison of flow behaviour around the wheel cases.

As it is seen from Figure 7.3, the wheel skirt prevents the collision of the flow with the back wheel case. The detachment of the flow seen in this figure is expected to reduce the potential effectiveness of drag reduction of the wheel skirt add-on. Attached flow on the side of the vehicle would be expected if a rounded edge in front wheel case of the vehicle is used, as explained in Appendix A and shown in Figures A.2 and A.1. This add-on is thought to be something that can be manufactured and implemented quickly onto the car with a very low cost of material and production.

7.2 Improvement 2: Extended Tail Add-On

In Subsection 6.1.6, the rear back of the car was found to be another of the major sources of pressure and velocities gradients and turbulence generation within the vehicle. As a attempt to improve the aerodynamics of the wake of the car, an extended tail add-on proposed. The design created is shown in Figure 7.4, with the aim of reducing the total drag by retarding the flow separation, decreasing the size of the wake and making the flow in the rear back of the vehicle to turn smoother.

This is a simple, non-optimized geometry and is simulated in order to see the possible scope of drag reduction with an rear back elongation of this kind. A CFD simulation is

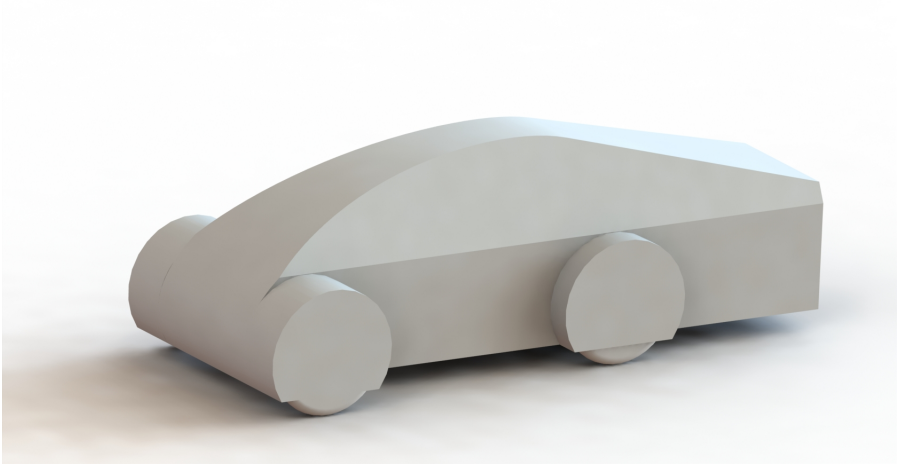

Figure 7.4: Evolution 2

carried out on the vehicle with the add-on. Table 7.2 shows the C_D and C_L improvement respect to the current car.

	Extended Tail	Unmodified	Change (%)
C_D	0.42748	0.61434	-30.416
C_L	$\approx$0.475	0.34633	+37.1524

Table 7.2: Drag and lift coefficient with extended tail.

From Table 7.2, it can be seen that the elongation of the back of the car can reduce notably the drag over the vehicle. This simple design, not optimized in terms of shape or inclination angles, achieves a 30% reduction. It have also a big influence in the lift, increasing the C_L value a 37%. This increase on the lift forces could lead to stabilities and handling problems at high velocities. Using a diffuser, down force would be generated, so the increased lift problem could be easily be solved.

The comparison of the flow behaviour with and without the tail extension is shown in Figure 7.5. The tail extension makes the flow leave the rear back of the vehicle in a smooth manner. The large rotating structures in the wake of the current car are also eliminated with the prolongation. Although a great reduction of the drag is achieved with the extension, the detachment of the flow in the side of the vehicle seen in the figure is expected to greatly reduce the potential effectiveness of the add-on.

After showing this large reduction of the drag with this simple construction, a thorough design and study of the geometry extension of the back would be expected to achieve significant further reductions of the drag. As these add-ons are supposed to be a temporal solution for this year competition in the Shell Eco Marathon, optimising the geometry would be extremely time consuming and out of the practical scope of this thesis.

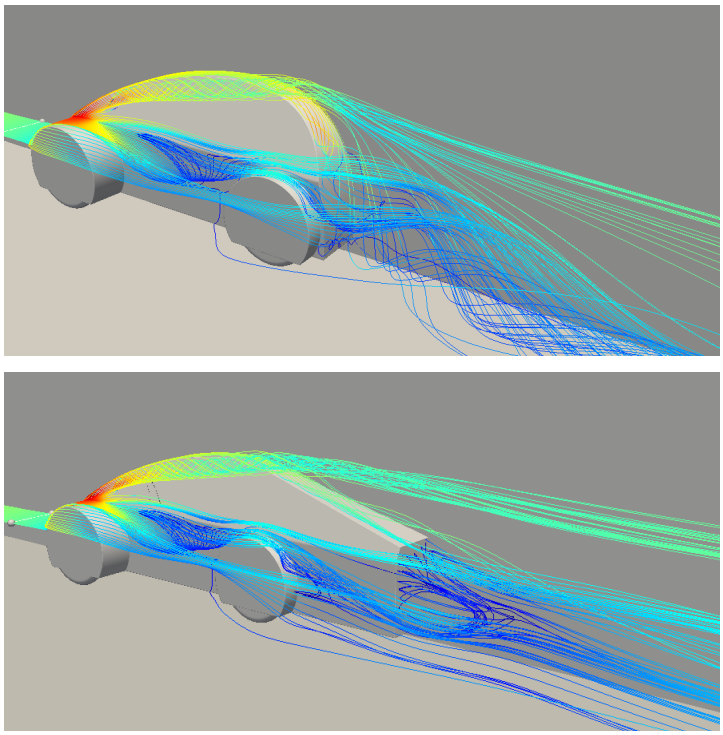

Figure 7.5: Comparison of flow behaviour around the rear back.

7.3 Improvement 3: Rounding of the Side Edge

As it was seen in Figure 6.8a and explained in Subsection 6.1.6, the sharp edge on the vehicle between the side window and the roof creates a rotating vortex sheet that detaches all the flow passing through it. The flow separation on all the side of the vehicle contributes negatively on the aerodynamic performance of the car. For this reason, the rounded of this sharp edge is proposed as a possible solution to prevent this flow separation. With this fillet, the flow is expected to shift smoothly from the top surface to the side one without the generation of a rotating vortex sheet. The modification proposed is shown in Figure 7.6.

As different radii can be chosen for the fillet, two simulations with fillets of radii 50 and 100 mm are conducted. An insufficient large radius is expected to act as a sharp edge, not being able to prevent the flow separation. Two CFD simulations were carried out for these two cases. Table 7.3 shows the results for the C_D and C_L for the different fillets on the side edge of the car.

	C_D	Change
50 mm fillet	0.46267	-24.688%
100 mm fillet	0.46736	-23.925 %
Unmodified	0.61434	-

Table 7.3: Drag coefficient of the modified design with the fillet

The rounding of the side sharp edge achieve a considerable drag reduction of 24%. This

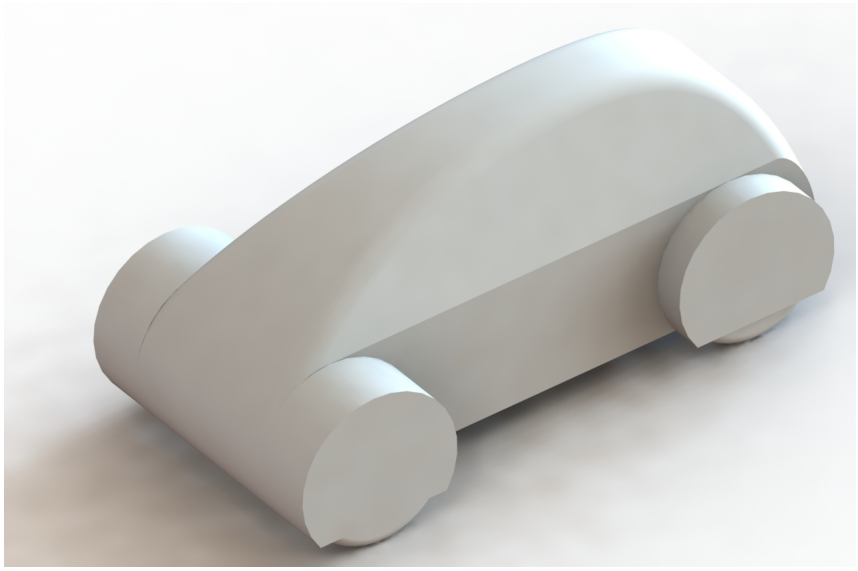

Figure 7.6: Evolution 3: rounding of side edge.

reduction on the drag is outstanding considering such a minor geometrical modification. These results illustrate the great potential for the drag reduction by the smoothing of the sharp edges present in the vehicle. The differences in drag between the 100 mm and 50 mm fillets are insignificant, and it is expected that the influence on the change of the radius follow a similar trend as the study in Figure A.2. From this, the drag is no longer reduce after a certain radius, as the maximum potential of reduction have been achieved. With this simulation, and seen that the drag does not change between 50 mm and 100 mm, the maximum drag reduction can be assumed as accomplished. In Figure 7.7, the comparison of the flow behaviour around the edge is shown.

As seen from Figure 7.7 the smoothing of the edge avoids the creation vortex sheet explained in Section 6.1.6. This prevent the separation of all the flow in the side of the vehicle, with the consequent enhancement on the drag reduction. As explained in Section 7.2, if the flow is attached to the side of the vehicle, as it was accomplished with this modification, further reduction on the drag with the tail extension would be expected.

7.4 Improvement 4: Vortex Generator

As already explained, the rear back of the car was found to be one of the main sources of drag generation. The tail extension analysed in Section 7.2 have proved a great potential of drag reduction by retarding the flow separation. Another possible method of drag reduction in the wake is the instalment of a series of vortex generators in the rear back of vehicle, just before the flow detaches. The vortex generator (VG) is an aerodynamic device adhered to the surface of the body that creates a rotating vortex when the fluid pass through it. This vortex creates a swirling flow that increases the energy in the boundary layer by mixing it with the high energy flow of the free stream. With this, the momentum in the boundary layer is increased, expecting a delaying on the flow separation.

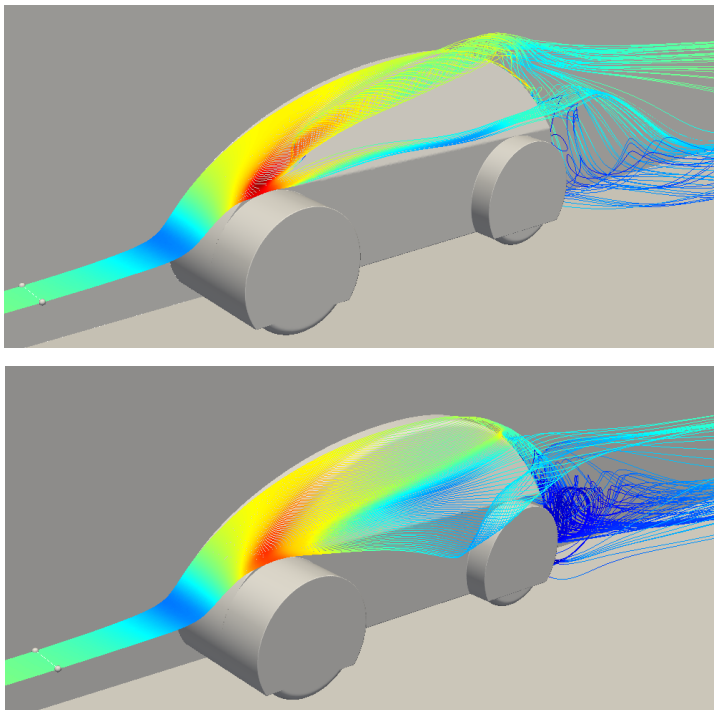

Figure 7.7: Comparison of flow behaviour around the side edge

In Figure 7.8, the vortex generators designed and placed on the roof of the car are shown. It should be noted that these VG's have not been optimized in shape, highness or position. For a good VG, different geometries must be experimentally tested. Also the exact separation point should be calculated as well with the thickness of the boundary layer in that region. This design is far away from being an optimal one, and this simulation is only done in order to show the potential of drag reduction with a device of this kind in the current car.

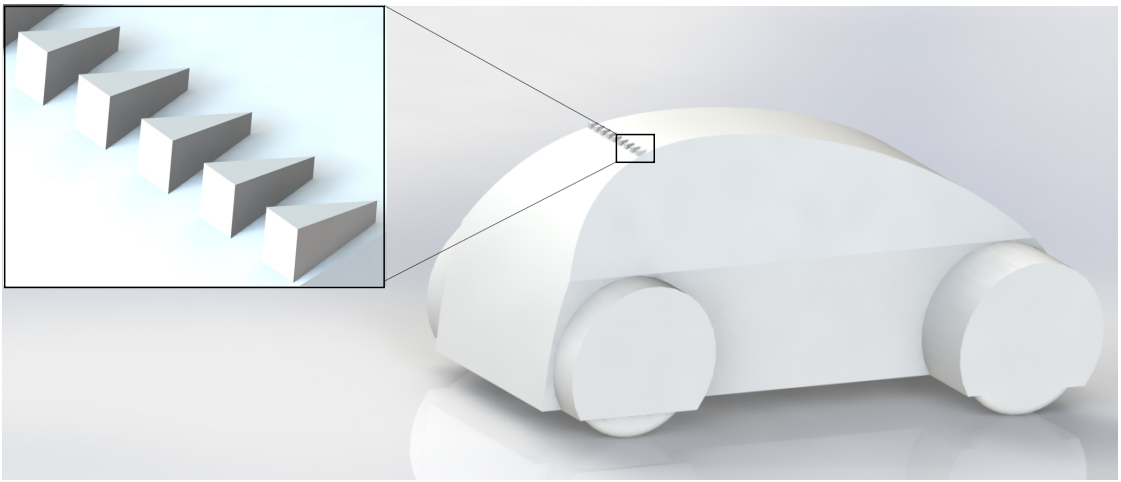

Figure 7.8: Evolution 4: Vortex Generator

A CFD simulation was carried out for the current car with the VG's. Table 7.4 shows the results of C_D and C_L obtained in the numerical simulation with the addition of the

vortex generator.

	VG's	No VG's	Change (%)
C_D	[0.5338,0.5850]	0.61434	-13.11 to -4.78
C_L	[0.1224,0.3301]	0.34633	-64.66 to -4.69

Table 7.4: Drag and Lift Coefficient with Vortex Generators

From Table 7.4 it is seen that these non-optimized VG's can diminish the drag and the lift considerably, up to 13% for the drag and 64% for the lift. The flow with the vortex generators shows a considerably transient behaviour, with big variations for the lift and drag. This abrupt changes in the forces over the vehicle could create instabilities and vibrations while driving. Special care should be taken when placing these VG's in the car if vibrations and instabilities want to be avoided. Figure 7.9 shows a comparison of how the flow behaves in the wake of the car with and without the VG's.

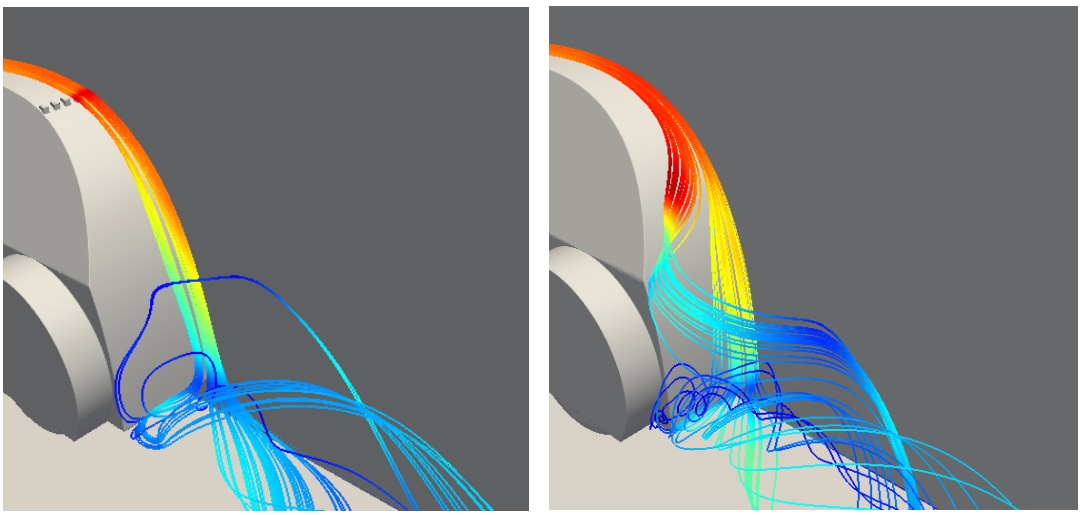

Figure 7.9: Comparison of flow behaviour with and without the vortex generator

From this figure it can clearly be seen that the VG's in the roof of the vehicle are able to keep the flow attached to the rear back of the vehicle. Whilst for the case without the modification, the flow detaches and whirls in the wake of the car. The speed of the flow stream also decreases more slowly in the case with the VG's, proving that they are providing more energy to the flow close to the surface of the car. The vortex generators are therefore, a cheap and fast solution with a huge of potential of archiving great drag reductions with the use of such a small device.

If this modification wants to be applied to the current car for the competition, the author recommends to use commercial VG's that have been already studied and optimised. With this high quality VG's, that can also be 3D printed easily, higher drag reduction and lower fluctuations would be expected. It should be noted that these devices are an alternative to the tail extension. If both the tail extension and VG's would be beneficial to the drag reduction must be studied. Although the VG's have been only analysed for the rear back it could be also recommended to place them in any region where the flow is about to get separated from the surface. The wheel cases are an example of the possibility of instalment

of these devices, as it could move downstream the separation point around the cylindrical shape of the cases. In order to ensure the validity of this hypothesis, simulations and studies must be conducted. It should be noted that no reliable statements can be affirmed in such a complex 3D flow without a cautious analysis.

7.5 Improvement 5: Combination of Fillet and Extended Tail

In order to check the combination of some of these modifications, a last case is simulated. This case consist on a modified extended tail plus the fillet of different edges in the vehicle. The edges that have been rounded are the side edge on the car previously studied and the borders of the wheel cases, both the front and rear one. This last modification have been done with the intention of preventing the complete separation of the flow in the side of the vehicle, as it was seen from Figures 6.17 and 7.3. The design created is shown in Figure 7.10, with the aim of studying the behaviour of several components together, and if any kind of synergy emerges from their combination. It is important to notice that the extended tail is not the same as the one analysed in Section 7.2. As the previous design resulted on an increase of 37% of lift, this one was designed with a spoiler in underbody. This change would be expected to reduce the amount of lift by creating down force into the vehicle. Also, the width in the extended tail was gradually reduced, creating the so-called boat tail.

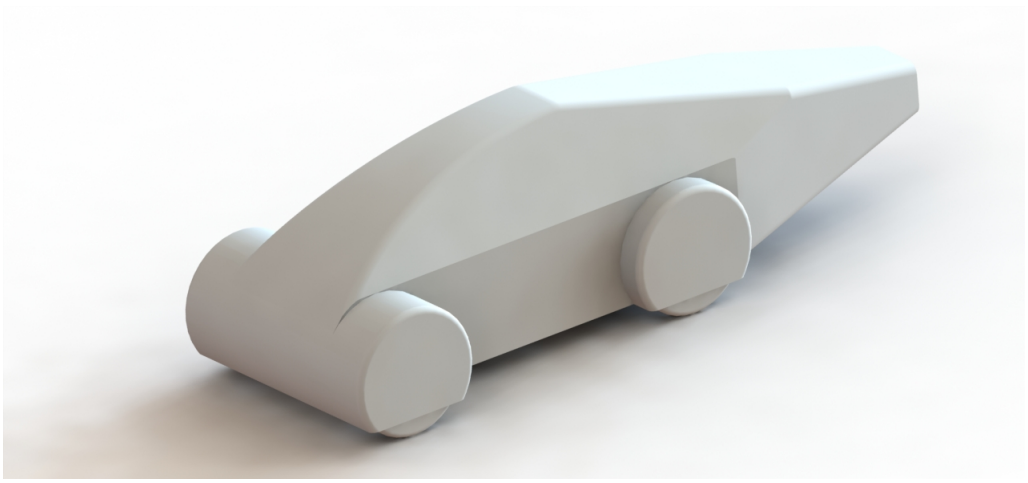

Figure 7.10: Modification of the current car including several edges rounding and a extended tail.

A CFD simulation was carried out for the current car with these modifications. Table 7.5 shows the results of C_D and C_L obtained in the numerical simulation with the addition of the extended tail and the edge rounding.

	Modified	Unmodified	Change (%)
C_D	[0.3862 to 0.4084]	0.61434	-33.522 to -37.136
C_L	[-0.0590 0.0326]	0.34633	-90.595 to -117.046

Table 7.5: Drag and lift coefficient of the modified design with the extended tail and the edge rounding.

The rounding of the edges together with the extended tail achieve a considerable drag reduction of up to 37%. The flow still shows a considerably transient behaviour, with the drag coefficient oscillating between 0.39 and 0.41. Regarding the lift, it is seen that the car no longer generates a considerable amount of positive lift, but instead oscillated around the point where no lift or down force is created. That means that the apparent weight of the vehicle will be constant throughout all the speed ranges.

With an average C_D value of 0.40 for this improved design, an great reduction of around 35% of the drag have been achieved without the complete restructuring of the car. This value for the drag coefficient is now comparable with some mid-size vans, SUV and some sedans available in the market, but still far away from a satisfying design for ultra efficient car.

7.6 Comparison of the improvements

In Table 7.6 the comparison of the C_D and C_L values attain with the modifications are presented. These values are the averaged ones, as some of the design presents strong transient behaviour that makes these coefficients to fluctuate. They are also arranged from the lower to the higher drag reductions achieved.

	C_D	Change in C_D (%)	C_L	Change in C_L (%)
Current design	0.614	-	0.346	-
Vortex Generator	0.559	-8.943 %	0.226	-34.658
Wheel Skirts	0.545	-11.245 %	0.344	-0.604
100 mm fillet	0.467	-23.925 %	0.015	-95.665
50 mm fillet	0.463	-24.688 %	0.061	-82.370
Extended Tail	0.427	-30.416 %	0.475	+37.152
Fillet + Tail	0.397	-35.323 %	-0.013	-103.811

Table 7.6: Comparison of drag and lift coefficient for the different modifications

Ranging from 9% for the non-optimised vortex generators up to 35% for the fillet and extended tail, all the designs proposed in this chapter have resulted in a satisfactory drag reduction. Further drag reductions may be expected for the vortex generators and the extended tail if their geometry is optimised. Regarding the lift, the modifications created also big changes on the the lift. Some of the modifications reduced the C_L more than 100%. This was the case for the fillet and extended tail where some down force was produced. In the rest of the cases, positive lift was produced, and some of the design reached an increased lift of 37 % with respect to the current design. Also, some of this modifications presented a heavy transient effect, with considerable cyclic variations in the drag and lift.

For better illustration of the changes in C_D and C_L, Figure 7.11 is presented. In this plot, the drag and lift coefficients are shown in a bar graph. Also two reference lines for representative C_D values of a commercial cars are displayed. One of this lines corresponds to the C_D of the Volkswagen XL1, an aerodynamic record-breaking car, designed exclusively with the aim of increasing its fuel efficiency. On the other reference line is the C_D for one of the least aerodynamic designs in the market, the Hummer H2.

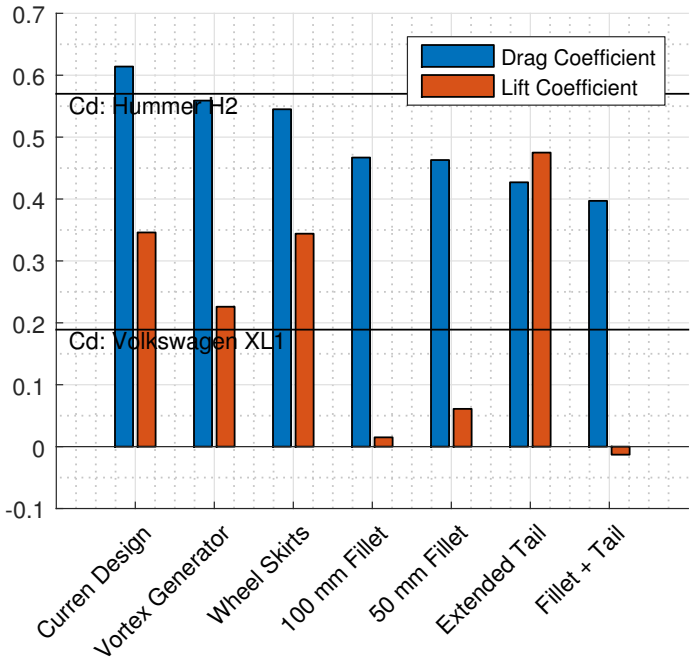

Figure 7.11: C_D and C_L comparison of the different modifications.

From this figure, although the drag coefficient can be reduced considerably with some complements, it is still far from being a aerodynamic design as the Volkswagen XL1. With the addition of the extended tail and the fillet of the edges, the car has a C_D value slightly lower than 0.4, that can be comparable with some regular cars on the market. Considering that these cars are usually designed mostly based on the aesthetics instead on the aerodynamics, the modified designs are concluded to be not satisfactory for an ultra efficient car. The modified design, although improved considerably is still far from the expected values of a proper aerodynamic designs, that have a C_D around 0.15 - 0.2. For this reason, a completely new design for the car will be proposed, with the aim of reaching a competitive C_D value.

Chapter 8

New Car

In Chapter 7, several add-on modifications have been designed and tested aiming for a drag reduction of the current design. From an original C_D value of 0.614, the modifications were able to reach drag reductions up to a 35%, achieving a improved C_D of 0.397. This modified car, significantly much better than the current design, it is still not suitable for a car participating on a ultra-efficient competition. As the add-on modifications are restricted by the baseline shape of the car, it limits greatly the potential of drag reduction. For this reason, if a competitive design wants to be achieved, a complete re-design of the car must be done.

This chapter contains a completely new design for the car based on the results obtained from the analysis of the current car and its modifications. After the new design have been tested, a couple of studies regarding geometrical changes are done. This is done with the goal of further understanding how they affect the flow behaviour. Also, a second new design, based on these studies and previous research within the automotive industry is presented and analysed.

8.1 New Design 1

A completely new outer design for the car have been proposed based on the results of the analysis of Chapter 6. The design, shown in Figure 8.1, does not use individual wheel cases, does not have any sharp angles and the rear back goes down gradually. All these changes have been done in the regions found to be more harmful to the drag contribution. This design is expected to behave gently with the flow, retarding the flow separation the further downstream as possible in order to obtain a low drag coefficient.

As done with the actual design of the car, a numerical simulation is conducted in order to analyse the aerodynamic performance of this new design. Different CFD simulations are done in order to ensure the validity and the mesh independence of the solution. The numerical approach is the same one explained in Chapter 4. The information regarding the mesh, model used and the solution of each of the simulations is presented in Table 8.1.

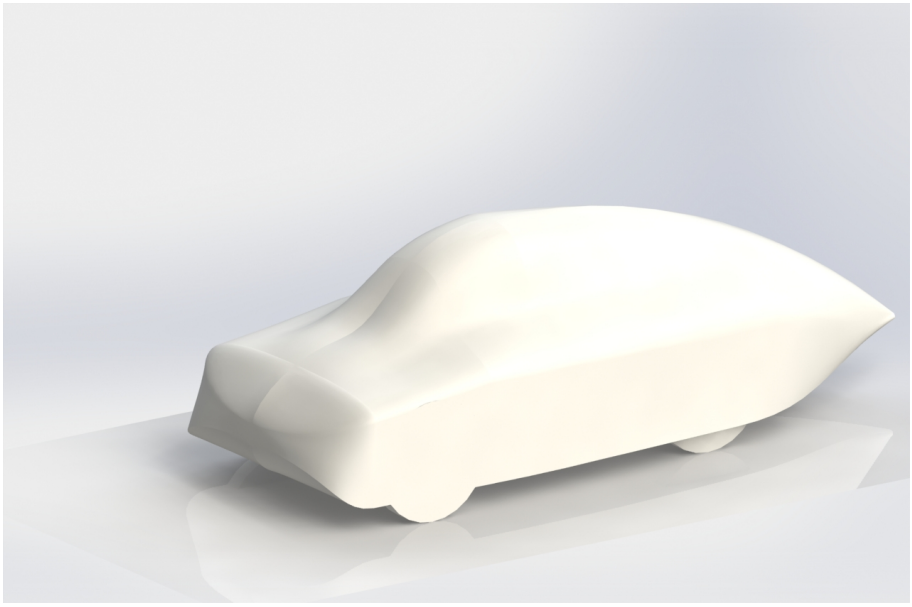

Figure 8.1: New Design

	Mesh 1	Mesh 2	Mesh 3	Mesh 4	Mesh 5
Nodes	$1.552\,10^6$	$2.438\,10^6$	$2.948\,10^6$	$3.610\,10^6$	$3.610\,10^6$
Elements	$7.429\,10^6$	$11.801\,10^6$	$14.149\,10^6$	$17.979\,10^6$	$17.979\,10^6$
Face Sizing	10 mm	8 mm	7 mm	7mm	7mm
Body Sizing	50 mm	40 mm	40 mm	30 mm	30 mm
Growth Rate	1.05	1.05	1.05	1.05	1.05
Model	Real. κ–ϵ	Real. κ–ϵ	Real. κ–ϵ	Real. κ–ϵ	RSM
Drag Coefficient	0.1282	0.1275	0.1273	0.1272	0.1290?
Lift Coefficient	0.1413	0.1347	0.1329	0.1331	0.1493?

Table 8.1: Number of cells.

Again, whether to choose or not one of these solutions for the drag and lift coefficient rely upon if the solution is not dependent of the discretisation process and if it has converged.

8.1.1 Mesh Independent Study

A mesh independence study have been performed for this new design. The number of elements and the refinement in the mesh have been gradually increased until the solution is barely changing. The mesh independent study for the drag and lift is presented in Figure 8.2. In the last three simulations only the 4^{th} decimal number changes. With a change in the C_D smaller than 0.08%, the solution of the mesh 4 of 18 million elements is considered mesh independent.

8.1.2 Quality of the Mesh

The quality of the mesh, presented in Table 8.2, measured with the skewness and aspect ratio of the cells, can also be considered satisfactory all over the computational domain based on the meshing recommendations given by Ansys [4].

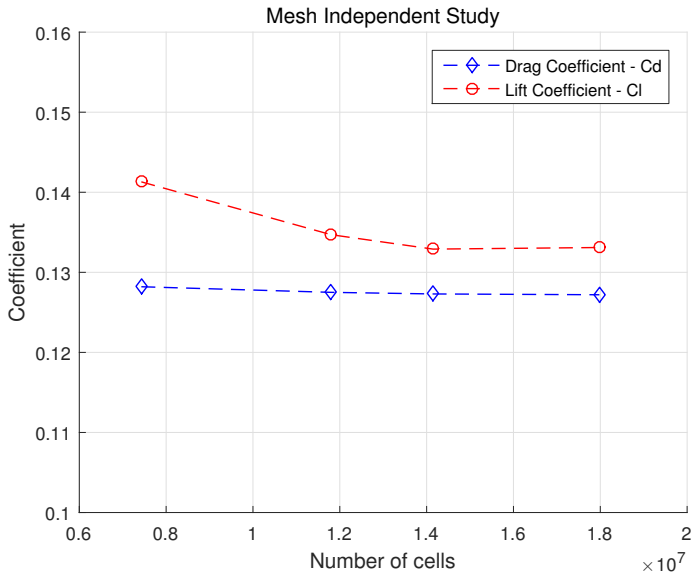

Figure 8.2: Mesh independent study for Realizable κ–ϵ.

	Skewness	Aspect Ratio
Minimum	$1.1857\,10^{-4}$	1.1616
Maximum	0.85612	76.679
Average	0.20212	1.9909
Standard Deviation	0.1106	0.96972

Table 8.2: Skewness and aspect ratio quality for Mesh 4.

8.1.3 Convergence Study

As done with the current design of the car, in the CFD simulations, the convergence must also be ensured. Figure 8.3 shows the convergence process of the mesh of 18 million elements. From this figure it is seen that the solution reaches a steady value for both the drag and lift at around the 350 iterations. Therefore, in addition to being mesh independent, the solution is also converged.

8.1.4 Turbulence Model Comparison

As the turbulence model may also be a source of errors in the field of CFD, a simulation using the Reynolds Stress Model (RSM) is conducted to check that no big changes appear between different models. In the last column of Table 8.1, the information regarding the solution of the RSM is presented. From this, is can be seen that the RSM only changes the drag coefficient in the 3^{rd} decimal number, with changes smaller than 1.5 %. The values for both RSM and Realizable κ–ϵ are pretty close. For the lift coefficient, the value of the RSM is 12 % higher than in the Realizable κ–ϵ. As the drag is our main parameter of focus and not the lift, no more refinement and comparison between the RSM and Realizable κ–ϵ will be done. Care should be taken in the studies where the lift becomes the main parameter of interest.

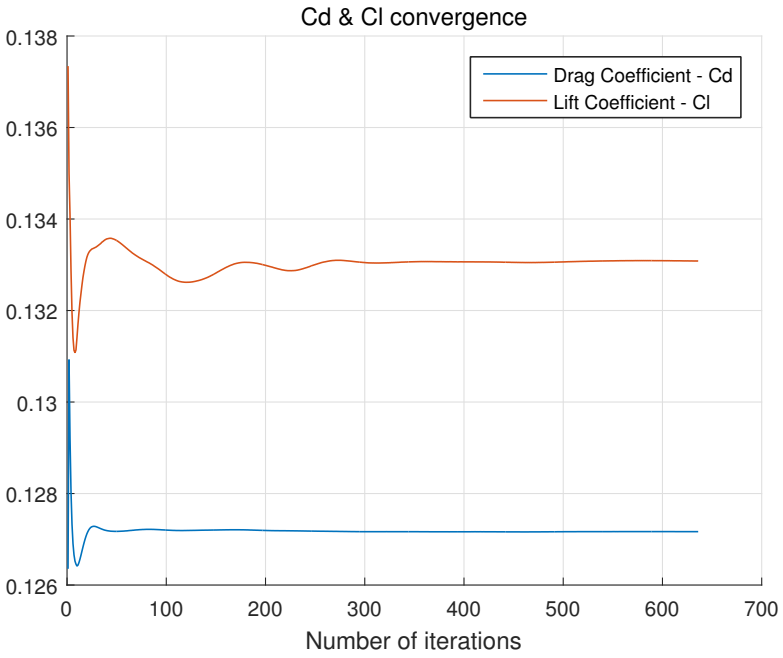

Figure 8.3: Convergence of the 17M-elements mesh (Mesh 4).

8.1.5 Results

After discussing the mesh independence and the convergence of the solutions, the results from the Mesh 4 of Table 8.1 are chosen. The solution of this mesh, of almost 18 million elements, proved to be mesh independent and converged, results in a drag coefficient of 0.127 and a lift coefficient of 0.133. No transient nature of any of these parameters have been perceived from the numerical simulations, although a transient analysis should be ideally done in order to certify this. In Table 8.3, the forces acting over the vehicle, both pressure and viscous drag are shown.

Pressure Force	2.2212 N
Viscous Force	1.5274 N
Total Force	3.7486N

Table 8.3: Drag forces in the car at 7 m/s.

The pressure drag was reduced an 85% respect to the current design from 14.83 N to only 2.22 N. This pressure drag contribution have changed from being 95% of the total drag to only a 59%. Meanwhile, the viscous force have been increased a 112% from 0.72 N to 1.53 N. This behaviour was expected by the streamlining of the design. This aims reducing the pressure drag by increasing the surface area with the collateral by incrementing slightly the viscous drag.

In overall, the total force over the vehicle was greatly reduced from 15.56 N of the current design to 3.75 N of this new one. This is an outstanding reduction of 76% on the total force created by the air over the vehicle. Regarding the drag coefficient, the new car have a C_D value of 0.127, reducing a 79% the value of the current car of 0.614. With a frontal area of 0.982 m^2, the C_D·A has a value of 0.125 m^2.

Despite of the excellent C_D value obtained, the analysis of the flow features and all the information obtained from the CFD simulation is essential for the understanding what makes this a good design. Also it is important to find any region that may be still detrimental for the drag. Knowing the causes that produce the drag makes possible to modify the design with the goal to be improved. In the next Subsection 8.1.6, a general analysis of data obtained from the simulation is presented. These visualizations of the vector fields will allow to understand how the flow behaves around the car.

8.1.6 CFD Solution Fields

From the CFD simulation, the pressure and velocities fields along with all other variables characterizing the flow are obtained in the solution. In Figure 8.4, the most relevant solution fields in the symmetry plane and surface of the car are presented.

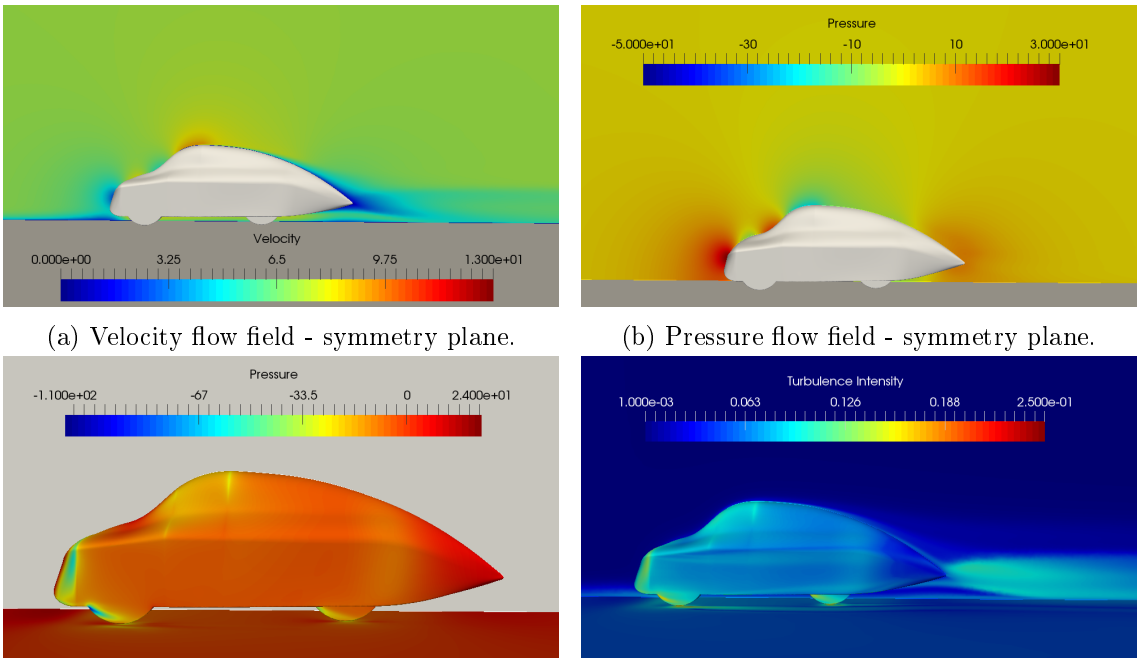

(a) Velocity flow field - symmetry plane.

(b) Pressure flow field - symmetry plane.

(c) Pressure flow field - surface of the car.

(d) Turbulence intensity field

Figure 8.4: CFD solution fields for the new design.

Several general flow features will be explained in order to obtain a basic understanding of the aerodynamic performance of this new design.

Symmetry Plane Features

Different characteristics of the flow can be found in diverse regions of the symmetry plane:

1. **Front end**. In this region the particles of air will slow down due to the bluff front, creating a low velocity area that can be seen from Figure 8.4a. This change of velocity can be linked with the increase of the pressure seen in the Figure 8.4b.
2. **Hood and Windshield**. The area over the hood and the wind-shield presents big gradients of pressure and velocity. The pressure of Figure 8.4b shows that in the vicinity of the inflection point between the hood and the windshield, there is pressure

decrease. This reduction is located just between two areas of high pressure and can be linked with the increased velocity seen in the same spot in Figure 8.4a.

3. **Top**. The upper region have an increased velocity magnitude in the region around the maximum height of the vehicle. From there to the rear back, the velocity decreases gradually. Near to the end of the vehicle and close to the surface, the velocity magnitude is reduced down to almost 0 m/s. This is probably due to the loss of energy in the boundary layer and a possible flow separation. Regarding the pressure, the top of car shows a region of reduced pressure all over the roof that propagates to a considerable distance above the roof. This region of low pressure finish suddenly into a area of high pressure close to the trailing edge of the vehicle. The point of transition from the zone of low pressure into the high one may be related with the possible point where the flow detaches. This point matches with the point in the velocity field where velocity close to 0 m/s starts to appear in the rear back.
4. **Wake**. The wake of the car shows a region of high pressure that smoothly transition to the atmospheric at some small distance downstream. Regarding the velocity, there is relatively narrow wake where the velocity magnitude is close to 0 m/s. Outside this region, the velocity changes pretty fast towards the free stream value. The narrow wake present is a positive sign of a good aerodynamic performance. From Figure 8.4d, it is seen that is in this region where most of the turbulence within the symmetry plane is created, but with a much more smaller values than in the steep rear back of the current design shown in Figure 6.9.

Surfaces Features

Regarding the surface of the car, several interesting features have been found. First of all, in the nose of the car there is big changes on the pressure. It transitions from high values into low ones in a small distance. This change occurs in the turning from the front to the side as it can be seen from Figure 8.4b.

From this figure, it can also be seen some small traces with lower values of pressure in the windshield and top of the vehicle. These lines of low pressure are result of the imperfections on the creation of the surfaces in the CAD software. From Figure 8.4d, it is seen that this imperfections contributes somehow to the turbulence creation.

Another region of interest in the surface of the car is the wheel area seen from Figure 8.4b. The wheels create regions of low pressure in the frontal area of them, specially in the corner between them and the frontal underbody. They are also a main source of turbulence, as it can be seen from Figure 8.4d.

General Flow Behaviour

In Figure 8.5, the general flow behaviour around the vehicle is shown.

From this figure, it is seen how nicely the flow behaves around the car compared with the actual design shown in Figure 7.1. The flow, both in the upper and side areas, follow the surface of the vehicle smoothly, with no apparent major flow separation. This behaviour is

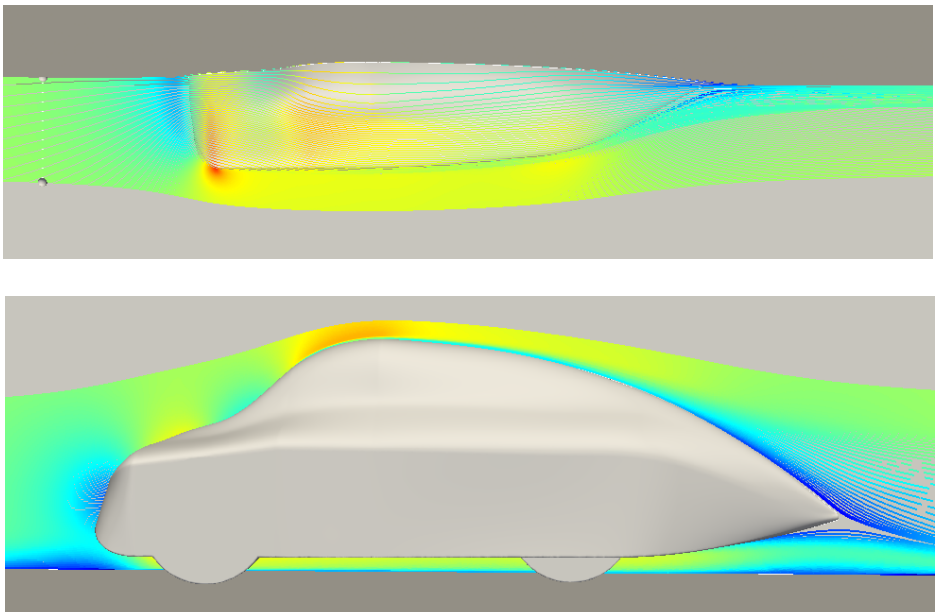

Figure 8.5: Flow over the car

a clear example of how a good design should behave such that the drag is minimized. The only area where the flow may create a detrimental situation for the drag is in the lower part of the rear tail of the vehicle, where the flow in the last portion is not completely attached to the surface.

The new design, with a C_D value of 0.127, and based on the flow analysis done in this section can be considered as outstanding. With the drag coefficient obtained and with no major detrimental flow features, it could be classify into a exceptionally aerodynamically car. The aerodynamic behaviour of this design can only be comparable with some other ultra efficient cars seen as prototypes, record breaking challenges or other vehicles inside the Shell Eco Marathon. The C_D situate this car its value below any of the commercial cars available of the market. This design can be consider as a suitable one for the achievement of a ultra efficient car.

8.2 Study 1: Reducing frontal area

Although the new design have resulted satisfactory, the frontal area of this new design is bigger than the actual car of the Team Aalborg Energy. As the total drag is proportional to $C_D \cdot A$, a modification of this design with a lower frontal area is created, with the intention of reducing the total drag force. Figure 8.6 shows the schematic of the reduced frontal area modification. This new design, has a 4.50% smaller area, but conserving most of the geometrical features of the new design.

A numerical simulation is conducted in order to analyse the aerodynamic performance of the design with the reduced area. Different CFD simulations are done in order to ensure the validity and the mesh independence of the solution. The information regarding the mesh, model used and the solution of each of the simulations is presented in Table 8.4.

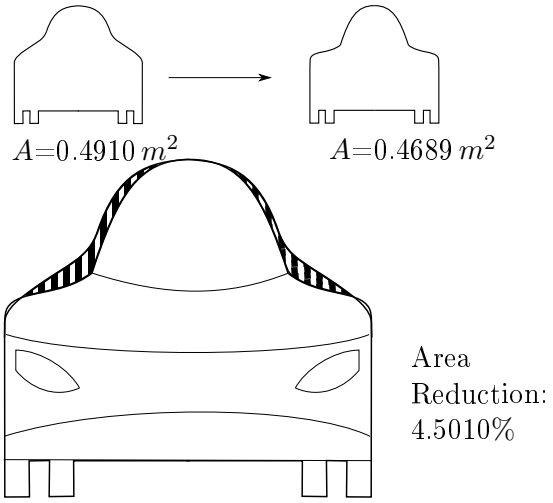

Figure 8.6: Reduction of the frontal area of the vehicle

	Mesh 1	Mesh 2	Mesh 3
Mesh Type	Tetrahedral	Tetrahedral	Tetrahedral
Nodes	$3.481\,10^6$	$4.421\,10^6$	$4.421\,10^6$
Elements	$17.625\,10^6$	$22.431\,10^6$	$22.431\,10^6$
Face Sizing	8 mm	7 mm	7 mm
Body Sizing	40 mm	35 mm	35 mm
Growth Rate	1.03	1.03	1.03
Mesh Conversion	Polyhedral	Polyhedral	Polyhedral
Elements Polyhedral	$3.517\,10^6$	$4.462\,10^6$	$4.462\,10^6$
Ratio Elements	5.011	5.027	5.027
Model	Real. κ–ϵ	Real. κ–ϵ	RSM
Drag Coefficient	0.13214	0.13231	0.13582
Lift Coefficient	0.13051	0.13126	0.15227

Table 8.4: Number of cells.

From this, after performing several simulations with different mesh sizes, the solution of the second mesh have been proved to be mesh independent, as it differs less than 0.15% in the results. A value of 0.132 for the drag coefficient is obtained from this simulation. The solution considered have also been checked to be converged as shown in Figure 8.7. Also, the RSM model have been used to check the differences between the Realizable κ–ϵ and this other model. The differences found between the models differ less than 3% for the drag.

The C_D value found is slightly higher than the value of the non-reduced area design. Despite of this, and in order to know if there is a real reduction in the drag over the vehicle, the total force or the $C_D \cdot A$ must be compared. In Table 8.5, the different components of the drag force over the vehicle are presented.

Pressure Force	1.1776 N
Viscous Force	0.7340 N
Total Force	1.9116 N

Table 8.5: Drag forces at 7 m/s.

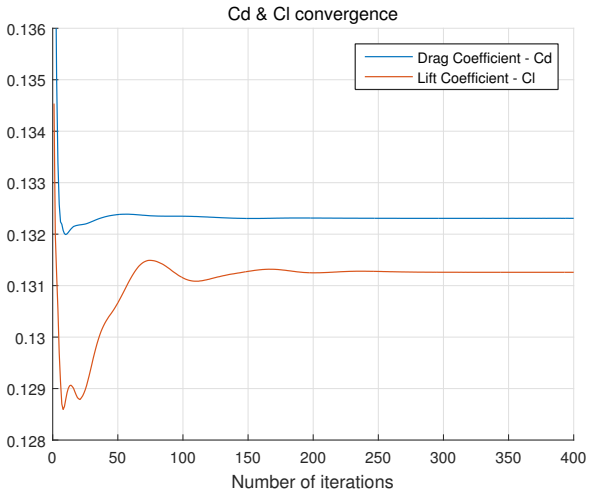

Figure 8.7: Convergence of the Mesh 2.

Comparing the values of this table with the ones from Table 8.3, it can be concluded that the reduction of the frontal area of the vehicle increases the drag by 1.99%. The total force is now 1.911 N compared with the 1.874 N of the first design. Although the viscous drag is diminished, the pressure drag is increased. The lower amount of surface area may explain why the viscous drag is lower in this reduced area design. The increase of the pressure drag may be related with the greater steepness on the sides of the vehicle, that may create regions prone to the flow separation. The C_D value of this vehicle is 0.132 compared with the 0.127 of the previous design.

This attempt of reducing the drag by decreasing the frontal area have resulted unsatisfactory. It should be noted that the possibility of obtaining a design with lower drag with less frontal area is not discarded, as some design may fulfil both conditions.

8.3 Study 2: Cut-Off Rear End

As seen from Figure 8.1 the tail of the new design is based on the so-call tear drop shape. This is one of the most optimal shapes for a road vehicle aerodynamics. This rear back configuration is not seen in any commercial cars and its design, based on the personal opinion of the author, is far from be aesthetic. Also, it needs a large elongation of the length of the vehicle associated with a considerable increase on the weight. Thus, for the sake of the curiosity and for possible improvements on the design, a study about how much the cut-off of the rear end influences the drag will be conducted.

Using the first new design, segments of different lengths will be chopped from the rear back of the vehicle. Numerical simulations will be carry out for each of these cases to see how much the drag is increased. The top of Figure 8.8 shows a schematic of the cuts that will be done each 125 mm. The author expects that close to the trailing edge the momentum available in the boundary layer will be small. Therefore a chop after that point is not expected to influence greatly in the pressure drag or the flow separation, as no energetic flow remains after that region. After carrying out the simulations, Figure 8.8

shows the drag increase for each of these cases.

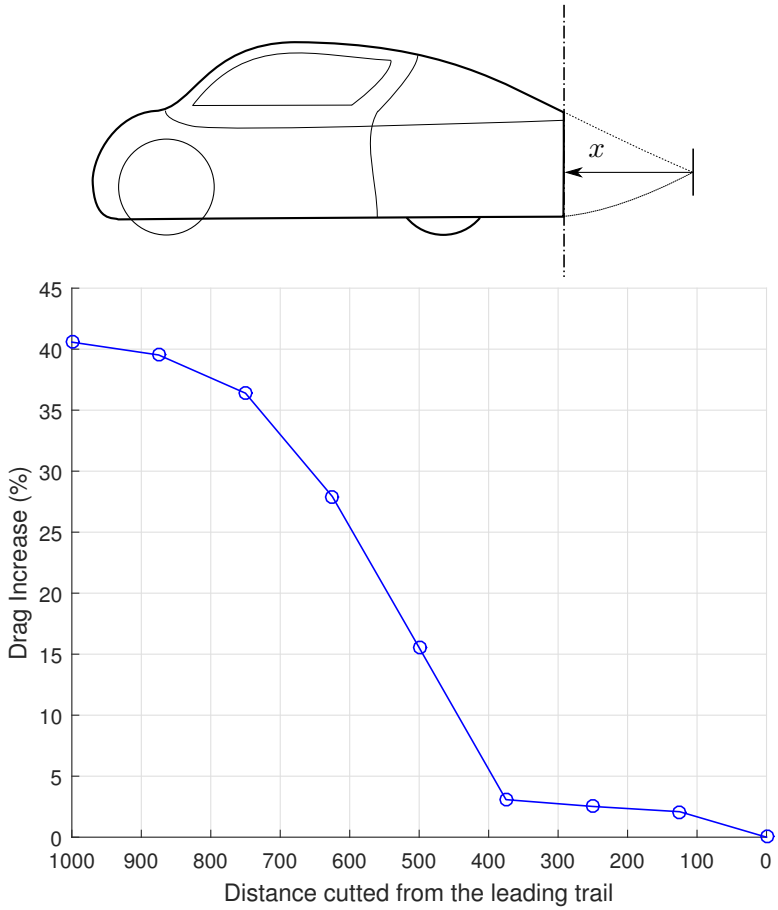

Figure 8.8: Kammback effect.

From this figure it is seen that bigger the cut, the larger the drag, as it would be expected. The relevant outcome from this study is that cuts up to around 400 mm do not have a significant increase on the drag, increasing it only up to 4%. From there on, bigger cuts have a considerable and fast increase in the drag. Furthermore, with chopped distances larger than 1 meter, the drag increase becomes steadier. Despite the small changes in the drag once reached this region, the total drag increases nearby 40%, giving a poor aerodynamic performance. The result obtained in this study follows a 'S-shape´ behaviour similar to the one shown in Figure A.8.

The results obtained in this study can be used for the design and improvement of the car. The reduction of rear end of the car while the drag is not significantly increased could reduced the weight and also improve the aesthetics of the vehicle. Although the drag over the vehicle is almost 4% higher with a chop of 400 mm, fewer material would be needed. The reduction on the weight in the vehicle would reduce the power associated with the extra load carried. This reduction could compensate the increased drag, and come to a more energy efficient design. Investigation should be done in order to check whether this weight reduction could counterbalance the drag increment .

8.4 New Design 2 based on previous Studies

The results from the new design, with a C_D value of 0.127 were really satisfactory. Despite this, a new design will be created as an attempt of further reduce the drag. This new design will be based on the experimental studies from the automotive industry explained in Appendix A and the results obtained from the Section 8.3. Most of the design will be based on the optimum angles arisen from the experimental work compiled in the book of 'Aerodynamic of Road Vehicles' [11]. Based on those angles that have been discussed in Section A, a new car have been proposed. A sketch of this new design is shown in Figure 8.9.

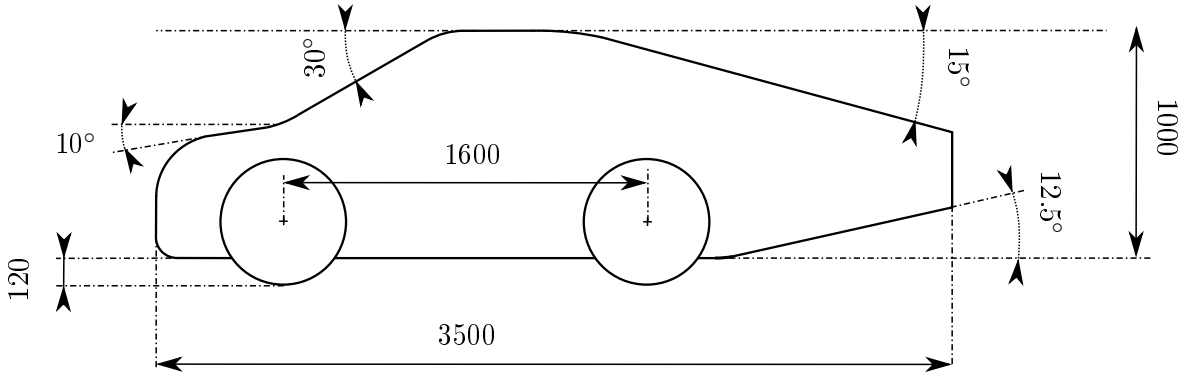

Figure 8.9: Drawing of the design. Distances in millimetres [mm] and angles in degrees [°].

The angles used in different section of the car seen from Figure 8.9 are explained here:

- For the hood, an angle of 10° is used, based on the studies shown in Figure A.3.
- For the windshield, an angle of 30° is chosen. Although smaller angles would reduce further the drag (Figure A.3), it could create some visibility and spacing problems [11].
- For the rear back, an angle of 15° is selected. This angle is the most crucial parameter in the design of the car, as it will determine the flow features in the wake and the location of the flow separation. Based on different previous studies [11], the optimum slant angle have been found to be 15° as shown in Figure A.5.
- For the underbody diffuser, an angle of 12.5° is picked. The angle chosen is based on Figure A.7, and in addition to reduce the drag, is also expected to generate down force in the vehicle, improving its stability.
- For the possible edges in the vehicle, a smooth tangency is used to connect the different regions of the car.

A numerical simulation is conducted in order to analyse the aerodynamic performance of this new design. The same approach for the meshing and the numerical set-up as the other car is adopted for this analysis. After doing a couple of simulations to ensure the mesh independence of the solution, and after checking its convergence the results regarding the drag and lift coefficient are shown Table 8.6.

	New Design 2	New Design 1	Change (%)
C_D	0.1311	0.1272	3.066
C_L	-0.1333	0.1331	-200.150

Table 8.6: Drag and lift coefficient of new design.

From this table, it can be seen that the drag coefficient is increased by 3%. Surprisingly, the design based on previous studies have a slightly larger drag coefficient than the first new design. The total drag force, both the pressure and the viscous one is presented in Table 8.7. Regarding the lift, the design proposed have an extraordinarily change in the lift coefficient. The car instead of producing a a positive lift, produces down force, pushing the car towards the road. This down force is most likely generated as a result of the diffuser designed in the rear back of the vehicle, and may be beneficial for the car stability and grip in the turns, but increasing the apparent weight of the vehicle.

Pressure Force	2.3477118 N
Viscous Force	1.64743138 N
Total Force	3.9951432 N

Table 8.7: Drag forces at 7 m/s.

From Table 8.7, and comparing with Table 8.3, the total force over the vehicle is 6.577% higher. Both the pressure and viscous drag is bigger in this re-design. This design, although based on previous experimental studies within the automotive industry, it has not resulted in a drag reduction. The only benefit for this design it could be considerable down force generated for the vehicle.

Chapter 9

Estimation of the Fuel Efficiency

This chapter describes the expected increased on the fuel efficiency and power reduction of the improvement and new design. It is important to acknowledge that the results of this chapter are based on approximated and estimated data of the power consumed in 2015 of the current car used in the Shell Eco Marathon competition. In that year 2015, the car for Team Aalborg Energy obtained the 3^{rd} position achieving a fuel efficiency of 204.2 km/m^3 of H_2 at standard pressure, or the equivalent in gasoline of 620 km/L. Table 9.1 shows the fuel efficiency obtained by the winners of last year in a hydrogen powered vehicle inside the UrbanConcept category.

Rank	University	Result [km/m^3 of H_2]	Result [km/L] *
1	Polytech Nantes	372.6	1131.3
2	Technical University Of Sofia	215.4	654
3	Aalborg University	204.2	620

* Gasoline Equivalent

Table 9.1: Results Shell Eco Marathon 2015, UrbanConcept powered by hydrogen [27].

The highest fuel efficiency in the competition have been achieved by the "La joliverie Polytech Nantes" with a result of 372.6 km/m^3 of H_2. The car for the Team Aalborg Energy was 45% less efficient that this car.

The current car of the AAU uses approximately 200 W of power for the motors during cruise speed. This energy is used and lost in the drive train of the vehicle, the motor, the transmission, motor controller, the aerodynamics, etc. From this study the C_D value of the car was calculated, allowing us to estimate the amount of energy lost due to the movement of the car thought the air. Equation 9.1 states the amount of power needed to overcome the drag produced.

$$P = U\,F_D = \frac{1}{2}\rho U^3\,A\,C_d \tag{9.1}$$

Considering that the average speed of the car is 7 m/s (ie. around 25 km/h), that the frontal area of the current vehicle is 0.8440 m^2, that the drag coefficient is the 0.614 calculated and that the fluid is air at 25^{o}C (ie. ρ=1.225 kg/m^3), the power can be calculated through Equation 9.1.

Therefore, the amount of power used in the current design to overcome the drag is 108.87 W at 7 m/s. That means that 54% of the power is used exclusively to move the car through the air. Reducing the drag results in a increase of the efficiency, as less power would be needed for the operation of the motors at the same speed and conditions. In the next sections, the power reduction and fuel efficiency for the 2016 competition and for future years are analysed.

9.1 Estimation for Shell Eco Marathon 2016

For the competition in June 2016, there is no enough time for the implementation and construction of any of the new design proposed. For this reason, only the add-on modifications of Chapter 7 may be implemented. This section aims to study to reduction of the power of each of those modifications and the increased on the fuel efficiency compared with the current design.

Based on the C_D values obtained in Chapter 7, the power needed to overcome the drag of each of one these designs may be calculated, as shown in Figure 9.1. The velocity is shown in the x-axis to see the influence of the speed on the power consumption. A vertical line marks the averaged speed of 7 m/s.

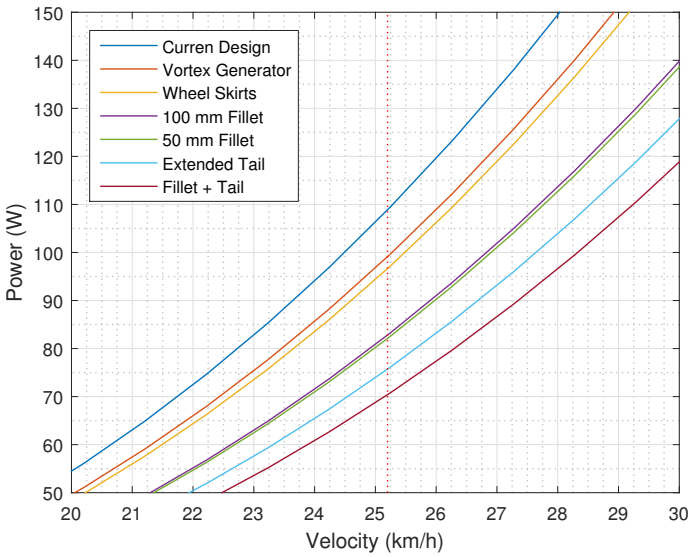

Figure 9.1: Power needed by the current with the different add-ons. The red dashed vertical line marks the averaged current speed of 7 m/s.

It can be seen that the improvements can obtain great power reductions. From the 108.9 W used on the current design to only 70.4 W for the car with the fillet and the extended tail. This best improvement would save 38.5 of the 200 W total used on the car. That means a 19 % reduction on the power consumption of the car.

It is also important to notice the big influence of the velocity on the power needed to overcome the drag. For this reason the average speed of the car should be reduced to the minimum possible. If the averaged speed is diminished from 25 km/h to for example

23 km/h, 26.5 W would be saved for the current design. For the best improvement, the reduction of the velocity would be 17.1 W.

An estimate of the fuel efficiency can be calculated based on the result of the car on the competition, the total power currently used and the power saved by the modifications.

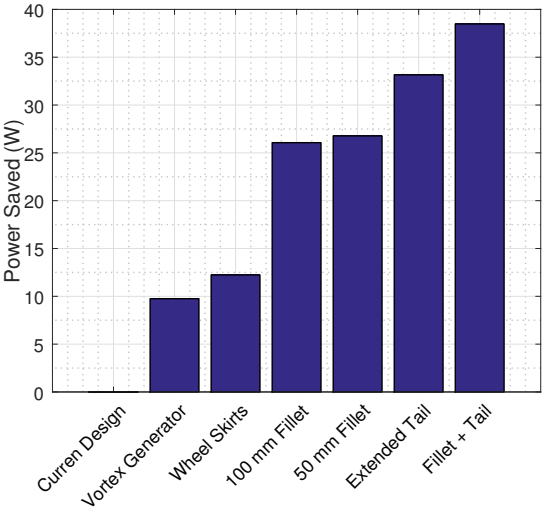

(a) Power saved with the different add-ons.

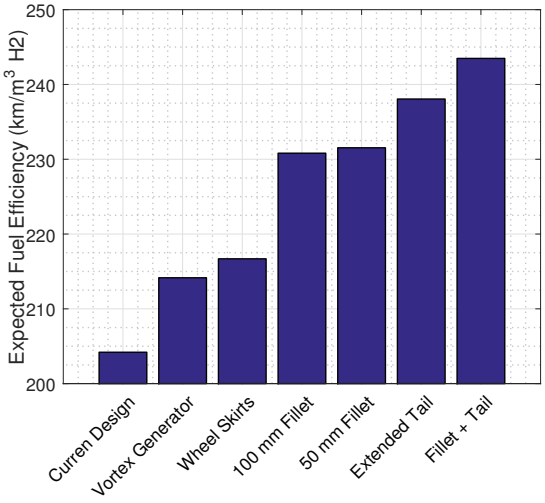

(b) Fuel efficiency with the different add-ons.

The expected fuel efficiency of the car would be increased from 204.2 to 243.5 km/m^3 of H_2 with the best of the modifications. If measured in km/L of gasoline equivalent, the current design will improve its fuel efficiency from 620 to 739.28 km/L. That is an increase of 20% the fuel efficiency of the car. Based on the results from the 2015 (Table 9.1), this would place the car of Aalborg University in the 2^{nd} place of the competition, surpassing the 215.4 km/m^3 of H_2 of fuel efficiency of the Technical University of Sofia.

9.2 Estimation for future Shell Eco Marathons

For the future Shell Eco Marathons, more time is available for the construction of a new design for the outer shell of the car. Based on the best design obtained, with a C_D value of 0.127, approximate estimations of the increased in the fuel efficiency will be conducted. First of all Figure 9.3a presents the drag reduction of this new design compared with the current car. Figure 9.3b compares the power consumed by the aerodynamics of the different designs.

From the Figure 9.3a, it can be seen the great force reduction of the new design compared with the current one of the team. The streamlining of the new design have reduced greatly the pressure drag by increasing only slightly the viscous drag. At the speed of 7 m/s the force is reduced from 15.5 N to only 3.7 N. That is an significant reduction of the 76% of the drag.

From Figure 9.3b it can be seen the power required by the current car, the modified one and the new design. From this, the power required for the new design is only 26.2 W compared with the 108.8 W of the current car, reducing it by 75.9 %. This means saving 82.6 W of the total 200 W of power used into the motors. Regarding the differences

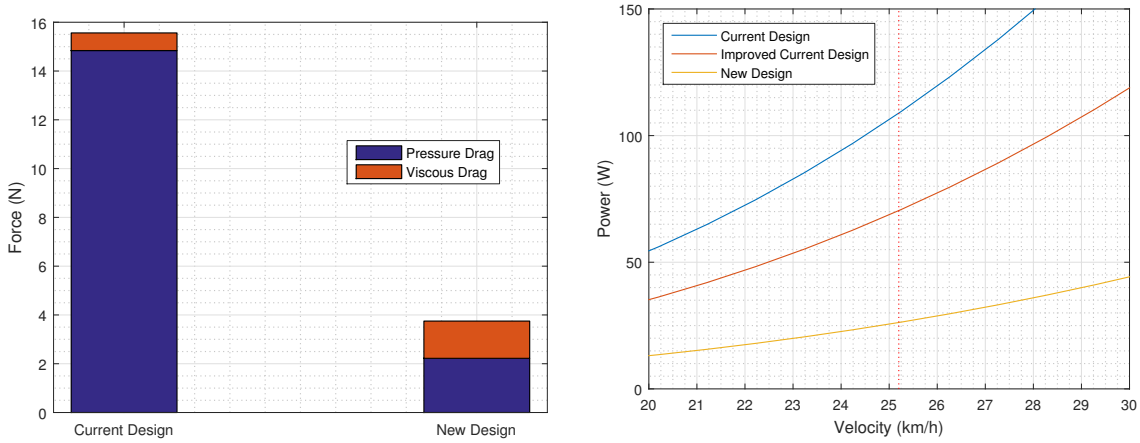

(a) Drag components comparison.

(b) Power required comparison.

between this new design and the improved current car, the new design reduces another 62.78 % the power needed for the drag. From the Figure 9.3b it can also be seen the importance on the velocity on the power consumption. The vertical red line of the figure shows the reference line for the speed of 7 m/s. Reducing the speed of the car brings great reductions on the power and shortening the differences between the designs. The higher the speeds the larger the differences in power consumption between the designs. This emphasizes the vital importance on a good aerodynamic design at high velocities in order to obtain good fuel efficiencies. In Figure 9.4 the expected fuel efficiency in km/m^3 of H_2 of the different designs is shown.

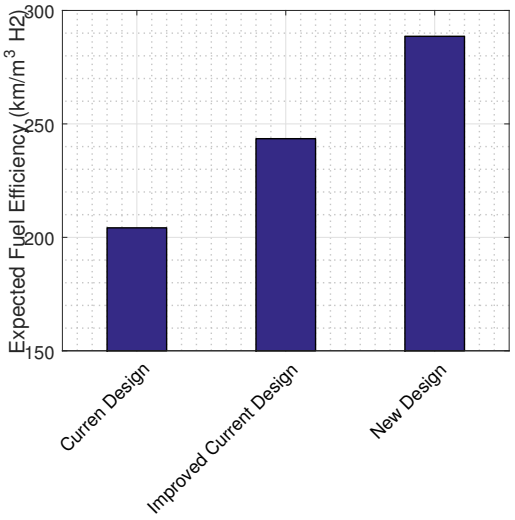

Figure 9.4: Expected fuel efficiency comparison.

It can be seen that the fuel efficiency of the car is increased from the 204.2 to 288.6 km/m^3. This indicates an significant increase of 41 % of the efficiency. Despite the low speed of the car, the aerodynamics plays a vital role on increasing the fuel efficiency of vehicle, as shown in Figure 9.4. If measured in km/L of gasoline equivalent, the current car will improved its fuel efficiency from 620 to 876 km/L with just the construction of the new outer shell proposed.

Chapter 10

Conclusion

This work have investigated the aerodynamic performance of the current car of the Team Aalborg Energy competing in the Shell Eco Marathon competition. Numerical and experimental testing of the car was conducted to calculate the drag and lift. Also with the aim to reveal its flow features and aerodynamic deficiencies.

A CFD simulation in ANSYS Fluent was performed to simulate the flow around the vehicle at the speed of 7 m/s. A mesh of 18 million elements with the Realizable κ–ϵ model arose a drag coefficient C_D of 0.614. This value, that gives an indication of the aerodynamic performance of the car, exposed the poor quality of the current design. The vector fields of the car were analysed, revealing its flow features. From this, the baseline shape, the wheels, the sharp edges, the steep rear back and the wheels cases have found to be enormous sources of drag within the vehicle, contributing negatively towards its efficiency. Furthermore, in order to validate and verify the CFD solutions, experimental analysis of the car were conducted in the wind tunnel of Aalborg University. Using a 1:9 scaled model, the forces over the vehicle were measured. This resulted in a corrected C_D value of 0.752, slightly bigger than the one of the numerical simulation, but emphasizing the bad aerodynamic performance of the current design. Also, a PIV system was used to visualize the flow in the wake in order to evaluate how the CFD was able to predict the flow separation seen in the rear back of the vehicle. Besides, smoke was injected in the wind tunnel during the testing allowing to recognize the flow features detected from the CFD analysis. From the experimental investigation, it was also concluded the validity of numerical model, as it was able to predict correctly the flow features and velocity fields seen in the wind tunnel. Both the numerical and experimental analysis showed the low aerodynamic efficiency of the car and the necessity of the reduction of the drag coefficient.

In the pursuit of fast and cheap drag reductions methods, different add-on modifications were proposed and analysed. These complement included wheel skirts, extended tails, rounding of edges and vortex generators. All these modification in the design were evaluated in CFD, following the same numerical set-up as with the current design. They yielded satisfactory individual drag reductions of 8 to 35 %. These modification are aimed to be applied to the actual car for the Shell Eco Marathon of June in London, as no time is available for the manufacturing of a brand new design. The better of these modification

is expected to increased 20% the fuel efficiency of the current car.

With the perspective of the upcoming competitions, and as the current design with the modifications is not yet satisfactory, a completely new design have been proposed. This car have been designed based on the deficiencies of the current car and the fundamental knowledge of fluid dynamics. CFD simulations were carried out in this design, resulting in an outstanding C_D value of 0.127. This design achieves an extraordinary 80% reduction of the drag with respect to the current design. Posterior to the creation of this new design, two studies of the influence of the change in the frontal area and the cut-off of the tail of this design were performed. Contrary to what it was initially expected, the reduction of the frontal area of this vehicle didn't result in a reduction of the total drag. Regarding the cut-off of the tail, 9 numerical simulations with cuts at different lengths was performed to see its influence. From this study, it was concluded that cuts up to 400 mm only contribute slightly to an increase of drag, with a maximum of 4%. After this point, the contribution increases rapidly, reaching up to 40% of a drag increased in just another 400 mm of extra cut. Based on these studies and past research on the automotive industry, a new re-design was proposed. This new design was analysed in the CFD software, giving a C_D value of 0.1311. This new design have an increased drag coefficient of 3%. Despite of the drag increase, this design creates a considerable amount of down force, contrary to all the previous designs. This down force may be beneficial to improve the stability of the car at hight velocities, but increases the apparent weight of the vehicle.

With the use of any of these two new designs, a great reduction on the drag of the vehicle will be achieved. Its construction will increase remarkably the overall efficiency of the car. The total power needed in the car at the driving speed of 7 m/s would be reduced by 82.8 W of the total of approximately the 200 W currently used. The fuel efficiency would be expected to be increased by 40%.

Chapter 11

Future Work

Although the results presented have resulted really satisfactory, many different modifications, simulations, experiments and improvements have been left for the future due to the lack of time. The study and improvement of the aerodynamics of a certain vehicle is complex task, where the perfect design does not exists, so the future work proposed could have no limit. In this chapter some relevant suggestion for future work are going to be discussed. The goal of this recommendations is to obtain better accuracy of the results, improve further the aerodynamic performance of the designs and to reach high quality aerodynamic analysis.

Reduction of the noise in the measurements on the wind tunnel

The experimental analysis of the forces done in the wind tunnel have shown considerable variations. In order to reduce the noise in the measurements of the sting balance, a thorough calibration of the system and the creation of a data filtering would be recommended.

Further use of the PIV system

The PIV visualization have been only conducted for the symmetry plane, in the area of the wake of car. For capturing the velocity flow field of different regions of the car, the PIV system would need to be moved and recalibrated. If this is done, much more information will be obtained of the flow field, and would help to verify and validate the different flow features in various regions obtained in the CFD simulations.

Simulate turning wheels and moving ground

In both the experimental and numerical analysis, the ground and wheels were stationary. In a real case scenario, the ground would be moving with respect to the car and the wheels will be rotating. These both conditions should be simulated if realistic results wants to be obtained. For the wind tunnel testing, a scaled model with turning wheels would need to be created. Besides, in the wind tunnel, a new set-up with a moving belt should be installed in order to simulate the moving ground. For the numerical analysis, these requisites can be

implemented easily in the boundary conditions of the set-up of the problem. A simulation or an experiment with this conditions would be expected to arise a solution closer to the real driving case scenario.

On-road testing of the car

Along this thesis, both numerical and experimental simulations have been performed to evaluate the aerodynamic performance of the vehicle. It is recommended as a future work to perform analysis on the real car. Different instrumentation as pitot tubes and pressure taps can be placed in different parts of the car to acquire data while driving. Also, smoke and tuft flow visualization can be used to observe the flow features and the separation regions. There is also techniques available to calculate the drag over the vehicle in a track. The availability of the car is a great opportunity to perform this kind of testing posteriori to the creation of the car.

Improvements of the modifications proposed by the current design

Different modifications for the current design have been proposed and analysed, including wheel skirts, rear extensions, fillets and vortex generators. These modifications have not been designed appropriately, and although they have been proved to reduced considerably the drag, much higher drag reductions will be expected. Farther studies and analysis of each of these components, specially the vortex generator and the rear extension, could be done to obtain the maximum drag reduction of these add-ons.

Optimisation: use of the ANSYS Fluent Adjoint Solver

Analytical optimisation of a geometry in CFD is a extremely complex task and out of the scope of a Master thesis. Thankfully, the latest versions of ANSYS Fluent have introduced a built-in tool for the optimisation of a geometry in CFD, the Adjoint Solver. It would be recommended as a future work to attempt to use this tool in the pursuing of the optimal design in terms of the drag. Although this tool is expected to be really challenging to use (specially in terms of computational resources, computational time and learning curve), it would convert the currently trial and error process into an automated one.

Analysis of weight vs. drag reduction

Some of the analysis designed in this thesis have achieved small drag reductions by incrementing the total surface of the car. As it was explained, this larger amount of surface will carry an increased of the weight of the vehicle. In order to be account for the overall efficiency of the car, a study of the balance between added weight and drag reduction should be done.

Creation of more designs

Two new cars have been designed and tested. Although they have reached a satisfactory drag coefficient, more designs could be proposed and analysed. Based on the analysis of

previous designs and a trial and error approach, further improvement of the aerodynamic performance will be expected.

Experimental testing of all the designs

Only the current design have been tested in the wind tunnel. In order to validate all the other designs tested only in CFD, it would be recommended to perform also experimental analysis in the wind tunnel.

Bibliography

[1] *R Adelnia.* R Adelnia. Evaluation of Surface Finish Effect on Aerodynamic Coefficients of Wind Tunnel Testing Models.

[2] **Alessandro Talamelli and Johan Westin**. Alessandro Talamelli and Johan Westin. *Aerodynamics of cars drag reduction.*

[3] **ANSYS, 2016**. Inc. ANSYS. *ANSYS Fluent Theory Guide, Release 17.0.* Prentice Hall, 2016.

[4] **ANSYS, 2016**. Inc. ANSYS. *ANSYS Fluent Meshing User's Guide, Release 17.0.* Prentice Hall, 2016.

[5] **Çengel, 2010**. Y.A. Çengel. *Fluid Mechanics.* Çengel series in engineering thermal-fluid sciences. Tata McGraw Hill Education Private, 2010. ISBN 9780070700345.

[6] **Cobb, 2016**. Jeff Cobb. *Top Six Plug-in Vehicle Adopting Countries, 2015*, 2016. URL `http://www.hybridcars.com/top-six-plug-in-vehicle-adopting-countries-2015/`.

[7] **Das**. Prasanjit Das. *The Blockage Effects on Vehicle Aerodynamics in Closed-Wall Wind Tunnel–A CFD Study.*

[8] **Davis, Rinehimer, and Uddin**. PL Davis, AT Rinehimer, and M Uddin. *A comparison of RANS-based turbulence modeling for flow over a wall-mounted square cylinder.*

[9] Henrik Aaserud Eikeland. Aerodynamic Development and Construction of a Car for Participation in the Eco-Marathon Competition. Master's thesis, Norwegian University of Science and Technology, 2010.

[10] **Transport (DFT)**. *Department for Transport (DFT).*

[11] **Hucho and Sovran, 1993**. Wolf-heinich Hucho and Gino Sovran. *Aerodynamics of road vehicles*, volume 25. Annual Reviews 4139 El Camino Way, PO Box 10139, Palo Alto, CA 94303-0139, USA, 1993.

[12] **Hyvarinen, 2015**. Ann Hyvarinen. *Investigation of blockage correction methods for full-scale wind tunnel testing of trucks*, KTH, Royal Institute of Technology, 2015.

[13] **Hyvärinen, 2015**. Ann Hyvärinen. *Investigation of blockage correction methods forfull-scale wind tunnel testing of trucks*. 2015.

[14] **Lanfrit, 2005**. Marco Lanfrit. *Best practice guidelines for handling Automotive External Aerodynamics with FLUENT*, Fluent Deutschland GmbH, 2005.

[15] **Levin and Rigdal, 2011**. Johan Levin and Rikard Rigdal. *Aerodynamic analysis of drag reduction devices on the underbody for SAAB 9-3 by using CFD*, 2011.

[16] **Maskell, 1963**. EC Maskell. *A theory of the blockage effects on bluff bodies and stalled wings in a closed wind tunnel*, DTIC Document, 1963.

[17] **Md. Hasan Ali, Mohammad Mashud and Islam**. Abdullah Al Bari Md. Hasan Ali, Mohammad Mashud and Muhammad Misbah-Ul Islam. *Aerodynamic Drag Reduction of a Car by Vortex Generation.* nternational Journal of Mechanical Engineering, 2.

[18] **Merkle, Kubota, and Ko, 1974**. CL Merkle, T Kubota, and DRS Ko. *An analytical study of the effects of surface roughness on boundary-layer transition*, DTIC Document, 1974.

[19] **Nykvist and Nilsson, 2015**. Björn Nykvist and Måns Nilsson. *Rapidly falling costs of battery packs for electric vehicles.* Nature Climate Change, 5(4), 329–332, 2015.

[20] **Transportation Statistics (BTS), 2008**. Bureau of Transportation Statistics (BTS). *National Transportation Statistics*, 2008.

[21] **Peric and Ferguson**. Milovan Peric and Stephen Ferguson. *The advantage of polyhedral meshes.*

[22] **Raffel, Willert, Kompenhans, et al., 2013**. Markus Raffel, Christian E Willert, Jürgen Kompenhans, et al. *Particle image velocimetry: a practical guide.* Springer, 2013.

[23] Ian J Ross. Wind tunnel blockage corrections: an application to vertical-axis wind turbines. PhD thesis, University of Dayton, 2010.

[24] Deepak Sahini. Wind tunnel blockage corrections: a computational study. PhD thesis, Texas Tech University, 2004.

[25] **Saxena, 2015**. Dr. Mukesh Saxena. *Vehicle Body Engineering Aerodynamics*, 2015. URL `http://docslide.us/documents/vehicle-body-engineering-558456f9b48a6.html`.

[26] **Seibert, Lanfrit, Hupertz, and Krüger, 2002**. Werner Seibert, Marco Lanfrit, Burkhard Hupertz, and Lothar Krüger. *A Best-Practice for High Resolution Aerodynamic Simulation around a Production Car Shape*, 2002.

[27] **Shell**, **2016**. Shell. *2016 Official Rules, Shell Eco-Marathon*. 2016.

[28] **Smith**, **2002**. J.H. Smith. *An Introduction to Modern Vehicle Design*. ISBN: 07506 5044 3. Butterworth-Heinemann, 2002.

[29] **Versteeg and Malalasekera**, **2007**. H. K. Versteeg and W. Malalasekera. *An Introduction to Computational Fluid Dynamics,* 2^{nd} *Edition*. ISBN: 978-0-13-127498-3. Prentice Hall, 2007.

[30] **White**, **2011**. Frank M. White. *Viscous Fluid Flow,* 3^{rd} *Edition*. ISBN: 978-1259002120. Tata Mcgraw Hill, 2011.

[31] **WHO**, **2014**. WHO. *7 million premature deaths annually linked to air pollution*, 2014. URL `http://www.who.int/mediacentre/news/releases/2014/air-pollution/en/`.

[32] **Wilcox**, **1998**. David C. Wilcox. *Turbulence Modeling for CFD,* 2^{nd} *Edition*. ISBN: 978-0963605153. D C W Industries, 1998.

[33] **Yin**, **2015**. Chungen Yin. *Slides from Lecture Aerodynamics and Flow*. 2015.

Appendix A

Drag Reduction Methods

Creating a remarkable aerodynamic design is a highly challenging and laborious task. Unfortunately, no general theory is available in the pursuance of the reduction of the drag in a vehicle. Although individual flow behaviour can be explained by means of principles of fluid dynamics, a systematic description of the flow around a complex geometry is infeasible. The prediction of the drag relies on experimental and computational methods, and all designs and modifications requires its individual testing such that the aerodynamic performance can be determined. The drag reduction have become a essential topic of research in the automotive and aerospace industry. In this section, based on a compilation from different books, studies and experiments as [2], [17] and [11], some of the most common methods of reducing the drag explained. The understanding of the trends seen in different studies is vital if the design of car with good aerodynamic performance wants to be achieved in reasonable time. This way, some general tendencies can be recognized and can be used as a guideline for the design of a low drag vehicle.

- **Front end**. Sharp edges on the front end of the vehicle may create separated flow, with detrimental effects on the total drag as shown in Figure A.1. By 1930, Pawlowski

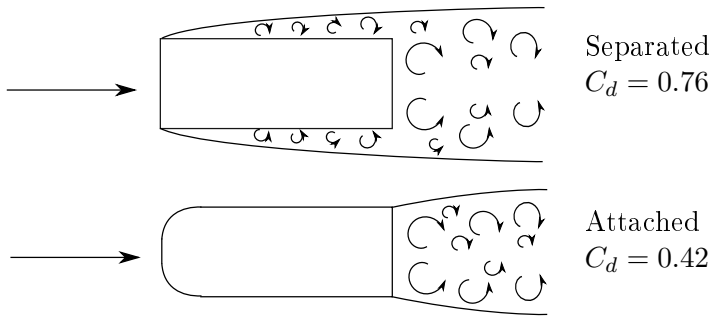

Figure A.1: Leading edge influence. Adapted from E. Möller.

had already published some data on the influence of the leading edge radius on the drag of rectangular bodies. He concluded that small radii are sufficient to achieve a minimum drag for box-shaped vehicles. Figure A.2 shows this effect in the studies performed by E. Moller in 1951 over the front design of the first Volkswagen LT van. From Figure A.2, the minimum drag is achieved from this van at a of 5% of the

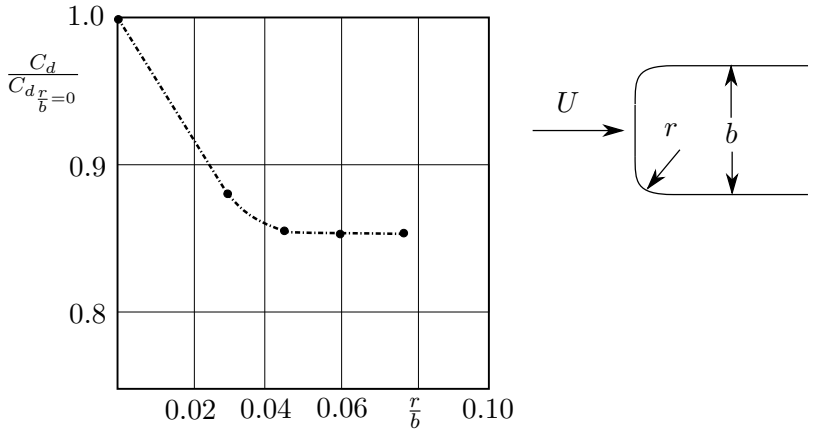

Figure A.2: Leading edge influence. Adapted from W. Hucho.

width of the vehicle, confirming that small radii are enough to obtain the minimum drag and prevent the flow separation of the front end.

- **Angle of hood and wind shield**. Increasing angle of wind shield with the vertical may reduce the drag. The effect of the drag reduction in the wind shield is directly influenced by the hood angle and the radius used in the front end. In Figure A.3, a study done by G.W.Caar regarding the drag reduction is shown.

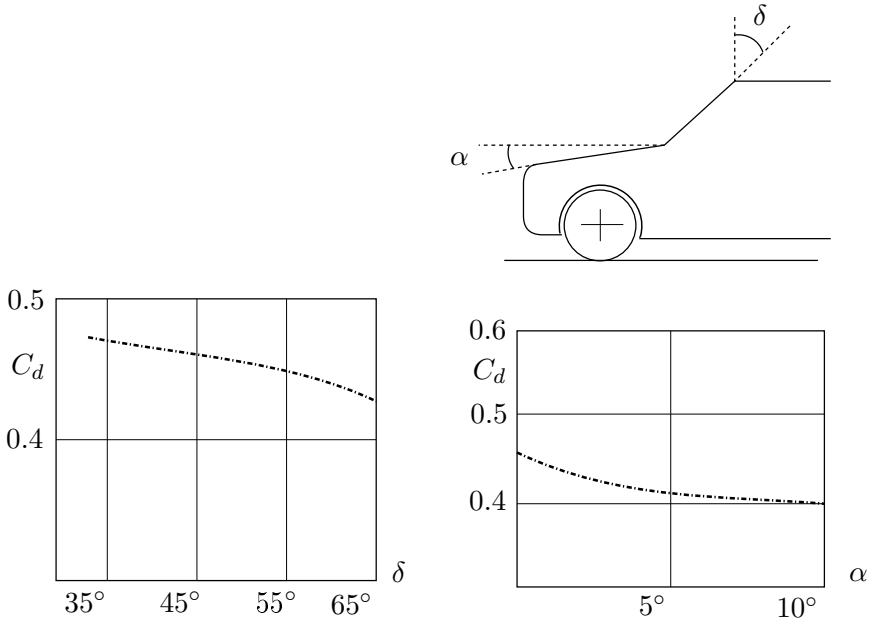

Figure A.3: Influence of the angles of the hood and wind shield in the drag. Adapted from G.W Caar.

From Figure A.3, it is seen that increasing the angle (δ) of the wind shield would reduced the drag coefficient. There are, however, some practical limitations for the maximum inclination, as angles bigger than 60° may originate visibility and temperature problems [11]. The angle of the hood also influences the drag reduction, decreasing the drag with increasing angles. From Figure A.3 it is seen than rising

the angle more than 10° will not have further effect on the drag reduction.

- **Roof and sides**. The drag in this areas is mainly due to friction drag. A negative angle of the roof may reduced the wake in the back of the car, but with the disadvantage of needing a bigger frontal area and reducing the internal space on the car. As the drag in this region is produced mainly because of the friction, ensuring smoothness and good quality surface is important [1].

- **Underbody flows**. The flow produced in the under body of a vehicle is quite complex and may affect considerably the drag and the lift. In order to reduce the drag it is recommended the use of rear panels and to avoid any kind of obstacle in the underbody that can create stagnation areas [15].

- **Rear end**. Two important areas can be considered in the drag reduction of the rear end, the upper and the lower rear end. For the first one, the methods are based on a reduction of the cross sectional area and by lowering of the roof. The design of rear end of the vehicle is the most crucial element design in order to accomplish a great drag reduction. The vehicle rear shape should approach to the ideal so-called tear drop shape (Figure A.4), so that the flow separation in the back is minimized. Usually, due to physical and practical restrictions the tear drop shape is not used in commercial vehicles, and another designs needs to be implemented whilst the drag contribution is not enlarged. In the automotive industry, the rear ends are usually categorized in three types, the square back, the fast back and the notch back as shown in Figure A.4. The kind of back influences greatly the characteristics of the flow on the wake of the car, and therefore the drag.

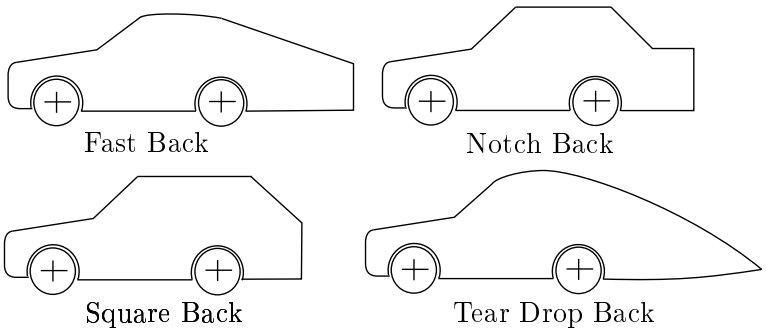

Figure A.4: Back Types

The influence of slant angle (β) on the drag coefficient is shown in Figure A.5 based on the experiments done by different authors.

From the Figure A.5, a really meaningful result can obtained. There is an situation where the drag is minimised, and this happen at a angle β of around 15°. Another interesting feature is that the character of the flow changes around a critical angle β of 30° where the drag reaches its maximum and a bi-stable separation occurs. For slant angles smaller than 30° the drag is reduced as the flow separation is retarded

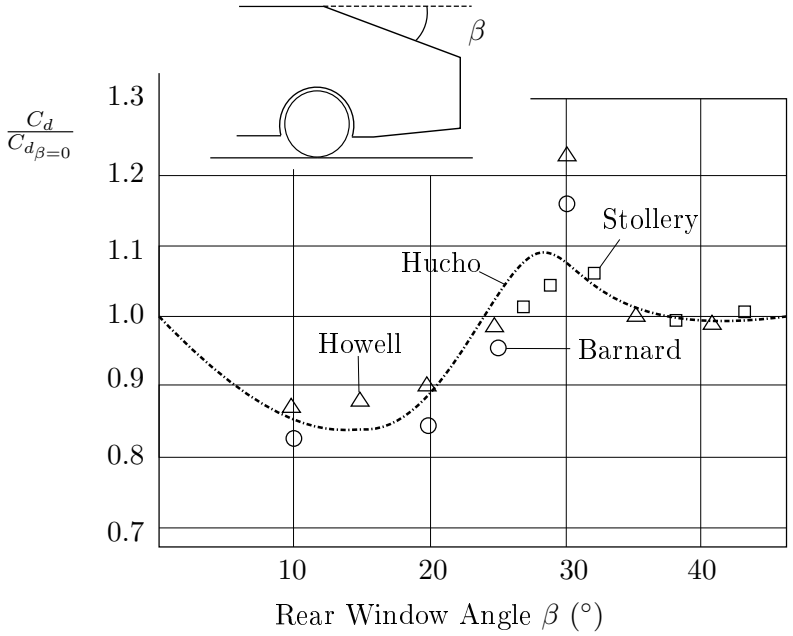

Figure A.5: Slant angle influence on the drag. Adapted from various authors.

up to the very end of the vehicle, as shown in Figure A.6. For slant angles bigger than 30°, the drag is reduced drastically with respect to the critical angle, but still bigger than angles smaller than 20°. The flow conditions are the one of a square back with the flow separated from the very top of the vehicle (flow not attached in the rear windscreen). The critical angle β of 30° is frequently used to classify the type of back of the vehicle, as it is associated with changes on the condition of the flow and the location of the flow separation. For angles bigger than 30°, the vehicle back is usually considered a square back while for angles smaller than 30° a fast back, as shown in Figure A.6.

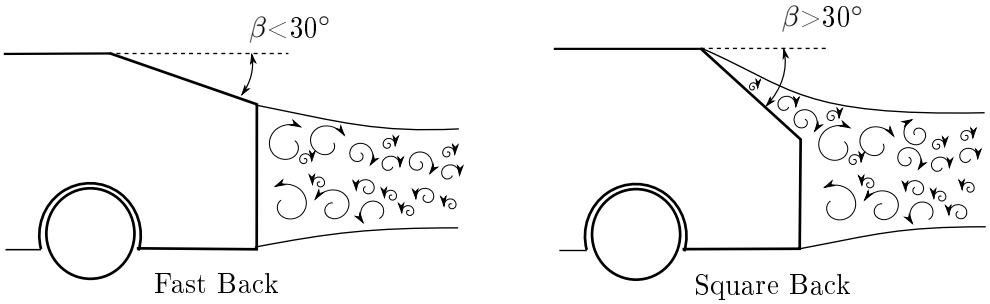

Figure A.6: Influence of the rear back on the wake structure.

The other important area of design in the back of the car is the underbody rear end, where a smooth transition and a diffuser should be used. Although diffusers are mainly used in high-speed vehicles to generate down force, it can also be used to reduced the drag. It is necessary to have a smooth underbody in order to obtain a effective drag reduction with a diffuser [15]. Figure A.7 shows the influence of a diffuser angle in the drag reduction.

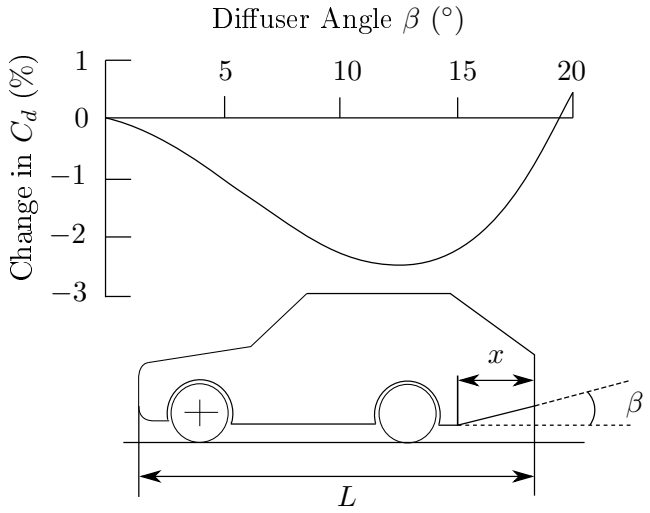

Figure A.7: Influence of a diffuser in the drag. Adapted from Happian.

From the Figure A.7, it can be seen that drag reduction is accomplished for moderate diffuser angles, with the maximum reduction between 10° and 15°.

Another important aspect on the design of the rear end, is the so-call boat tail shape, that may reduce the drag in the vehicle. The boat tailing shape consists in a gradual reduction of the end body cross-sectional area, specially of the side width. Figure A.8 shows the drag reduction as a result of the reduction of the width of the car. From Figure A.8 it is seen that the boat tail shape have positive effects on the drag

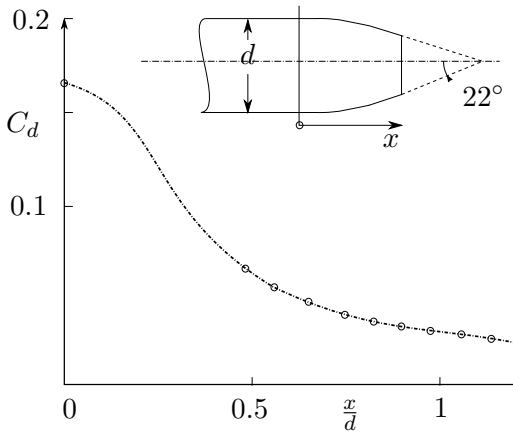

Figure A.8: Boat tailing influence on the drag. Adapted from W.A. Mair.

reduction over the vehicle. It should be noted that there is insignificant improvements by further extension of the body of $x/d > 5$ [11].

- **Wheelhouse**. The wheels can add up to 50 % of the drag of a well designed streamlined car [11]. For this reason a proper wheelhouse and wheel-arches may be decisive to reduce the drag losses. The smaller the gap between the wheel and wheelhouse, the better the aerodynamic performance of it, and both drag and lift may be reduced. The use of wheel skirts or fender skirts for covering the wheels may reduce further the drag significantly. Usually, only rear wheel skirts are used in the vehicle, as the

front wheels needs to turn in order to move the car and bigger skirts would be needed.

- **Spoiler**. The spoilers, both in the back or in the front of the car may reduced the drag in the vehicle. The spoilers need to be optimized in order to obtain satisfactory results over the overall drag reductions.

- **Vortex Generator**. Vortex generators (VGs) on cars can achieve improvements in car aerodynamics reducing both lift and drag. The VG creates a swirling flow that increases the energy in the boundary layer by taking momentum from the high energy flow available far from the free stream. With this, the momentum in the boundary layer is increased, delaying the separation of the flow and reducing the pressure drag.

Appendix B

Other Types of Drag

Based on 'An Introduction to Modern Vehicle Design' of J.H. Smith [28], the drag force in the vehicle design is usually broke down into six constituents. Apart from the pressure and viscous drag, already explained in Chapter 3, the others are:

- **Induced drag** For high-speed vehicles, and in order to allow the car to drive faster through a corner, a downward force perpendicular to the vehicle is created. This pushes the car tyres onto the road, increasing the grip and the traction. The redirection of the air in order to produce this down force, will have two components, one producing the desire negative lift, and the other, generating the induced, non-desired drag. This collateral drag is the so-called induced drag and contributes approximately 8% for a convectional road vehicle [25]. In Formula 1 vehicles, as enormous down force are produced, the contribution of the induced drag reaches values of 65%.
- **Excrescence drag**. This is produced due to components needed for the operation of the car, as wheels, wheel arches, wing mirror, door handles, rain gutter, windscreen wiper blades, etc. These components disturbs the smooth surface of the vehicle producing extra turbulence, local flow separations and drag.
- **Interference drag**. The interactions between the main flow and the flows around external devices (eg. wing mirrors) can increase further the drag. The contribution of the interference drag along with the excrescence are around 15% of the total drag produced by convectional car [25].
- **Internal drag**. This drag, that can add up to 10% of the total drag [25], arises from the losses in the front grill of the vehicle, that redirects the air to be used in the cooling of the engine, mechanical components and for the cabin ventilation flows. In many instances some flow is also redirect to the breaks, in order to prevent overheating, contributing in an extra manner to this internal drag.

Appendix C

Similarity and Model Testing

In order to calculate experimentally the aerodynamic forces acting on the vehicle, some testing of the flow of a fluid around the external body of the car should be conducted. One of the most extended methods in the automotive and aerospace industry is the use of a wind tunnel. In many cases, due to the lack of a wind tunnel big enough to perform a test of the full scale prototype and for economical and practical reasons, a model is used for the study. When this model, of different size than the full scale prototype, is placed and analysed in the wind tunnel, results regarding the full scale car can be extracted if certain conditions are satisfied.

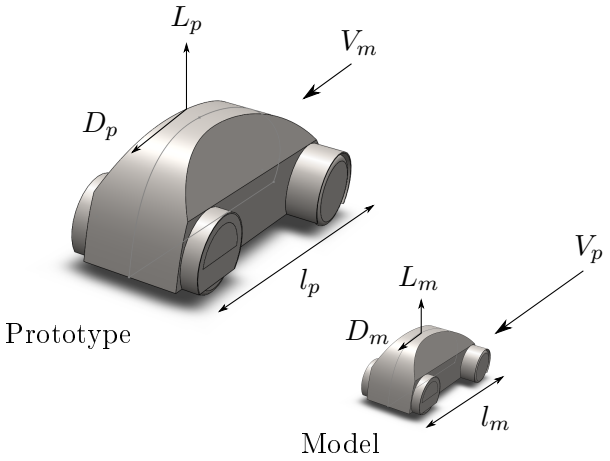

Figure C.1: Prototype and model

For the case that will be analysed, the car of the Team Aalborg Energy, a 3D printed model will be used. In order to perform the test of the model, the similarity laws must be applied in order to obtain satisfactory results. There are three necessary conditions that must be fulfil in order to archive the complete similarity between the model and the full scale prototype [5].

1. **Geometric similarity**: the model should have the same shape as the prototype, but it might be scaled to some factor.
2. **Kinematic Similarity**: the velocity at any point in the model flow must be proportional to the velocity at that point in the prototype flow.

3. **Dynamic similarity**: the forces acting on corresponding fluid particles and boundary surfaces of the prototype and model are proportional.

The dimensional analysis of the problem is the key to find the relationships between different physical quantities involved in the problem. This mathematical approach is one of the most used methods in experimental work. It provides the factors that affects the problem and it helps on the interpretation of the physical behaviour of it. For the practical purpose of this project, and as the experiments will be conducted in a scaled model in a wind tunnel, a dimensional analysis of the drag over a vehicle will be performed.

Based on the experience and observations, it is known that the drag for low speed flows is dependent on the following variables stated in Table C.1.

	Symbol	Dimensions
Drag	D	ML/T^2
Characteristic area	A	L^2
Viscosity	μ	M/LT
Density	ρ	M/L^3
Velocity	U	L/T

Table C.1: Drag dependent variables

where:			
	L	Lenght unit	[m]
	M	Mass unit	[kg]
	T	Time unit	[s]

Therefore, the drag over a body changes whether one or more of theses variables vary its value. It can be considered a function of all these parameters, as shown in Equation (C.1).

$$D = f(A, \mu, \rho, U) \tag{C.1}$$

In this problem, the five variables of Equation (C.1) and three fundamental dimensions (the length (L), the mass (M) and time (T)) are involved. Applying the Buckingham's π-theorem [5] and choosing density, velocity, and projected frontal area as the repeating variables, a formal relationship between dimensionless groups may obtained (C.2).

$$\frac{D}{\frac{1}{2}\,\rho\,A\,U^2} = f\left(\frac{\rho\,U\,\sqrt{A}}{\mu}\right) \tag{C.2}$$

On the left side of Equation (C.2), the drag coefficient explained in Section 3.1 appears. The term on the right side is the well known Reynolds dimensionless parameter, that represent the ratio of the inertial to the viscous forces (Eq. (C.3)), and fundamental in order to determine dynamic similitude between two different cases of fluid flow.

$$\mathrm{Re} = \frac{\rho \mathbf{v} L}{\mu} = \frac{\text{inertial forces}}{\text{viscous forces}} = \frac{\mathbf{v} L}{\nu} \tag{C.3}$$

The dimensionless drag, the drag coefficient C_d, is therefore a function unique of the Reynolds number (C.4).

$$\mathrm{C_d} = f(\mathrm{Re}) \tag{C.4}$$

It should be acknowledge that in high speed flows, usually at velocities higher than Ma= 0.3, the compressibility effects of the air should be taken into account, and more variables would be involved in the dimensionless analysis. The Mach number would show up in the results and the C_D would be dependent on the Reynolds and the Mach number.

The Equation C.4 it is applicable to both the prototype and the geometrically similar model. In order to obtain the similarity, it must be assumed that the Reynolds number of the model and prototype are the same (ie. $Re_m = Re_p$), such that the C_d of the model and prototype are the same.

$$\left(\frac{\rho V\sqrt{A}}{\mu}\right)_m = \left(\frac{\rho V\sqrt{A}}{\mu}\right)_p \tag{C.5}$$

where:	m	Subscript referring to the model	[–]
	p	Subscript referring to the Prototype	[–]

Taking into account that the Reynolds number must be the same, the velocity in the wind tunnel for a scaled model can be calculated with Equation (C.6).

$$V_\mathrm{m} = V_\mathrm{p} \times \left(\frac{\rho_p}{\rho_m}\right) \times \left(\frac{\sqrt{A}_p}{\sqrt{A}_m}\right) \times \left(\frac{\mu_m}{\mu_p}\right) \tag{C.6}$$

If it is further assumed that the air used in the wind tunnel has the same density and viscosity as the one in a real case situation, Equation (C.6) can be simplified into (C.7).

$$V_\mathrm{m} = V_\mathrm{p} \times \left(\frac{\sqrt{A}_p}{\sqrt{A}_m}\right) \tag{C.7}$$

The dimension of the model should be chosen in order to determine the ratio of $\sqrt{A}_p/\sqrt{A}_m$ for the calculation of the required velocity for the wind tunnel. There are different constraints for the maximum size of the scaled model, as the dimensions of the wind tunnel test section and the blockage ratio. The concept and the importance of the blockage ratio in experimental analysis in a wind tunnel is explained in Section C.1.

C.1 Blockage Ratio

The blockage ratio is defined as the ratio of the model's frontal area over the test section area of the wind tunnel as stated in Equation C.8

$$BR = \frac{A_p}{A_{ts}} \tag{C.8}$$

where:	A_p	Frontal area of the scaled model	[m^2]
	A_{ts}	Frontal area of the test section	[m^2]

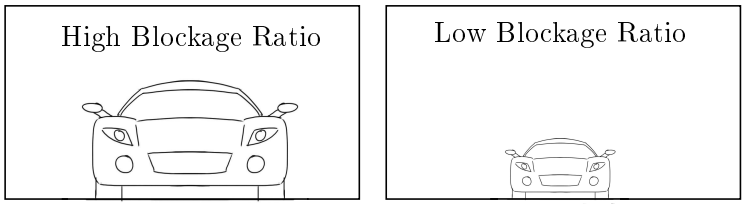

Figure C.2: Blockage ratio in wind tunnel.

If the frontal area of the prototype is relatively big compared with the frontal area of the test sections, the effects of the blockage ratio will create one of the main error sources in wind tunnel testing. [9] As the car blocks a certain area of the test section, the effective area where the fluid flows becomes smaller, and as in a Venturi tube, the constrained flow needs to accelerate around the car. This local flow acceleration also influence the boundary layer, increasing its thickness [13]. This behaviour can easily be explained with help of Bernoulli equation and mass conservation ($\rho AV = \text{constant}$) affecting the dynamic pressure and the velocity of the flow, that correspond to the drag increment seen in the experiments.

For a wind tunnel testing, low blockage ratio must be ensured, or in the other case, the values obtained in the experiment must be corrected. A lot of research has been done about wind tunnel correction over the years [24] and different methods have been proposed [23].

C.1.1 Maskell Correction

One of the first to address the problem of the blockage problems in a close wind tunnel testing was Maskell with the so-called Maskell correction [16]. The method can be derived using momentum balance in the flow outside the wake. This derivation gives a corrected formula for the dynamic pressure (q_c) in the wind tunnel, according to Equation (C.9) [7].

$$\frac{q_c}{q} = 1 + \frac{5}{2} C_D \frac{A_p}{A_{ts}} \tag{C.9}$$

where:			
	q_c	Corrected dynamic pressure	[Pa]
	q	Uncorrected dynamic pressure	[Pa]
	C_D	Uncorrected drag coefficient	[–]
	$\frac{A_P}{A_{ts}}$	Blockage ratio (BR)	[–]

Based on the corrected dynamic pressure, the corrected drag coefficient C_{D_c} can be obtained with the use of Equation (C.10).

$$C_{D_c} = \frac{C_D}{q_c/q} \tag{C.10}$$

The Maskell method is the one of the simplest methods created, and it has been proved to have some deficiencies for modern trucks and other long vehicles with a significant

amount of drag created by skin friction. Additionally the Maskell method does not take into account the solid blockage effects but only the ones caused due to flow separation [12].

Several improvements of the Maskell method have been proposed over the years for specific applications or to overcome some of its general deficiencies. Based on the experiments and investigation conducted by [7] for vehicle aerodynamics, the DNW-Maskell method and the method by Thom and Herriot appear to suit the best for automotive applications.

C.1.2 DNW-Maskell Correction

The DNW-Maskell correction for the dynamic pressure is presented in Equation (C.11). This improved version of Maskell's correction accounts for the vehicle length (l_m) meanwhile the corrected drag coefficient in terms of the dynamic pressure uses the original formulation Maskell correction of Equation (C.10).

$$\frac{q_c}{q} = 1 + \left(\frac{l_m}{8} + \frac{5}{2}\right) C_D \frac{A_p}{A_{ts}} \tag{C.11}$$

C.1.3 Thom and Herriot Correction

The other of the recommended corrections formulas for vehicles aerodynamics, is the one proposed by Thom and Herriot. The correction formula is given by Equation (C.12).

$$\frac{q_c}{q} = \left[1 + T\left(\frac{V_{car}}{{A_{ts}}^{3/2}}\right) + \frac{1}{4} C_D \frac{A_p}{A_{ts}}\right]^2 \tag{C.12}$$

where:			
	T	Thompson's tunnel shape factor	[–]
	V_{car}	Vehicle volume	[m^3]

The corrected drag is calculated using Equation (C.13)

$$C_{D_c} = \frac{C_D - T\left(\frac{V_{car}}{{A_{ts}}^{3/2}}\right) C_D}{q_c/q} \tag{C.13}$$

The Thompson's tunnel shape factor can be calculated with Equation (C.14).

$$T = 0.36\left(\frac{w_{ts}}{h_{ts}} + \frac{h_{ts}}{w_{ts}}\right) \tag{C.14}$$

where:			
	h_{ts}	Test section height	[m]
	w_{ts}	Test section width	[m]

With this corrections, the experimental values for the coefficient of drag C_d obtained of a relatively big model in a wind tunnel, can be corrected in order account for interference effects. For all the experimental work conducted in the wind tunnel of the university the three corrections, the Maskell's correction, the DNW-Maskell and the one of Thom and Herriot, will be applied to all the drag coefficient C_D values calculated. Then, a quantitative comparison of the different values obtained with the correction will be done, and one of them will be chosen when compared with the results obtained from the CFD simulations.

Appendix D

Turbulent Flow Modelling

The Navier Stokes Equations provides the governing laws that explains the physical behaviour of any viscous flow. This guarantees the existence of a mathematical model of the fluid mechanics and the basis for all the numerical methods used in the engineering field. For this reason, it is important to have a basic understanding of these equations in order to comprehend how the flow is modelled in a CFD commercial software.

The Navier Stokes Equations are composed by a set of Partial Differential Equations (PDEs). For a 3D velocity field $\vec{v} = (u(x,y,z), v(x,y,z), w(x,y,z))$ they can be written in a general case as the momentum of Equation (D.1). It should be noted that different notations and forms are used along the fluid mechanics bibliography, and special care should be taken when using other references.

$$\rho\frac{\partial(u_i)}{\partial t} + \frac{\partial(\rho u_i u_j)}{\partial x_j} = -\frac{\partial p}{\partial x_i} + \frac{\partial \tau_{ij}}{\partial x_j} + \rho g_i \tag{D.1}$$

Equation (D.1) can be rewritten into the 3 components of a 3D problem, the x, y and z direction. The x-component (Equation (D.2)):

$$\rho\frac{\partial(u)}{\partial t} + u\frac{\partial(\rho u)}{\partial x} + v\frac{\partial(\rho u)}{\partial y} + w\frac{\partial(\rho u)}{\partial z} = -\frac{\partial p}{\partial x} + \left[\frac{\partial \tau_{xx}}{\partial x} + \frac{\partial \tau_{yx}}{\partial y} + \frac{\partial \tau_{zx}}{\partial z}\right] + \rho g_x \tag{D.2}$$

The y-component (Equation (D.3)):

$$\rho\frac{\partial(v)}{\partial t} + u\frac{\partial(\rho v)}{\partial x} + v\frac{\partial(\rho v)}{\partial y} + w\frac{\partial(\rho v)}{\partial z} = -\frac{\partial p}{\partial y} + \left[\frac{\partial \tau_{xy}}{\partial x} + \frac{\partial \tau_{yy}}{\partial y} + \frac{\partial \tau_{zy}}{\partial z}\right] + \rho g_y \tag{D.3}$$

The z-component (Equation (D.4))

$$\rho\frac{\partial(w)}{\partial t} + u\frac{\partial(\rho w)}{\partial x} + v\frac{\partial(\rho w)}{\partial y} + w\frac{\partial(\rho w)}{\partial z} = -\frac{\partial p}{\partial z} + \left[\frac{\partial \tau_{xz}}{\partial x} + \frac{\partial \tau_{yz}}{\partial y} + \frac{\partial \tau_{zz}}{\partial z}\right] + \rho g_z \tag{D.4}$$

where:			
	ρ	Density	[kg/m^3]
	u, v, w	Velocity components	[m/s]
	p	Pressure	[Pa]
	τ_{ij}	Stress tensor components	[Pa]
	g_i	Gravity components	[m/s^2]

For a more compact notation, it is widely used in continuous mechanics the material or Lagrangian derivative (Equation (D.5))

$$\frac{D()}{Dt} = \frac{\partial()}{\partial t} + u\frac{\partial()}{\partial x} + v\frac{\partial()}{\partial y} + w\frac{\partial()}{\partial z} = \frac{\partial()}{\partial t} + \vec{v} \cdot \nabla() \tag{D.5}$$

The stress components on a fluid particle can be related with the viscosity of the fluid and the gradients of the velocity field. The postulate of Newton between stress and strain rate for a Newtonian fluid and the Stokes Hypothesis [30] arises a more simplified and suitable set of governing equations. For a incompressible (ρ=constant) Newtonian fluid with constant viscosity (μ=constant):

For the x-direction (Equation (D.6))

$$\rho\frac{D(u)}{Dt} = \mu\left[\frac{\partial^2 u}{\partial x^2} + \frac{\partial^2 u}{\partial y^2} + \frac{\partial^2 u}{\partial z^2}\right] - \frac{\partial p}{\partial x} + \rho g_x \tag{D.6}$$

For the y-direction (Equation (D.7))

$$\rho\frac{D(v)}{Dt} = \mu\left[\frac{\partial^2 v}{\partial x^2} + \frac{\partial^2 v}{\partial y^2} + \frac{\partial^2 v}{\partial z^2}\right] - \frac{\partial p}{\partial y} + \rho g_y \tag{D.7}$$

For the z-direction (Equation (D.8))

$$\rho\frac{D(w)}{Dt} = \mu\left[\frac{\partial^2 w}{\partial x^2} + \frac{\partial^2 w}{\partial y^2} + \frac{\partial^2 w}{\partial z^2}\right] - \frac{\partial p}{\partial z} + \rho g_z \tag{D.8}$$

The general solution of this set of equations has not been found, and it can be only solved for some special cases and simple geometries. For interested readers, detailed solutions for these special solution cases can be found in the book of 'Viscous Fluid Flow' [30]. For this reason, these fundamental equations governing the motion of any fluid particle can only be solved numerically for the general cases of interest. The engineering approach to solve the problem is the discretization of the Navier Stokes Equations and the use of different schemes that transforms the PDEs into a set of Algebraic Equations that can be solved easily for a computer.

For most engineering cases, the flow present is not laminar, but turbulent. A turbulent flow presents unsteady, irregular, random, and chaotic changes of the flow fields variables. Because of these fluctuating variables (as velocity and pressure) and the small scales present in the flow, the equations are not easy to handle. If these variables are decomposed into a time-averaged and a fluctuating quantities, a time-averaged equation can be obtained. Figure D.1 shows graphically the turbulent random fluctuations of the velocity in one point of the space.

In Equation (D.9), the decomposition of fluctuating variables of velocity, pressure and density are shown.

$$\begin{aligned} u(x,y,z,t) &= \bar{u}(x,y,z) + u'(x,y,z,t) \\ p(x,y,z,t) &= \bar{p}(x,y,z) + p'(x,y,z,t) \\ \rho(x,y,z,t) &= \bar{\rho}(x,y,z) + \rho'(x,y,z,t) \end{aligned} \tag{D.9}$$

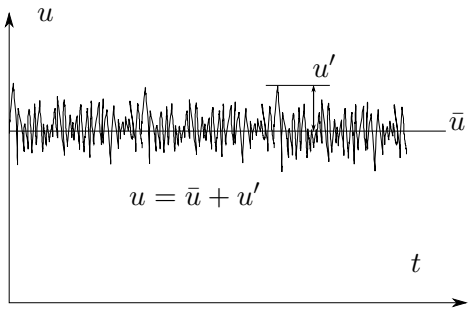

Figure D.1: Fluctuating velocity in a turbulent flow.

Introducing (D.9) into the general Navier Stokes equation, with some manipulation and applying the rules for time averaging, the Equation (D.10) is obtained, the so-called Time Averaged Navier Stokes Equation.

$$\rho\frac{\partial\overline{u_i}}{\partial t}+\rho\overline{u_j}\frac{\partial\overline{u_i}}{\partial x_j}=\frac{\partial}{\partial x_j}\left(\mu\frac{\partial\overline{u_i}}{\partial x_j}-\rho\overline{u_i'u_j'}\right)-\frac{\partial\overline{p}}{\partial x_i}+\rho g_i \tag{D.10}$$

If Equation (D.10) for turbulent flow is compared with its counterpart equation in laminar, it can be seen that an additional terms appears added to the total stress.

$$\tau_{total}=\tau_{lam}+\tau_{turb}=\left(\mu\frac{\partial\overline{u_i}}{\partial x_j}\right)-\left(\rho\overline{u_i'u_j'}\right) \tag{D.11}$$

The term (D.12) is named Reynold stress or apparent turbulent shear stress.

$$\tau_{turb_{i,j}}=\rho\overline{u_i'u_j'} \tag{D.12}$$

The Reynolds stresses represents the transport of momentum due to the fluctuating motion and acts as a stress on the fluid [33]. This new term introduces 6 additional unknowns into the set of governing equation with the need of their modelling. The Reynolds stresses are the start point of the RANS based turbulent models, that are one of the most important and more used methods in CFD. In the following section different models of modelling the turbulence are presented.

D.1 Turbulence Modelling

The modelling and prediction of the turbulence has been, and still is, the fundamental problem of computational fluid dynamics (CFD) and fluid mechanics. Over the years, different models have been created and developed.

- Direct numerical simulation (DNS)
- Large eddy simulation (LES)
- RANS-based turbulence models
- Detached eddy simulation (DES)

D.1.1 Direct numerical simulation (DNS)

A CFD simulation carried out with DNS solves numerically the Navier Stokes equations without any turbulence model. In order to do this, all the temporal and spatial scales

presented in the problem must be resolved. The need to solve the smaller scales in the flow, as Kolmogorov microscales, makes the computational cost of DNS extremely high and unsuitable for all industrial application. However, direct numerical simulation is very useful tool in fundamental research of the turbulence.

D.1.2 Large eddy simulation (LES)

The Large Eddy Simulation (LES) is based on a low-pass filtering of the Navier–Stokes equations. Based on the Kolmogorov Theory, the smaller eddies in the flow are found to be nearly isotropic and to have a universal behaviour, so it can be modelled easily. The large scale motions in the flows are dependent on the geometry, and in the LES model, these eddies are solved implicitly. Therefore, the small scales are eliminated from the Navier Stokes equation, while leaving only the large scale information. The small eddies are modelled separately in subgrid-scales models.

D.1.3 RANS-based turbulence models

For most engineering purposes, the time-averaged properties is representative enough of the flow characteristics, and there is no practical need of resolving all the details within the turbulent fluctuations. This is the basis behind the RANS models where an averaging process in done. The time-averaged Navier Stokes Equation (D.10) gives the information about the average quantities on the flow. The main objective behind the RANS (Reynolds Averaged Navier Stokes) is the computation and modelling of the Reynold Stresses (D.12) in order to be able to solve the equations. RANS turbulence models are classified based on the basis of the number of additional transport equations that need to be solved along with the Time Averaged Navier Stokes equations [29].

- Zero equation model: Mixing length model
- One equation model: Spalart–Allmaras model
- Two equation model: κ–ϵ model, κ–ω model and algebraic stress model
- Seven equation model: stress model

Boussinesq proposed in 1877 that Reynolds stresses may be proportional to mean rates of deformation (ie. the mean velocity gradients) as stated in Equation (D.13). This hypothesis is used in the Spalart-Allmaras model, the κ–ϵ model and κ–ω model.

$$-\rho\overline{u_i'u_j'} = \mu_t\left[\frac{\partial U_i}{\partial x_j} + \frac{\partial U_j}{\partial x_i}\right] - \frac{2}{3}\rho\kappa\delta_{ij} \tag{D.13}$$

where:			
	μ_t	Turbulent viscosity	[Pa s]
	κ	Turbulence kinetic energy	[m^2/s^2]
	δ_{ij}	Kronecker delta function	[−]

The turbulent kinetic energy is defined as Equation (D.14).

$$k = \frac{1}{2}\left(\overline{(u_1')^2} + \overline{(u_2')^2} + \overline{(u_3')^2}\right). \tag{D.14}$$

And the Kronecker delta function as Equation (D.15).

$$\delta_{ij} = \begin{cases} 1 & \text{if } i = j \\ 0 & \text{if } i \neq j \end{cases} \tag{D.15}$$

It is also useful in the field of the modelling of turbulence to define a kinematic turbulent viscosity, defined as Equation (D.16)

$$\nu_t = \frac{\mu_t}{\rho} \tag{D.16}$$

Zero equation model: Mixing length model

Based on a simple dimensional analysis, the kinematic turbulent viscosity can be expressed as the product of a velocity scale and a length scale (D.17)

$$\underbrace{\nu_t}_{[\mathrm{m}^2/\mathrm{s}]} \propto \underbrace{v}_{[\mathrm{m/s}]} \cdot \underbrace{l}_{[\mathrm{m}]} \tag{D.17}$$

where:	v	Velocity scale	$[\mathrm{m}^2/\mathrm{s}]$
	l	Length scale	[m]

Prandtl further assumed that the velocity scale in the flow was related with the length scale and the mean velocity gradients, allowing to write (D.17) as (D.18) and close up the problem of the modelling of ν_t in this quite simple and straightforward approach.

$$\nu_t = l_m^2 \left| \frac{\partial U}{\partial y} \right| \tag{D.18}$$

Depending on the kind of flow and conditions, different mixing lengths l_m^2 should be used. The adequate values for l_m^2 can be found for example in Table 3.2 of [29]. Based on [33] an overall assessment of advantages and disadvantages of the mixing length model are summarized on Table D.1.

Table D.1: Mixing length model

Advantages	**Disadvantages**
• Easy to implement and cheap in terms of computing resources. • Good predictions for thin shear layers: jets, mixing layers, wakes and boundary layers. • Well established.	• Completely incapable of describing flows with separation and recirculation. • Only calculates mean flow properties and turbulent shear stress.

The Standard κ–ϵ model

The $\kappa - \epsilon$ (Launder and Spalding, 1974) model consists on two PDE transport equations, one for the modelling of the turbulent kinetic energy (κ) and the other one for the turbulent

dissipation (ϵ). This κ and ϵ are used to define the velocity (v) and length scales (l) as stated in Equation (D.19).

$$v = \kappa^{1/2} \qquad l = \frac{\kappa^{3/2}}{\epsilon} \tag{D.19}$$

Therefore, with Equation (D.19) and using the same dimensional reasoning as in Equation (D.17), the turbulent kinematic eddy viscosity (ν_t) can be calculated with Equation D.20.

$$\nu_t \propto v \cdot l = C_\mu \frac{\kappa^2}{\epsilon} \tag{D.20}$$

where: C_μ | Dimensionless constant [–]

The standard $\kappa - \epsilon$ model uses two transport equations. One of them, for the turbulent kinetic energy (κ), presented in Equation (D.21).

$$\frac{\partial}{\partial t}(\rho k) + \frac{\partial}{\partial x_i}(\rho k u_i) = \frac{\partial}{\partial x_j}\left[\left(\mu + \frac{\mu_t}{\sigma_k}\right)\frac{\partial k}{\partial x_j}\right] + P_k + P_b - \rho\epsilon - Y_M + S_k \tag{D.21}$$

A second transport Equation (D.22) is used for the turbulent dissipation (ϵ).

$$\frac{\partial}{\partial t}(\rho\epsilon) + \frac{\partial}{\partial x_i}(\rho\epsilon u_i) = \frac{\partial}{\partial x_j}\left[\left(\mu + \frac{\mu_t}{\sigma_\epsilon}\right)\frac{\partial \epsilon}{\partial x_j}\right] + C_{1\epsilon}\frac{\epsilon}{k}\left(P_k + C_{3\epsilon}P_b\right) - C_{2\epsilon}\rho\frac{\epsilon^2}{k} + S_\epsilon \tag{D.22}$$

where: G_k	- Generation of turbulence kinetic energy due to the mean velocity gradients
G_b	- Generation of turbulence kinetic energy due to buoyancy
Y_m	- Contribution of the fluctuating dilatation in compressible turbulence to the overall dissipation rate
σ_κ	- Turbulent Prandtl numbers for κ
σ_ϵ	- Turbulent Prandtl numbers for ϵ
α_κ, α_ϵ	- User-defined source terms for κ and ϵ
$C_{1\epsilon}$, $C_{2\epsilon}$,$C_{3\epsilon}$	- Constants

For a better comprehension of the physical meaning of the Equations (D.21) and (D.22), they can be expressed in rates:

Rate of change of κ or ϵ + Transport of κ or ϵ by convection = Transport of κ or ϵ by diffusion + Rate of production of κ or ϵ - Rate of destruction of κ or ϵ.

The Equations (D.21) and (D.22) also consist on five adjustable constants σ_k , σ_ϵ , $C_{1\epsilon}$ and $C_{2\epsilon}$. The values of these constants have been found after numerous experiments and data fitting for a wide range of turbulent flows. Common values used for general problems are shown in (D.23), [29].

$$\begin{aligned} &C_\mu = 0.09 && \sigma_k = 1.00 && \sigma_\epsilon = 1.30 \\ &C_{1\epsilon} = 1.44 && C_{2\epsilon} = 1.92 \end{aligned} \tag{D.23}$$

Table D.2: Standard $\kappa - \epsilon$ model

Advantages	**Disadvantages**
• The parameters are calibrated by benchmark experimental data for different geometries and cases. • Robust and economical model. • Reasonable accuracy for a wide range of flows.	• Overly diffusive and poor performance for many situations as flows involving strong streamline curvature, swirl, rotation, separating flows and low-Re flows. • It is not able to predict round jet spreading rate • Un-physically excessive production of κ in regions of large strain rate as near a stagnation point that produce very inaccurate model predictions.

Based on [33] and [29] an overall performance of the Standard $\kappa-\epsilon$ model is summarized on Table D.3

Different version and improvements of the Standard $\kappa - \epsilon$, as the RNG $\kappa - \epsilon$ and the Realizable $\kappa - \epsilon$ have been also developed [3].

The RNG κ–ϵ model

In order to overcome some of the deficiencies of the Standard $\kappa - \epsilon$, The RNG κ–ϵ uses a statistical technique called Renormalization Group theory. Even they are similar in form, and while while the κ-equation remains almost identical, the most significant different with the standard model is the the additional strain rate term in the ϵ-equation. With this modification, an improved performance for rapidly strained flows and flows with high streamline curvature is archived. The effect of swirl on turbulence is also included in the RNG model, increasing accuracy for swirling flows.

The turbulent kinetic energy (κ) transport equation for the RNG κ–ϵ model is presented in Equation (D.24) [3].

$$\frac{\partial(\rho k)}{\partial t} + \frac{\partial(\rho k u_i)}{\partial x_i} = \frac{\partial}{\partial x_j}\left[\alpha_k \, \mu_{eff} \frac{\partial k}{\partial x_j}\right] + G_k + G_b - \rho\epsilon + Y_m + S_k \tag{D.24}$$

And the transport equation (D.25) for the turbulent dissipation (ϵ):

$$\frac{\partial(\rho \epsilon)}{\partial t} + \frac{\partial(\rho \epsilon u_i)}{\partial x_i} = \frac{\partial}{\partial x_j}\left[\alpha_k \, \epsilon_{eff} \frac{\partial \epsilon}{\partial x_j}\right] + C_{1\epsilon}\frac{\epsilon}{k}(G_k + C_{3\epsilon} G_b) - C_{2\epsilon}\rho\frac{\epsilon^2}{k} - R_\epsilon + S_\epsilon \tag{D.25}$$

where:			
	G_k	Generation of turbulence kinetic energy due to the mean velocity gradients	[]
	G_b	Generation of turbulence kinetic energy due to buoyancy	[]
	Y_m	Contribution of the fluctuating dilatation in compressible turbulence to the overall dissipation rate	[]
	α_κ	Inverse effective Prandtl numbers for κ	[]
	α_ϵ	Inverse effective Prandtl numbers for ϵ	[]
	α_κ, α_ϵ	User-defined source terms for κ and ϵ	[]

Although RNG improves some of the deficiencies of the Standard $\kappa - \epsilon$, it still does not predict correctly some common CFD problems, as the spreading of a round jet.

The realizable κ–ϵ model

Another improved model to the standard κ–ϵ is the realisable κ–ϵ. The model is able to resolve across the boundary layer [32].

- The model contains an alternative formulation for the turbulent viscosity.
- The dissipation rate (κ) transport equation is modified while the turbulent kinetic energy (ϵ) equation remains the same.

The turbulent kinetic energy (κ) transport equation for the Realizable κ–ϵ model is presented in Equation (D.26) [3].

$$\frac{\partial}{\partial t}(\rho k) + \frac{\partial}{\partial x_j}(\rho k u_j) = \frac{\partial}{\partial x_j}\left[\left(\mu + \frac{\mu_t}{\sigma_k}\right)\frac{\partial k}{\partial x_j}\right] + P_k + P_b - \rho\epsilon - Y_M + S_k \tag{D.26}$$

And the transport Equation (D.27) for the turbulent dissipation (ϵ).

$$\frac{\partial}{\partial t}(\rho\epsilon) + \frac{\partial}{\partial x_j}(\rho\epsilon u_j) = \frac{\partial}{\partial x_j}\left[\left(\mu + \frac{\mu_t}{\sigma_\epsilon}\right)\frac{\partial \epsilon}{\partial x_j}\right] + \rho\, C_1 S\epsilon - \rho\, C_2 \frac{\epsilon^2}{k + \sqrt{\nu\epsilon}} + C_{1\epsilon}\frac{\epsilon}{k} C_{3\epsilon} P_b + S_\epsilon \tag{D.27}$$

The variables G_k, G_b, Y_M represent the same as with the RNG model, C_2 and C_{1_ϵ} are constants, σ_κ and σ_ϵ are the turbulent Prandtl number for κ and ϵ and S_K and S_ϵ are user-defined source terms. Also C_1, η and S are defining according to Equation D.28-

$$C_1 = \max\left[0.43, \frac{\eta}{\eta + 5}\right], \qquad \eta = S\frac{k}{\epsilon}, \qquad S = \sqrt{2 S_{ij} S_{ij}} \tag{D.28}$$

Based on [3] and [8] an overall performance of the Realizable $\kappa - \epsilon$ model is summarized on Table D.3

Table D.3: Standard $\kappa - \epsilon$ model

Advantages	**Disadvantages**
• Predicts planar and round jet spreading correctly. • Suitable for boundary layers under strong adverse pressure gradients or separation. • Superior ability to capture the mean flow of the complex structures • Good performance on flow with rotation, recirculation, and strong streamline curvature.	• May produce non-physical turbulent viscosities for problems with multiple references frames.

D.1.4 Detached eddy simulation (DES)

The detached eddy simulation method is a hybrid combination between the LES and RANS models. The resolving of the boundary layer and near-wall region is done with a RANS strategy, while the rest of the flow is solve with a LES model. The reason of switching from LES to RANS is that solving the boundary layer with LES would be computational prohibitive, so the RANS model is used in those regions. The application of DES, is lower than LES, but still require significant amount CPU resources.

D.2 Near Wall Treatment

The presence of a wall will affect how the fluid flows and the velocity field close to it. As the fluid moves next to a solid surface, and due to the effects of the viscosity, the molecules close to surface are slowed down, reaching the non-slip condition in the surface, where the velocity of the fluid is zero.

The development of a velocity gradient, from the surface of the body, where the velocity is zero, to a certain distance form the wall, where the velocity matches the free-stream velocity produces the so-called boundary layer shown in Figure D.2. The boundary layer thickness δ is defined as the distance away from the surface where the velocity reaches 99% of the free-stream velocity.

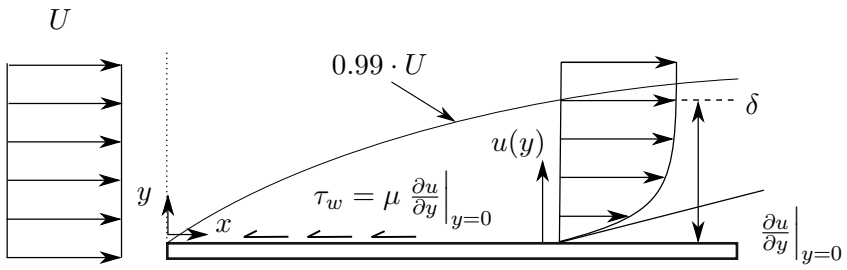

Figure D.2: Boundary layer

The walls are the main source of vorticity and turbulence of the flow, and the boundary presents large gradients in mean velocity. The importance of an accurate near-wall modelling is critical in a CFD simulation.

The near-wall region, based on the relative importance of the laminar and turbulent stress of (D.11) can be subdivided into three layers [3].

- **Inner layer**, also called viscous sub-layer. This region is characterise for an almost laminar behaviour (ie. τ_{lam} is dominant with respect to τ_{tur}) and because the viscosity in this region plays affects significantly the transfer of momentum, heat and mass.
- **Outer layer**, also called fully-turbulent layer where the turbulence plays a major role (ie. τ_{tur} is dominant).
- **Overlap layer**, the region between the inner and outer layer where the effects of molecular viscosity and turbulence are equally important (ie. τ_{lam} is of the same order of magnitude as τ_{tur}).

In Figure D.3, the graphical representation of this subdivision according to the relative magnitude of the shear stress is shown.

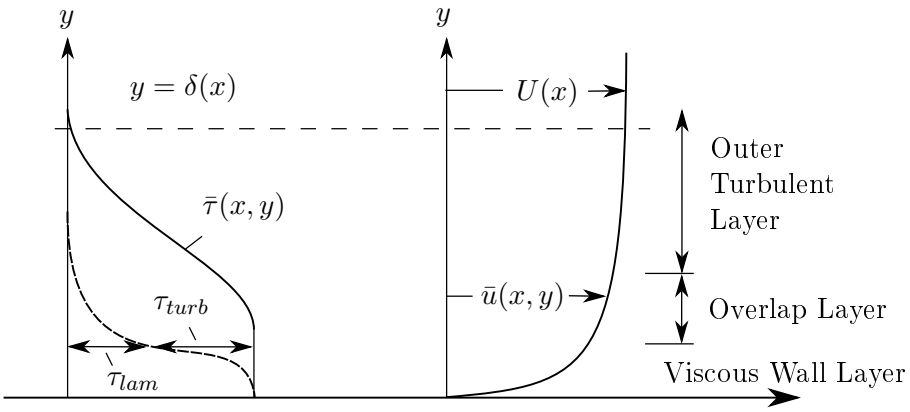

Figure D.3: Typical velocity and shear distribution in turbulent flow near the wall

One main challenge in CFD is how to treat these thin near-wall layer, that are crucial to the accuracy of the solution. Traditionally, there are two approaches to modelling the near-wall region:

- Wall functions: the viscous sub-layer is not resolved analytically, but instead semi-empirical approximations, called wall functions, are used to account for the flow behaviour in this region.
- Near wall modelling approach: the viscous layer is resolved numerically, and turbulence models are modified in order to include these viscous effects.

More information for interested readers about these two approaches and near wall treatment can be found on the book of W. Malalasekera [29].

Appendix E

Mesh Quality Measurement

In this chapter, the three most used parameters to measure the quality of a mesh will be presented and explained.

E.0.1 Skewness

The skewness of a cell indicates how close or how far is the cell from being ideal. There is two methods for measuring the skewness, one of them based on the equilateral volume (used for tetrahedral elements) and another one based on the deviation from a normalized equilateral angle (used for all cells and face shapes). As the mesh that will be initially generated is tetrahedral, the formula used to calculate the value of the skewness for tetrahedral cells based on the equilateral volume is presented in Equation (E.1) [4].

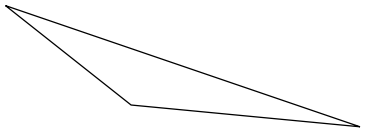

Highly Skew Cell

Figure E.1: Skewness

$$\text{Skewness} = \frac{\text{Optimal Cell Size} - \text{Cell Size}}{\text{Optimal Cell Size}} \tag{E.1}$$

The optimal cell size is the size is defined as an equilateral cell with the same circumradius.

The cell skewness will be the maximum skewness compute for any face of the cell. A value of 0 indicates an optimal cell (equilateral) and a value of 1 indicates a completely degenerate cell. Highly skewed cells can lead to stability and accuracy problems for CFD solvers [29], so ensuring a low value for the skewness is a crucial step in the mesh generation.

E.0.2 Aspect Ratio

The aspect ratio is a measure of the stretching of the cell. It is defined as the ratio of the longest edge length to the shortest one. The aspect ratio, as with the skewness, is used to see how far is the cell from being ideal. Figure E.2 shows the concept of aspect ratio. An ideal element have an aspect ratio of 1, and the bigger its ratio is, the worse is the quality of the cell.

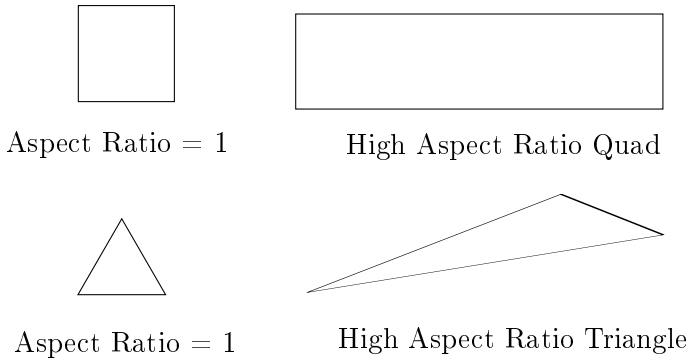

Figure E.2: Aspect Ratio

The aspect ratio applies to triangular, tetrahedral, quadrilateral, and hexahedral elements and is defined differently for each element type. The different equations quantifying the aspect ratio for each element type can be consulted in [4].

E.0.3 Smoothness

As several regions within the computational volume will have different elements sizes, it is important to ensure a smooth transition between those regions. A rapid change in the size of the cells will have a negative influence on the convergence and accuracy of the numerical solution. Sudden jumps in the size of the cells should be avoided because it may induced numerical errors at nearby nodes.

In the ANSYS Fluent the smoothness is achieved based on the growth ratio specified between the different regions. A growth ratio of 1.05 means that the volume of the cells are increased by 5% between adjacent elements until it matches the dimensions of the outer cells defined.

Appendix F

Mesh Type Conversion

This appendix serves to evaluate the differences on the solution between a tetrahedral mesh and the polyhedral. This polyhedral mesh is created by a conversion process from the tetrahedral mesh that have implemented in ANSYS Fluent. In Figure F.1, the tetrahedral and polyhedral elements are shown.

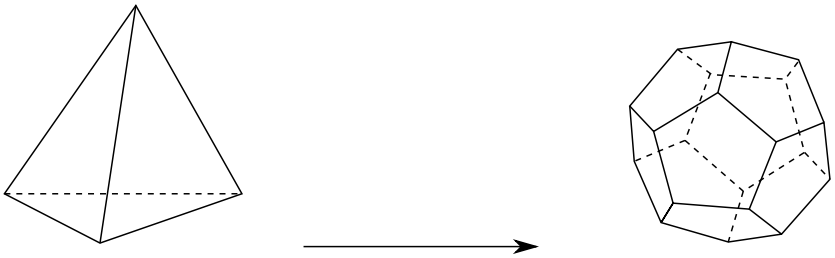

Figure F.1: Tetrahedral to polyhedral conversion.

While a tetrahedral mesh have only four neighbours, the polyhedral one have typically around 10 . This allows the better to approximated the gradients of the variables. Although more neighbours means more storage and computing operations per cell is compensated by a higher accuracy of the solution [21].

In order to check the differences between the two different meshes, simulations comparing a converted mesh (ie. polyhedral) and non-converted one (ie. tetrahedral) are carried out. The creation of the polyhedral mesh can not be directly created in ANSYS Meshing, but need to be converted through a tool implemented in Fluent. This tool converts the tetrahedral mesh created into a polyhedral one, but does not allow the user to control any parameter.

One of the comparison correspond to the new car, and the other to the same design but with a cut of 574mm of the tail. The second one is chosen as it is expected to have separated flow in the back, and the performance of the mesh in this situation wants to be evaluated. Tables F.1 and F.2 present the information of mesh, conversion process, bandwidth reduction and solution.

	Polyhedral Mesh	Tetrahedral Mesh
Mesh Type	Tetrahedral	Tetrahedral
Nodes	$3.610\ 10^6$	$3.610\,10^6$
Elements	$17.979\ 10^6$	$17.979\ 10^6$
Face Sizing	7 mm	7 mm
Body Sizing	30 mm	30 mm
Growth Rate	1.05	1.05
Mesh Conversion	Polyhedral	None
Elements Polyhedral	$3.653\ 10^6$	-
Ratio Elements	4.922	-
Model	Real. κ–ϵ	Real. κ–ϵ
Drag Coefficient	0.12542	0.1272
Lift Coefficient	0.13133	0.1331
Drag Difference	-1.399 %	-
Lift Difference	-1.3298 %	-

Table F.1: Mesh and conversion information: new design.

	Polyhedral Mesh	Tetrahedral Mesh
Mesh Type	Tetrahedral	Tetrahedral
Nodes	$3.876\,10^6$	$3.876\,10^6$
Elements	$19.606\,10^6$	$19.606\,10^6$
Face Sizing	7 mm	7 mm
Body Sizing	30 mm	30 mm
Growth Rate	1.05	1.05
Mesh Conversion	Polyhedral	None
Elements Polyhedral	$3.924\,10^6$	-
Ratio Elements	4.231	-
Model	Real. κ–ϵ	Real. κ–ϵ
Drag Coefficient	0.14732	0.15285
Lift Coefficient	0.19086	0.20148
Drag Difference	-3.6179 %	-
Lift Difference	-5.2710 %	-

Table F.2: Mesh and conversion information: new design with 574 mm cut.

From Tables F.1 and F.2, it can be seen that the solution for the drag and lift present small differences. For the case where with no separated flow, the difference in the drag is smaller than 1.5 % while for the case with separated flow the difference is slightly bigger than 3.5 %. Although the mesh independence of the tetrahedral solution have been ensured, the conversion into polyhedral still creates a small difference in the result. It is difficult to prove without a benchmark which one of these solutions are the closer to the reality. But the advantages of polyhedral meshes have been proved arise better accuracies and convergences and fewer need of memory and computing time [21]. As the differences are within the 5% for the drag and lift, the conversion is considerable acceptable.